U.PORTO

FEUP FACULDADE DE ENGENHARIA
UNIVERSIDADE DO PORTO

ANCHORS FOR FLOATING WIND TURBINES

RENZO BELMOK ALVES

Dissertação submetida para satisfação parcial dos requisitos do grau de

MESTRE EM ENGENHARIA CIVIL — ESPECIALIZAÇÃO EM GEOTECNIA

Orientador: Professor Doutor António Joaquim Pereira Viana da Fonseca

---

Coorientador: Professor Doutor Ole Hededal

JUNHO DE 2025

MESTRADO EM ENGENHARIA CIVIL 2024/2025

DEPARTAMENTO DE ENGENHARIA CIVIL

Tel. +351-22-508 1901

✉ m.ec@fe.up.pt

Editado por

FACULDADE DE ENGENHARIA DA UNIVERSIDADE DO PORTO

Rua Dr. Roberto Frias

4200-465 PORTO

Portugal

Tel. +351-22-508 1400

✉ feup@fe.up.pt

http://www.fe.up.pt

A meus Pais

"My land has palm trees,
Where the thrush sings;
The birds, which chirp here,
They don't chirp like they do there.
Our sky has more stars,
Our floodplains have more flowers,
Our forests have more life,
Our life more loves.
[…]
God forbid that I die,
Without me going back there;
Without me enjoying the primes
Which I can't find here;
Without seeing the palm trees,
Where the thrush sings."

Exile Song, Gonçalves Dias (1843)

ACKNOWLEDGMENTS

I would like to express my deepest gratitude and admiration to the following individuals:

To Professor António Joaquim Pereira Viana da Fonseca, who has been one of my greatest sources of inspiration and who has consistently supported and guided my journey into the field of geotechnical engineering.

To the entire team at COWI A/S, in particular Ole Hededal, Martin Østergaard, Søren Nielsen, Søren Sørensen, and Nikolaj Bjerge, for their invaluable support throughout the development of this work. Their critical insight and thoughtful feedback helped shape every aspect of this research. I am also grateful to the renewable energy team at the Aarhus office for their warm welcome and for always being willing to clarify my questions on the topic.

To all my friends and family in Brazil. Due to space limitations, I cannot mention each of you individually, but your support has been essential to both this work and my personal journey.

To Vinicius Rodrigues and Lucas Leão, for being among the most valued friends I had the privilege of meeting during my time at FEUP.

RESUMO

O presente trabalho tem como objetivo contribuir para o entendimento do comportamento de âncoras de sucção instaladas em solos não coesivos, com foco específico em geometrias representativas de aplicações comerciais. A literatura existente revela uma lacuna significativa quanto ao estudo desse tipo de ancoragem em areias, particularmente no que se refere à influência do coeficiente de pressões laterais (K) e ao chamado “efeito de silo”.

A metodologia baseou-se em modelações numéricas utilizando o software PLAXIS 2D, por meio de análises em regime de deformação plana e simetria axial. Foram simuladas diferentes geometrias de caixões, variando o diâmetro, a razão de aspecto (L/D), e a densidade relativa do solo. Avaliou-se o desempenho das âncoras sob carregamentos verticais, horizontais e inclinada (30°), com variações na posição do ponto de aplicação da carga (z_{pad}). Também foram comparadas equações analíticas propostas por diversos autores (Cheng et al., 2021; Hirai, 2023; Zhao et al., 2018), destacando as diferenças na formulação da distribuição de tensões verticais no solo.

Os resultados obtidos indicam que o modelo numérico reproduz satisfatoriamente o comportamento previsto analiticamente para geometrias realistas, evidenciando a importância do efeito de silo no interior do caixão. Foi observado que a influência de K se torna mais significativa à medida que se aumentam a razão L/D e o ângulo de atrito do solo. Além disso, a posição ótima do padeye para cargas horizontais manteve-se em torno de z_{pad} = 0.65, com variações em função da densidade relativa.

Este estudo contribui para a compreensão do comportamento de âncoras de sucção em solos arenosos, propondo uma base para futuros desenvolvimentos normativos e investigações em modelos tridimensionais.

PALAVRAS-CHAVE: Âncoras de Sucção, Solos não Coesivos, Modelação Numérica, Capacidade de Carga, Deformação Plana

Abstract

This study aims to enhance the understanding of suction anchor behavior in cohesionless soils, with a particular focus on geometries representative of commercially viable designs. The existing literature reveals a notable knowledge gap in the analysis of suction anchors embedded in sandy soils, especially regarding the influence of the coefficient of earth pressure (K) and the so-called "silo effect".

The methodology involved numerical modeling using PLAXIS 2D, based on both plane strain and axisymmetric analyses. Various caisson geometries were simulated, with different diameters, aspect ratios (L/D), and relative densities of the surrounding soil. The performance of the anchors was assessed under vertical, horizontal and inclined (30°) loading, varying the load application depth (z_{pad}). Analytical formulations proposed by Cheng et al. (2021), Hirai (2023) and Zhao et al. (2018), were also compared, with particular attention to how they model vertical stress distribution in the soil.

The results demonstrate that the numerical models accurately capture the predicted behavior for realistic anchor geometries, highlighting the relevance of the internal silo effect. The influence of K was shown to increase with higher aspect ratios and soil friction angles. Furthermore, the optimal padeye position for horizontal loading was consistently observed near z_{pad} = 0.65, with variations dependent on relative density.

This work contributes to the geotechnical understanding of suction anchors in sandy soils and provides a foundation for future development of design guidelines and three-dimensional modeling approaches.

KEYWORDS: Suction Anchors, Cohesionless Soil, Numerical Modeling, Bearing Capacity, Plane Strain.

CONTENTS

LIST OF FIGURES

LIST OF TABLES

Symbols, Acronyms and Abbreviations

FWT – Floating Wind Turbines

TLP – Tension Leg Platform

AHV - Anchor Handling Vessel

FPSO – Floating Production Storage and Offloading

3D-FEM – 3 Dimensional Finite Elements Method

MMC – Modified Mohr-Coulomb

API – Application Programming Interface

L – Length of the suction anchor

L_p – Length of the attached load, padeye position

z_{pad} – Normalized padeye position

D – Diameter of the suction anchor

D_i – Internal diameter of the suction anchor

D_o – Outside diameter of the suction anchor

D_e – External diameter of the suction anchor

t – Thickness of the suction anchor

λ – Aspect ratio of the suction anchor(L/D)

θ – Angle between the mooring line and the horizontal

γ' – Effective soil weight

A_i – Area of a disk within the suction anchor

C_i – Circumference of a disk within the suction anchor

dz – Infinitesimal depth of a disk within the suction anchor

σ'_{zi} – Effective vertical pressure inside the suction anchor

σ'_{ze} – Effective vertical pressure outside the suction anchor

K – Coefficient of lateral pressure

K_0 – Coefficient of lateral pressure at rest

K_p – Coefficient of lateral pressure of passive state

ψ – Dilation angle of the soil

φ – Friction angle of the soil

φ_{ini} – Initial friction angle of the soil

φ_{cv} – Critical-state friction angle of the soil

φ_{pk} – Peak friction angle of the soil

D_r – Relative density of the soil

δ – Interface-soil friction angle

P_{vye} - Vertical yield resistance of the soil outside the suction anchor

P_{vyi} - Vertical yield resistance of the soil inside the suction anchor

W_c - Buoyant weight of the suction anchor

V_t – Vertical uplift capacity (by Hirai, 2023)

V_f – Vertical uplift capacity (by Houlsby et al., 2005)

V_{ult} – Vertical uplift capacity (by Zhao et al., 2018 and Cheng et al., 2021)

N – Lateral capacity factor

c – Cohesion

ν – Poisson's ratio

m - Load-spreading parameter of vertical stress reduction outside soil (by Houlsby et al., 2005)

η-k – Soil stress level factor

HS – Hardening Soil

γ_{sat} – Saturated soil weight

E_{ur}^{ref} – Unloading and reloading stiffness

E_{oed}^{ref} – Tangent stiffness for the first load

E_{50}^{ref} – Secant stiffness of reference

E – Elastic module

e_{init} – Initial void ratio of the soil

e_{min} – Minimal void ratio of the soil

e_{max} – Maximum void ratio of the soil

m – Power stress level dependency of the stiffness (by PLAXIS 2D)

σ'_{xx} - σ'_{yy} – Horizontal and Vertical effective stresses

1
INTRODUCTION

1.1. OVERVIEW

The increasing sophistication of modern technologies and lifestyles has necessitated the expansion of energy production. However, since the advent of the first industrial revolution, humankind has emitted a substantial amount of CO_2 into the atmosphere, in comparison with the levels observed in pre-industrial past centuries.

With this amount of CO_2 emitted in the atmosphere, the natural cycle has been deregulated, which has resulted in significant natural disasters that have afflicted the planet in recent years, as evidenced by the 2022 European heat wave, which resulted in the death of over 61.000 people, according to the "Heat-related mortality in Europe during the summer of 2022" published in Nature Medicine in 2023, the analysis estimated more than 61.000 heat-attributable deaths between 30 May and 4 September of 2022.

In an aim to reverse the current situation, the Paris Agreement was established. Is a legally binding international treaty on climate change, adopted by 195 Parties at the United Nations Climate Change Conference (COP21) in France, Paris, on 12 December 2015, with the objective of limiting the temperature trend and ensuring that the global mean temperature remains below 2°C above pre-industrial levels. The implementation requires economic and social transformation, working on a five-year cycle ambition climate action, increasing the degree of ambition each cycle according to the nationally determined contribution (NDC), and providing a financial, technical and capacity building support for the countries who need it.

A global trend of modifying the energetic matrix to reverse environmental issues and transition to renewable energy sources is evident. This shift in energy sources has a notable impact on wind energy as well. The generation of wind energy can be categorized into two distinct modalities, onshore and offshore. The development of onshore wind energy was the first to be explored. However, it was observed that certain environmental variables have the capacity to influence wind energy production. These variables include wind speed and consistency. In order to mitigate these issues, an environment was searched for that would reverse the effects of these variables. The sea was identified as the ideal solution. Offshore wind production has been demonstrated to be more efficient than onshore wind production. The presence of no geological barriers at sea results in greater wind speed and consistency. The production of energy is thus enhanced and optimized by taking advantage of the wind currents.

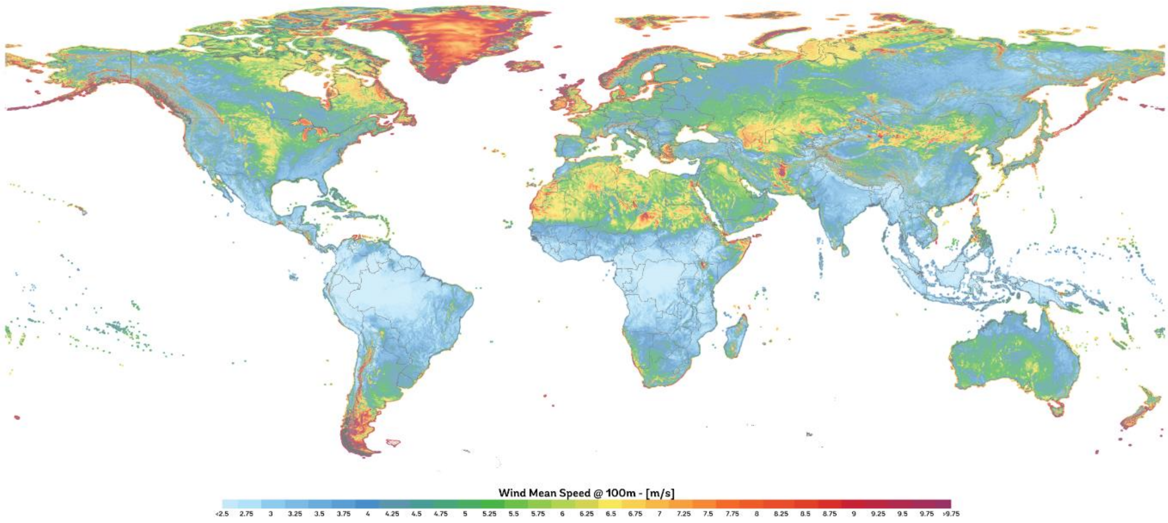

Figure 1.1 – Global wind mean speed at 100m above surface, “Global Wind Atlas”

In order to ensure the stability and functionality of the offshore wind turbine, it is imperative that it be securely anchored to prevent it from being carried by sea, wind, and currents. In order to achieve this objective, two distinct types of wind turbines were developed: the bottom-fixed turbine, which is the most commonly used in shallow waters and is composed of steel structures and reinforced concrete, and the floating wind turbine, which is a more recent development and utilizes a chain to attach the turbine to an anchor embedded in the seabed. The utilization of floating systems is particularly prevalent in contexts involving high sea depths, wherein the implementation of bottom-fixed systems becomes impractical due to the associated costs. In such scenarios, floating wind turbines emerge as a viable solution, effectively addressing the unmet needs in these environments.

In this context, the imperative for the exploration of floating wind turbines is twofold: first, to augment the global green energy production, and second, to facilitate the transition of the energetic matrix to a more sustainable one, benefiting both humanity and the environment.

1.2. OBJECTIVE

Among the five most commonly used anchor types for the fixation of floating wind turbines, namely gravity-based, drag, pile, suction, and plate anchors, which are further detailed in Chapter 2, suction anchors stand out as a particularly promising solution. This is largely due to their ease of installation, recoverability after decommissioning, and the potential for a single suction anchor to serve multiple mooring lines, thanks to their high vertical and lateral load-bearing capacities.

While extensive research and well-established design guidelines exist for suction anchors in cohesive soils (clays), the same level of development is lacking for cohesionless soil (sands). Although some studies have investigated the behavior of suction anchors in sandy soils, they often focus on limited geometries that do not reflect the full range of commercial anchor dimensions. As such, a significant knowledge gap remains in the understanding of suction anchors behavior embedded in sands, particularly for configurations relevant to large-scale dimensions.

Therefore, this thesis provides an envelope for different suction anchors shape, englobing different soil conditions using a 2D model, with the following main objectives:

- The modelling of a suction anchor in sand, using Python scripts.
- The behavior under horizontal and vertical loading in the models.
- An optimized padeye position for horizontal, vertical and inclined loading

1.3. Structure of the Thesis

The present thesis is structured in 7 chapters.

The first chapter provides an introduction and an explanation of the topic, touching upon its most superficial aspects.

Chapter 2 provides an overview of floating wind turbines, commencing with an introductory segment that defines the subject matter. The chapter then delves into the realm of wind energy, culminating in a discussion of the various anchors employed in wind turbine installations.

Chapter 3 provides a comprehensive overview of suction anchors, encompassing their structural intricacies, recognized behaviors, and comparative advantages over alternative anchors.

In Chapter 4, the reader will find an examination of limit equilibrium and numerical methods employed to predict the behavior of suction anchors. This analysis demonstrates the approaches of three different papers: those by Hirai (2023), Cheng et al. (2021), and Zhao et al. (2018). The chapter also provides an explanation of how the vertical and horizontal ultimate capacity are achieved in the papers previously mentioned.

Chapter 5 was developed with a focus on the explanation of the structure of the Python scripts used to calculate, model, and interpret the behavior of the suction anchors in sand.

Chapter 6 provides an explanation of the behavior of the forces of the model under vertical, horizontal and inclined (30°) forces, with the optimized attached positions of loading.

And Chapter 7 provide a conclusion of the work highlighting the findings and future works.

2
OFFSHORE WIND TURBINES

2.1. INTRODUCTION

Historically, offshore structures have been predominantly associated with the oil and gas industry. The first offshore oil rig was constructed in 1947 in the Gulf of Mexico, operating in a water depth of just 6 meters. With the advancement of petroleum technologies during the 1950s, particularly during what is referred to as the "Third Wave" of innovation, the development of jack-up rigs enabled drilling operations to extend into depths of up to 53 meters.

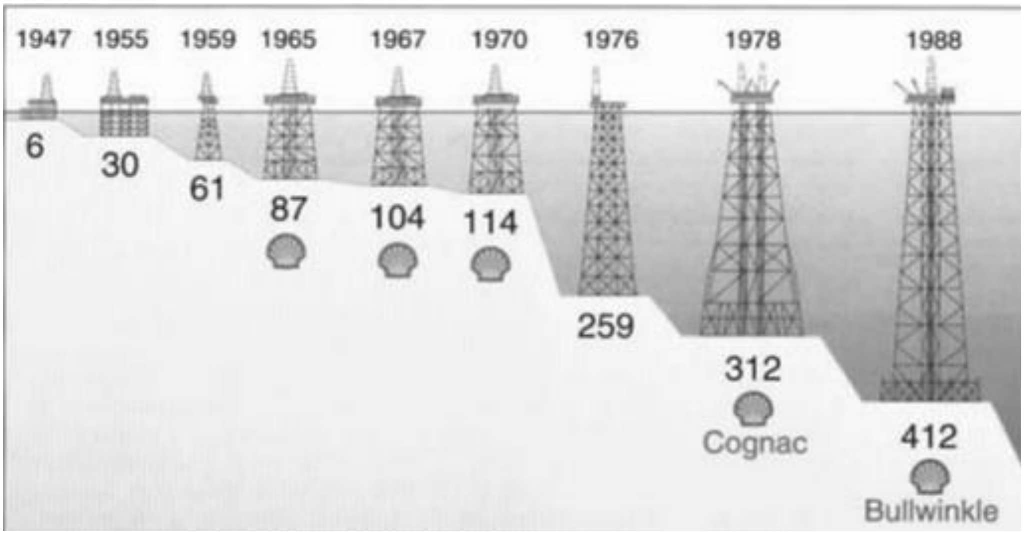

Figure 2.1 – Bottom-fixed evolution in the Gulf of Mexico of water depth (“Historical Development of Offshore Structures”, Chakrabarti et al., 2007)

Since the early 21st century, there has been a notable expansion in wind energy development, driven by the urgent need to shift the global energy matrix in response to climate change and energy security concerns, especially following the oil crisis of 1973. The offshore wind industry has leveraged the extensive experience of offshore oil and gas infrastructure, particularly the use of bottom-fixed structures, which have been utilized since the late 1940s.

While bottom-fixed foundations provided a logical starting point for offshore wind turbine deployment, their application is constrained by the increased loads and structural demands of modern wind turbines.

Unlike oil platforms, which typically support minimal superstructure, wind turbines are subjected to significant aerodynamic and hydrodynamic forces. Consequently, bottom-fixed foundations are generally limited to water depths of approximately 50 meters, as noted in the report Offshore Wind in Europe (2017).

However, optimal offshore wind conditions are often found in deeper waters. According to Equinor (Floating Offshore Wind), nearly 80% of the world's offshore wind potential is located in regions with water depths exceeding 60 meters. This limitation has spurred the development of floating offshore wind turbine technologies, which offer greater flexibility in site selection and the potential to take advantages of more consistent and stronger wind resources located farther from shore.

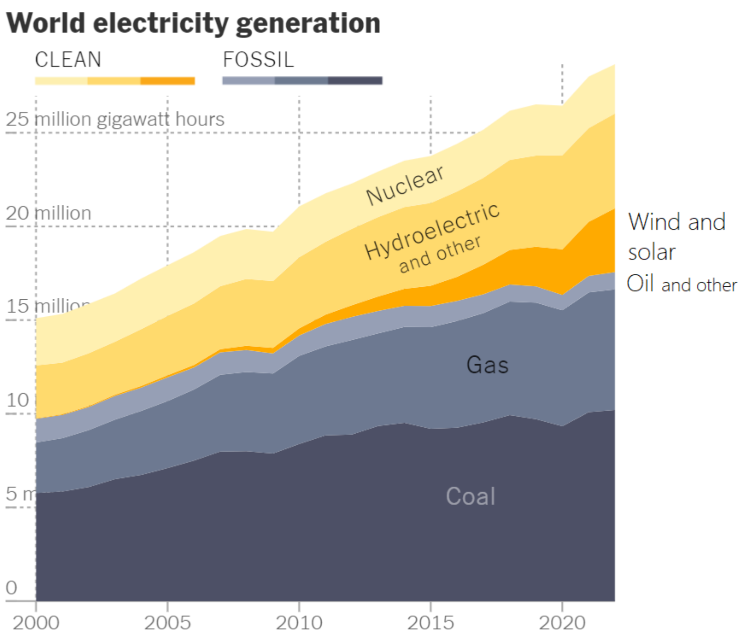

Figure 2.2. – World energy production (The New York Times, "What's Going on in This Graph? | Global Electricity Sources")

2.2. Wind Energy

The transformation of the kinetic energy of the blades, due the wind action, into mechanical rotative energy, wind energy is notably more productive in places with a high intensity and constancy of the wind. In the terrestrial environment the wind is limited by the natural nonregulation of the Earth's geography, dissipating high amounts of wind intensity, consequently the constancy of the winds. To avoid this and another problem, wind turbines were moved to the sea, where the environment is favorable to wind production, according to Business Norway "Offshore wind turbines generally run at 35–50 per cent capacity, whereas onshore turbines have a lower capacity of 25–35 per cent."

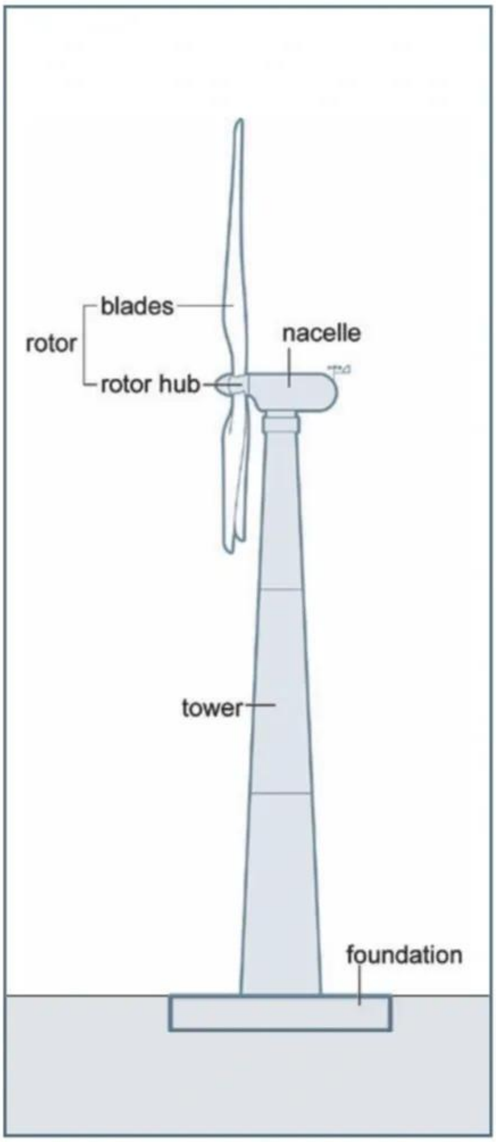

Figure 2.3 – Onshore wind turbine scheme

The trend of the increase wind energy growths, even with the bottom-fixed wind turbines limitations, being the most common due to the cost, as mentioned in Guide to a Floating Offshore Wind Farm "At the end of 2021 cumulative installed global offshore wind capacity was approximately 57 GW. Only approximately 140 MW of this is floating, with the rest fixed to the seabed.".

In 2023, China accounted for approximately two-thirds of the global increase in wind energy capacity, adding an estimated 76 GW, of which 5 GW originated from offshore wind farms. In comparison, the European Union expanded its wind energy capacity by around 15 GW during the same period. This growth was supported by new policy frameworks and strategic targets introduced under initiatives such as the REPowerEU Plan, the Green Deal Industrial Plan, and the European Wind Energy Action Plan.

Looking ahead, offshore wind capacity in the EU is projected to reach 77,2 GW by 2030, according to the International Energy Agency (Offshore Wind Capacity by Country). This represents a more than twofold increase compared to the 37 GW of installed offshore capacity expected in 2025, as reported by

WindEurope (Wind Energy in Europe: 2024 Statistics and the Outlook for 2025–2030). These figures reflect the EU's commitment to scaling up offshore renewable energy as part of its broader decarbonization and energy security goals.

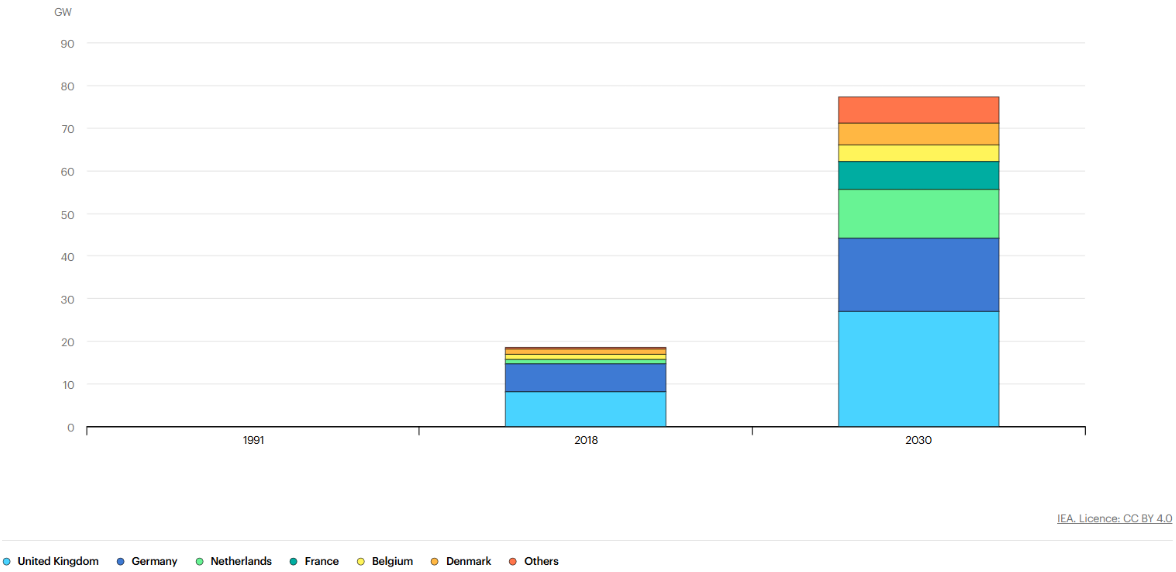

Figure 2.4 – Forecast of offshore wind energy production in GW (International Energy Agency)

2.3. Bottom-Fixed Wind Turbine

Bottom-fixed systems have long been the most established and extensively studied foundation solution for offshore structures. When compared to floating systems, they currently represent the most cost-effective option for offshore wind energy deployment. Within the European Union, the majority of offshore wind turbines are supported by monopile foundations, which dominate the market due to their relative simplicity and economic advantages. Jacket and gravity-based foundations follow in prevalence, serving as alternatives in sites with greater water depths or specific geotechnical conditions.

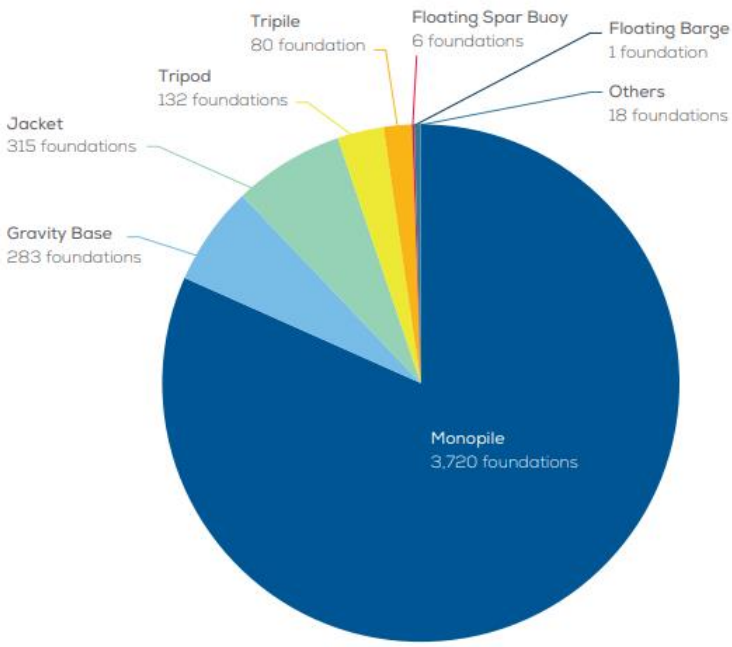

Figure 2.5 – Foundations of wind turbines in Europe (WindEurope)

Monopiles are composed of hollow steel pipes that are embedded in the soil, exhibiting a behavior analogous to that of a pile. They are subjected to horizontal loads resulting from sea and wind currents, as well as vertical load, compression, from the self-weight of the wind turbine. The primary challenge associated with monopiles pertains to the water depth, as the dimensions of the foundations become exceedingly large, and the installation process becomes arduous in cases of high-water depth. The installation process begins with the transport of the monopile to the designated site. The monopile is then lifted into place by a crane, followed by the use of a hydraulic hammer to drive it into the seabed. This process generates significant noise, which potentially impacts the marine life in the vicinity of the installation site.

The jacket is a lightweight, braced structure typically composed of three or four steel legs connected by diagonal and horizontal members. At the base of each leg, pile foundations are integrated, which are subjected to combined horizontal and vertical loads, including both compressive and tensile forces. Unlike monopiles, which behave as individual elements, jacket foundations exhibit the load-sharing characteristics of pile groups. One of their key advantages is the ability to be installed at greater water depths than monopiles. The installation process begins with the pre-installation of piles using an installation template to ensure precise positioning. These piles are driven into the seabed using techniques similar to those employed for monopile foundations. Subsequently, the jacket structure is transported to the site, lifted into position by a crane, and secured onto the pre-installed piles. The final step involves grouting or concreting the connections between the jacket and pile elements to ensure structural integrity.

In contrast, gravity base foundations are massive structures typically constructed from reinforced concrete, with weights ranging from 1.500 to 4.500 tons. Their stability on the seabed is ensured primarily through self-weight, and they are subjected to both horizontal and vertical loads, exhibiting behavior analogous to that of shallow foundations. The installation process differs significantly from that of jacket and monopile foundations, as it requires seabed preparation prior to placement, this includes the removal of surface soil layers with insufficient bearing capacity. Transportation poses a considerable logistical challenge due to the substantial weight of the structure, often necessitating the use of heavy-lift crane vessels. To address these difficulties, a float-and-submerge installation method was developed. In this approach, the gravity base is prefabricated onshore in a dry dock and designed to be self-floating. Once transported to the offshore installation site, the structure is gradually submerged and positioned on the seabed through controlled ballasting using water and sand.

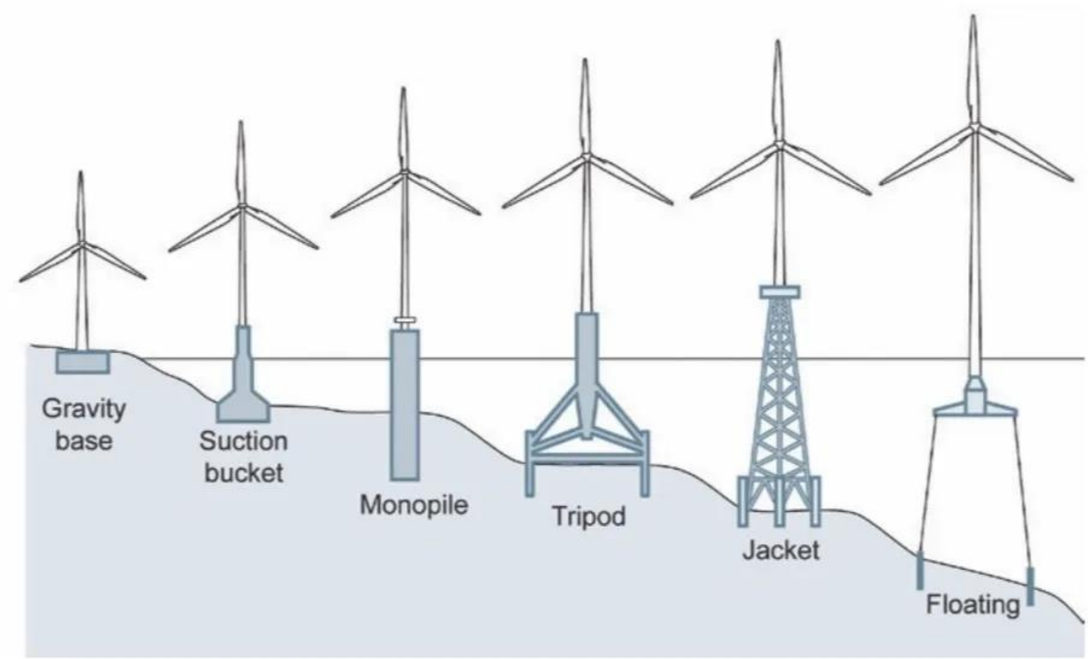

Figure 2.6 – Fixing system of wind turbines

2.4. FLOATING WIND TURBINE

Floating wind turbines (FWTs) differ significantly from bottom-fixed systems, comprising three key components: the floating platform, the mooring system, and the anchoring system. Among the various floating foundation concepts, the most commonly employed are the spar-buoy, semi-submersible, and tension leg platform (TLP) designs.

The spar foundation, as its name suggests, consists of a long, slender cylindrical structure typically constructed from steel. It offers substantial hydrostatic stability due to its deep draft and low center of gravity. The installation of a spar foundation generally involves four stages: transportation, upending, ballasting/de-ballasting, and turbine integration. The structure is transported horizontally to the installation site with the aid of tugboats. Upending is achieved by gradually flooding the lower compartments with water. This is followed by a controlled ballasting process, in which the water is replaced by a solid ballast to stabilize the structure vertically. Finally, the wind turbine is mounted onto the upended platform. The first implementation of this concept was the Hywind Demo, installed in the North Sea in 2009.

The semi-submersible foundation consists of three or four buoyant columns spaced apart and interconnected by horizontal braces. This design offers enhanced hydrodynamic stability compared to the spar foundation, particularly in rough sea conditions. Due to its superior stability, the semi-submersible platform can often be assembled entirely onshore and towed to the installation site in a vertical position, simplifying logistics and reducing installation costs. An example of this approach is the WindFloat 1 project, deployed in Portugal in 2011.

Figure 2.7 – Tugboat towing a Semi-submersible wind turbine. (Principal Power)

The TLP is a floating structure characterized by excess buoyancy and vertical mooring, designed to remain vertically stable through the use of taut tendons. Unlike spar and semi-submersible platforms, TLPs are not yet widely commercialized for offshore wind applications due to the complexity of their anchoring systems and installation procedures. The installation process begins with the deployment of the tendons, which are fixed to the seabed in advance of the platform's arrival. The fully assembled wind turbine, mounted on the TLP, is then towed to the installation site. Upon arrival, the platform is partially ballasted to achieve the correct draft and positioned over the pre-installed tendons. These tendons are subsequently connected to the platform and tensioned by progressively removing ballast, leveraging the platform's inherent buoyancy to apply vertical pre-tensioning forces. This configuration minimizes vertical displacements and ensures a stiff response to environmental loading.

2.5. Anchors

To ensure the stability of FWTs and prevent uncontrolled translational movement of the platform under environmental forces such as wind and ocean currents, anchoring systems have been developed as a critical component of the mooring infrastructure. The use of anchors dates back to the early development of maritime vessels, where stability was initially achieved by deploying heavy structures to secure ships in position. Over time, more efficient anchor designs emerged, beginning with drag anchors, which offered higher capacity-to-weight ratios. Building upon these foundational concepts, anchoring systems for FWTs were developed to meet the specific demands of offshore environments and loading conditions.

Currently, a wide range of anchor types has been developed, each with its own specific characteristics tailored to different applications. These anchors vary in terms of soil compatibility, capacity-to-weight ratio, load-bearing capacity, installation procedures, and overall efficiency. The selection of an appropriate anchoring solution depends on various factors, including geotechnical conditions, environmental loads, and the operational requirements of the floating structure.

2.5.1. Gravity Anchor

One of the most basic types of anchors is the gravity anchor, which consists of a heavy object, typically constructed from steel or concrete, that resists movement of the floating wind turbine (FWT) primarily through its self-weight.

The installation process often necessitates the use of heavy-lift cranes for transportation and placement on the seabed, making this anchor type less suitable for inclined or irregular seafloor conditions.

The main advantages of gravity anchors include the potential for on-site fabrication, reliable bearing capacity derived from their own weight, straightforward mooring line connection and inspection, and effective performance in hard seabed conditions.

However, gravity anchors also present notable limitations. Their lateral load resistance decreases significantly with increasing seabed inclination, and they offer relatively low lateral capacity compared to other anchor types, except in hard grounds. Additionally, their size is constrained by the lifting capacity of available crane vessels.

2.5.2. Drag Anchor

Drag anchors are steel structures available in various shapes, designed to resist the movement of floating wind turbines (FWTs) primarily through friction and the passive resistance of the soil. Unlike gravity anchors, drag anchors, and the other types discussed subsequently, are classified as embedded anchors.

The installation process is relatively straightforward: the anchor is first deployed onto the seabed by an Anchor Handling Vessel (AHV) and then dragged across the seabed to penetrate the soil. The depth of embedment is determined by the configuration of the anchor, particularly the angle between the fluke and the shank.

The advantages of drag anchors include a wide variety of types and sizes, high load-bearing capacity, ease of recovery, and the ability to maintain resistance even after reaching maximum capacity.

However, drag anchors also present certain limitations. They exhibit low resistance to vertical loads and can behave unpredictably in layered soils. The dragging process may damage pre-existing seabed infrastructure, and their performance in rocky or hard seabed conditions is generally poor. Additionally, their capacity decreases significantly on seafloor slopes greater than approximately 6 degrees.

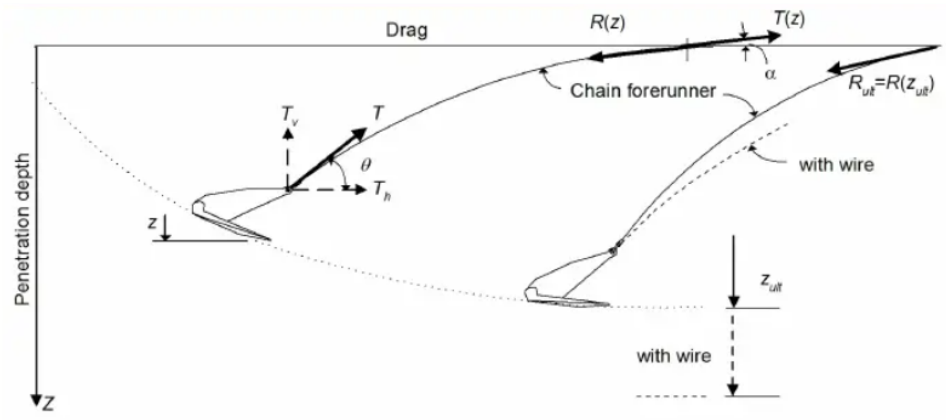

Figure 2.8 – Drag anchor installation (DNV GL – 2017 – Design and Installation of Fluke Anchors)

2.5.3. Pile Anchor

Pile anchors function similarly to foundation piles and are typically composed of steel hollow pipes that are either driven or drilled into the seabed and subsequently grouted. These anchors generally exhibit a length-to-diameter (L/D) ratio greater than 10. Due to their installation complexity, specialized equipment is required, which increases overall costs. Additionally, the driving or drilling phases may negatively impact marine life.

The installation process begins with the transportation of the steel pipes to the designated site. Two primary methods of embedment are commonly employed: either driving the pile into the seabed using a hydraulic hammer, similar to monopile installation, or drilling a borehole into which the pile is inserted and then grouted. The grout is injected under pressure from the bottom to the top of the pile cap and may be applied in stages along the pile shaft.

Among the advantages of pile anchors are the well-established design methodologies and installation practices, cost-effectiveness when compared to gravity, drag, and plate anchors, and robust performance under vertical loads.

However, pile anchors also have notable drawbacks. They are non-recoverable once installed, and although they are cost-effective compared to some alternatives, the initial installation cost can still be considerable. Furthermore, successful application requires detailed geotechnical investigation and a more comprehensive understanding of subsurface conditions than is necessary for gravity or drag anchors.

2.5.4. Plate Anchor

Plate anchors consist of large steel plates deeply embedded in the seabed, designed to resist external loads primarily through the weight and confining pressure of the overlying soil. These anchors have been extensively utilized in regions such as the Gulf of Mexico, where deep penetrations of up to 25 meters are common.

The installation process begins with the vertical insertion of the plate into the soil to significant depths. This initial embedment can be achieved through various methods, including driving, vibrating, jetting, or dragging. Once the desired depth is reached, the anchor is reoriented, typically rotated, to maximize its bearing surface area, thereby enhancing its load-bearing capacity. However, in hard ground conditions, this reorientation may not be feasible, resulting in a bearing capacity that is governed predominantly by shaft friction.

The main advantages of plate anchors include their high capacity-to-weight ratio, ability to resist both vertical and lateral loads, and reliable performance on inclined seabed.

Nevertheless, these anchors also present some limitations. They are generally non-recoverable, perform poorly under cyclic loading in coarse silt or loose sand, and the anchor cable is prone to fatigue over time.

2.5.5. Suction Anchor

Suction anchors are cylindrical steel structures with an open bottom, typically ranging from 3 to 8 meters in diameter and featuring a length-to-diameter ratio (L/D) between 3 and 6. The mooring line is connected at a specific location along the skirt, referred to as the padeye position, which significantly influences the anchor's load-bearing capacity, depending on the angle between the mooring line and the horizontal axis. Similar to pile anchors, this angle affects the performance under combined vertical and lateral loading.

The installation process of suction anchors is considered one of the simplest among embedded anchors. Initially, the anchor is placed on the seabed and begins to penetrate under its self-weight. Once self-penetration ceases, the top cap is vented to release the trapped water inside the cylinder. Subsequently, water is pumped out from the anchor, generating a pressure differential that facilitates further embedment into the soil. Once the desired depth is reached, the top cap is sealed.

Suction anchors offer several advantages: they possess high vertical and lateral load capacities, are fully recoverable, and may be shared among multiple floating wind turbines. They are suitable for both shallow and deepwater applications, compatible with various mooring systems, and involve a relatively simple and cost-effective installation process compared to other embedded anchors.

However, some limitations must be noted. Suction anchors generally exhibit a lower capacity-to-weight ratio than drag anchors, making them heavier for the same resistance. Installation in hard soils can be challenging or even unfeasible. Moreover, there is a notable lack of standardized design guidelines and recommended practices, particularly for cohesionless soils such as sands.

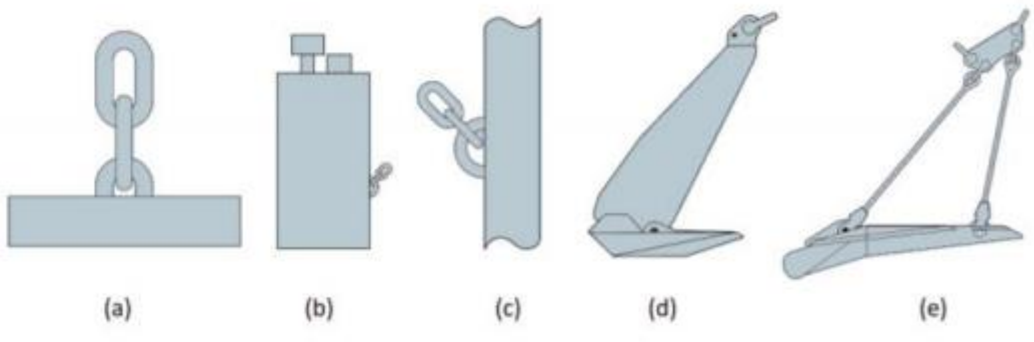

Figure 2.9 – Anchor types: a) Gravity anchor, b) Suction anchor, c) Pile anchors, d) Drag anchors, e) Plate anchors (VRYHOF MANUAL, The Guide to Anchoring)

A significant knowledge gap exists between floating and bottom-fixed wind turbine technologies, primarily due to the longer operational history and broader application of bottom-fixed systems. To address this disparity, continued research and development are essential to deepen the understanding of floating wind technologies. Bridging this gap is crucial, as a substantial portion of the world's offshore wind energy potential remains underutilized and unoptimized for large-scale energy production.

The performance of suction anchors in cohesive soils is well-established, supported by a substantial body of research and design guidelines, such as the DNVGL-RP-E303, which outlines recommended practices for the installation and design of suction anchors in clay. In contrast, the behavior of suction anchors in cohesionless soils remains poorly understood, with limited guidance available, thereby restricting their broader application in such environments. Although a few studies, such as those conducted by Zhao et al. (2018) and Cheng et al. (2021), have employed three-dimensional finite element (3D-FE) modeling to investigate suction anchor behavior in sandy soils, these analyses often use anchor geometries that do not correspond to commercially viable designs. Consequently, the current understanding of suction anchor performance under realistic geometric and soil conditions remains limited.

Given the considerable versatility of suction anchors, including their high vertical and lateral capacity, recoverability, and suitability for a range of mooring systems, this research aims to address the identified gap by analyzing their behavior in cohesionless soils using geometries representative of commercial practice. The primary objective of this study is to enhance the current understanding of suction anchor performance in sandy soils and to contribute toward the development of design methodologies suitable for such conditions.

2.6. Mooring system

Another critical component is the mooring line, which connects the floating structure, to the seabed ensuring positional stability under environmental loads such as waves, wind, and currents. The mooring system can vary in composition and may take the form of a tension leg, taut leg, or catenary shape, and for each one system will differ from two important conditions:

- The load angle range, for taut leg and for catenary this angle goes from 10º to 60º, imposing the caisson under load conditions such as horizontal capacity for angles close to 0º, and combined capacity for angles between 0º and 90º, while in the tension leg, only the vertical capacity condition is request.
- The load position, for taut lad and catenary system, the load can be attached along the skirt length of the caisson, on the other hand for tension leg, the load always is attached in the top cap of the caisson.

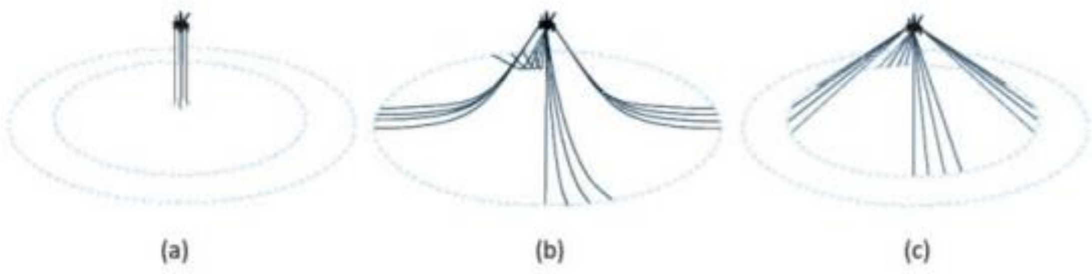

Figure 2.10 – Mooring systems: a) Tension Leg, b) Catenary, c) Taut Leg (VRYHOF MANUAL, The Guide to Anchoring)

The mooring lines themselves are typically made from three categories of materials: steel chain, wire rope, and synthetic fiber rope.

Steel chains, made from high-grade carbon or alloy steel, are widely used due to their high strength and durability. They provide excellent abrasion resistance and are often used in the lower sections of the mooring line that are in contact with the seabed. However, their considerable weight can contribute to high vertical loads on the anchor.

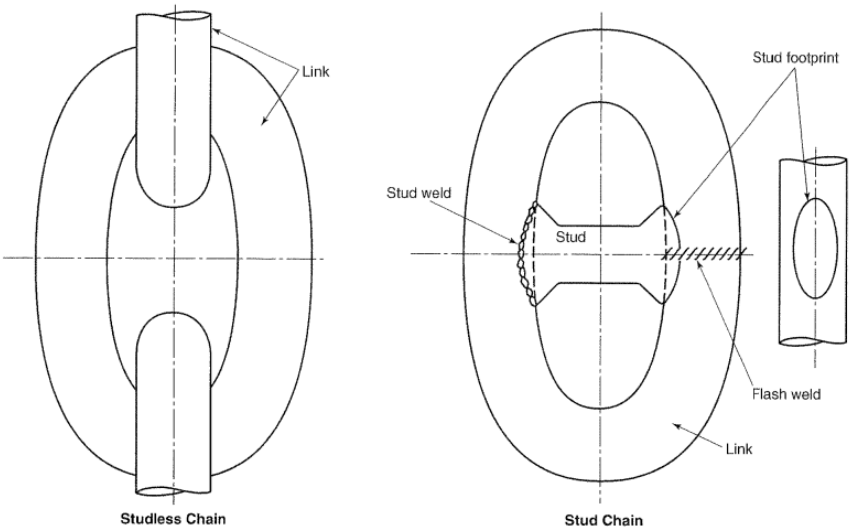

Figure 2.11 – Steel chains without and with stud respectively, (API RP 2SK, 2005)

Wire ropes, generally made from galvanized or corrosion-protected steel, offer a lighter alternative with good tensile strength and flexibility. Nevertheless, they are more vulnerable to fatigue and corrosion, particularly under dynamic loading conditions.

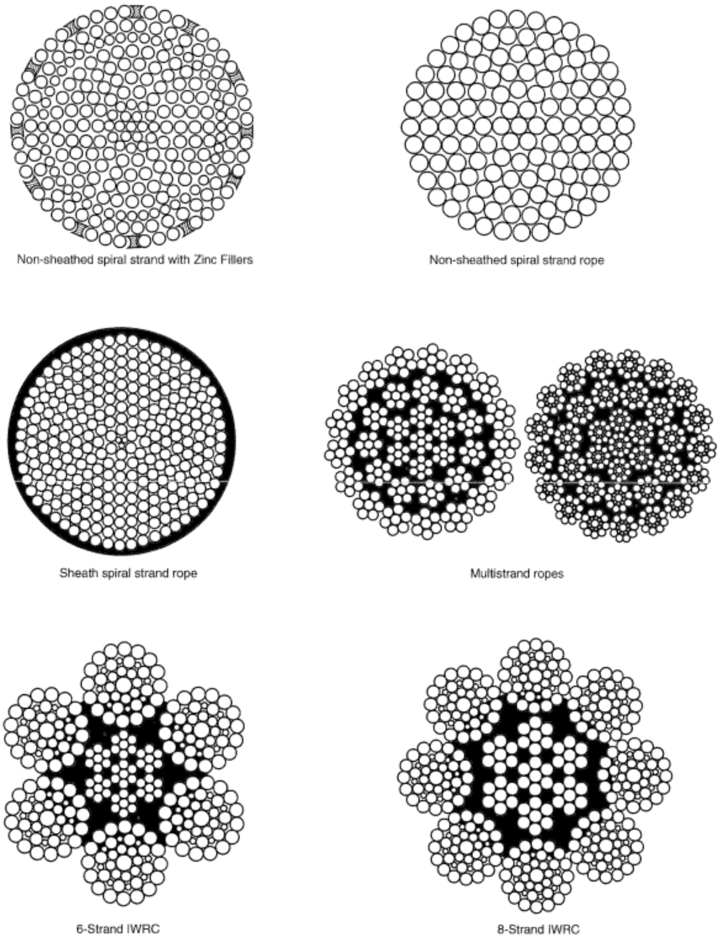

Figure 2.12 – Different types of wire ropes (API RP 2SK, 2005)

Synthetic fiber ropes, typically made from materials such as polyester, nylon, or aramid, are increasingly used in modern offshore applications. They are extremely lightweight, resistant to corrosion, and exhibit excellent fatigue performance. Polyester ropes, in particular, are preferred for their elasticity and creep resistance, making them ideal for deepwater mooring systems (S. Rui et al., 2024).

Figure 2.13 – Synthetic fiber ropes (All Lifting, “Different types of fiber rope”, 2019)

A common design approach is to use a hybrid mooring line, where chain segments are placed near the anchor and/or platform for abrasion resistance and weight, while synthetic or wire rope is used in the middle sections to reduce the overall weight and improve dynamic response (Wenyue Lu, 2021).

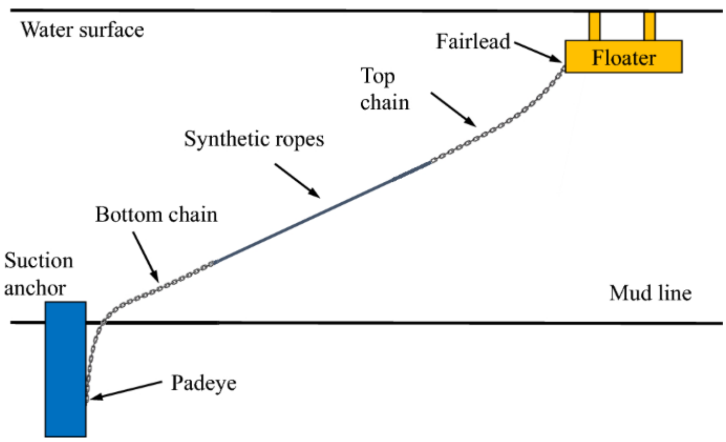

Figure 2.14 – Hybrid configuration of mooring line (Wenyue Lu, 2021)

The selection of mooring line materials and configuration is a key factor in ensuring the long-term performance, safety, and cost-effectiveness of floating offshore systems. When combined with reliable anchoring solutions such as suction caissons, well-designed mooring systems contribute significantly to the operational integrity and economic viability of floating energy infrastructure.

3
SUCTION ANCHORS

3.1. Introduction

Suction anchors, also known as suction caissons, are a widely adopted foundation solution for offshore structures such as floating wind turbines, subsea manifolds, and mooring systems. While their behavior in cohesive soils, particularly clays, has been extensively studied and is relatively well understood, their performance in cohesionless soils remains a topic of ongoing research. This is especially important in shallow marine environments and nearshore areas, where sandy seabed is predominant.

Two major design challenges arise in the context of suction anchors: the installation process and the load capacity under various loading conditions, vertical, horizontal, and inclined. The absence of a standardized design framework for cohesionless soils complicates the safe and efficient application of suction anchors in such conditions. Existing guidelines, such as those provided by the API RP 2GEO and DNV-RP-E303, are largely focused on cohesive soils, and their direct application to sandy environments can lead to conservative or non-conservative designs.

Given the increasing relevance of offshore renewable energy and the growing need for deployable and efficient anchoring systems in diverse seabed conditions, it is imperative to better understand and characterize the behavior of suction anchors in sands.

3.2. Suction Anchor Structure and Behavior

As previously mentioned, suction anchors are cylindrical steel caissons with varying diameter-to-length ratios (λ = L/D). They are composed of a padeye, where the mooring line is attached. The padeye position (L_p) is critical for the behavior of the suction anchor. It determines whether the anchor will rotate forward, backward, or not rotate at all for a certain load angle(θ).

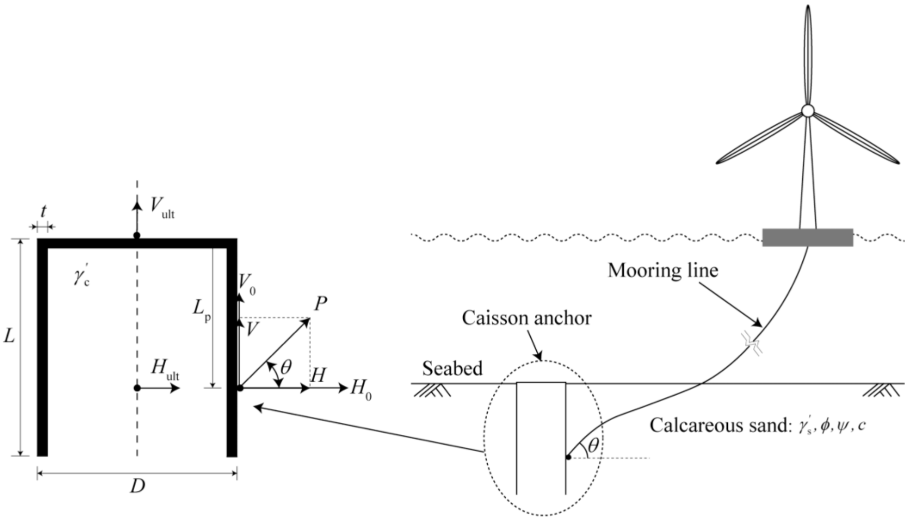

Figure 3.1 – Suction anchor structure system (Cheng et. al, 2024)

The load angle imposed on a suction caisson depends on the configuration of the mooring system that connects the floating foundation to the anchor. This angle is not constant, as it varies with the tension in the mooring line. Additionally, the surrounding soil interacts with the mooring chain, a phenomenon referred to as chain-soil interaction, which can enhance the overall resistance. However, the progressive development of this interaction may lead to soil deformation in front of the suction anchor, potentially resulting in trench formation. This trenching effect alters the stress state of the soil adjacent to the anchor, which can significantly reduce the anchor's load-bearing capacity (Rui et al., 2023).

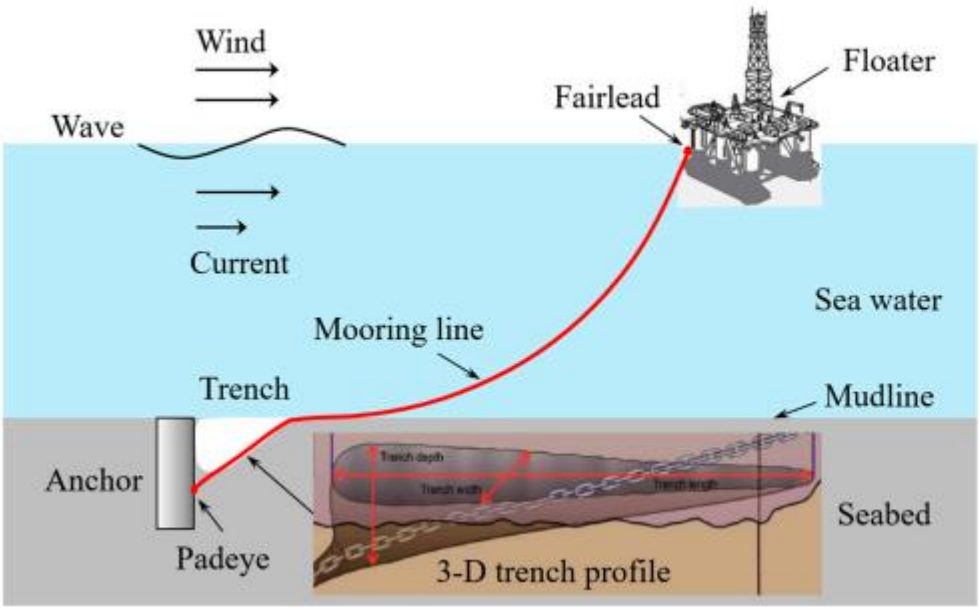

Figure 3.2 – Trench in front of the suction anchor (Rui et al., 2023)

The padeye position plays a critical role in determining the failure mechanism during loading. Depending on the relative depth at which the load is applied (usually represented by the dimensionless parameter $z_{pad} = L_p/L$), the anchor may exhibit different responses:

- Rotational failure (forward or backward).
- Translational pull-out.
- Combined mechanisms.

In normally or lightly over-consolidated clays, an optimal range for the load application point, typically where the line of action intersects the centerline of the caisson between 65% and 70% of its total embedment depth, has been identified. Within this range, suction caissons tend to exhibit non-rotational behavior under inclined loads, allowing for maximum horizontal load capacity to be mobilized, according Susan Gourvenec and Mark Randolph in “Offshore Geotechnical Engineering”.

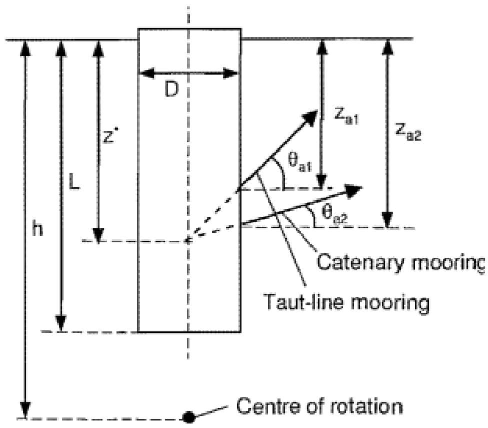

Figure 3.3 – Example of intersection of the centerline and line of action (“Offshore geotechnical engineering”, Mark Randolph and Susan Gourvenec)

For suction anchors embedded in sand and subjected to horizontal loading, their behavior can be categorized into three distinct modes, depending on the position of the padeye, the point of attachment of the mooring line, relative to the caisson height: above, below, or at the optimum padeye position. Each configuration results in a different failure mechanism:

- Padeye Above the Optimum Position: The caisson tends to rotate clockwise, lowering the center of rotation. This motion leads to the formation of a soil wedge in front of the caisson, causing local uplift of the soil.
- Padeye Below the Optimum Position: The caisson rotates counterclockwise, raising the center of rotation. This induces uplift in the soil in front of the caisson and promotes a curved sliding mechanism in the soil behind it.
- Padeye at the Optimum Position: The line of action of the applied load passes through the center of rotation, resulting in a predominantly translational movement of the caisson with minimal rotation. This configuration yields the maximum horizontal load capacity.

For caissons subjected to vertical loading, the failure mechanism remains consistent regardless of the padeye position. In all cases, the caisson exhibits a counterclockwise rotation, and the uplift capacity remains effectively the same. This indicates that, under vertical loads, the position of the mooring line attachment does not significantly influence the anchor's ultimate load-bearing behavior.

For caissons subjected to inclined loading, the anchor behavior varies depending on the padeye position. However, for a loading angle of 30°, there exists an optimal range, typically between 60% and 70% of the skirt length depth, that provides the maximum pullout capacity. Cheng et al. (2021) observed that this optimal padeye position is not fixed but instead varies with the aspect ratio (L/D) of the caisson; specifically, as the aspect ratio increases, from 1 to 1.5 to 2, the optimal padeye depth also increases accordingly.

When a caisson is subjected to lateral loads, the primary load transfer mechanism involves passive and active lateral earth pressures. Under horizontal loading applied at the optimum padeye position, the caisson tends to translate horizontally. This motion induces passive earth pressure on the front side of the caisson and active earth pressure on the backside. In contrast, when the caisson is subjected to vertical loads, load transfer occurs primarily through shaft resistance, which results from the interaction between the skirt length (both internal and external surfaces) and the surrounding soil. In sandy soils, this resistance is governed mainly by the interface friction angle (δ) and the lateral earth pressure coefficient (K), allowing for the estimation of shaft resistance in granular materials. Chapter 4 will provide a more detailed explanation of both loads.

In dense sands, dilatancy effects can increase effective stresses around the caisson, leading to higher resistance, particularly under slow loading rates. However, in loose sands or under rapid loading, the development of pore pressures and potential soil softening can reduce capacity.

Figure 3.4 – Suction anchor structure (Offshore magazine – "Suction anchor in place for Karish FPSO offshore Israel")

3.3. Suction Anchor Advantages

Several features aimed at enhancing the functionality of suction anchors have been the subject of ongoing discussion. One notable advantage is the potential to share a single suction anchor among multiple floating systems, thereby reducing overall costs and improving resource efficiency, an approach made feasible by their high vertical and horizontal load-bearing capacity. Furthermore, the relatively simple installation and retrieval process, especially when compared to other embedded anchors, represents a considerable benefit, particularly for temporary or semi-permanent offshore structures, as it contributes to reduced operational costs. Lastly, suction anchors exhibit a high degree of adaptability to varying soil types, water depths, loading conditions, and mooring configurations, enabling reliable performance across a wide range of offshore environments.

However, certain disadvantages may hinder the broader application of suction anchors. These include challenges associated with installation in hard ground conditions, a relatively lower capacity-to-weight ratio compared to drag anchors, and the necessity for detailed geotechnical characterization, often requiring advanced laboratory testing, to inform accurate design and performance predictions.

Several research topics remain under investigation regarding suction anchors embedded in sand, including the effects of cyclic loading, chain–soil interaction, anchor shearing, torsional behavior, among others.

These features make suction anchors particularly attractive for floating offshore wind turbines, where multiple turbines may share a common mooring system, enhancing cost-effectiveness and structural efficiency.

4
ANALYSIS METHODOLOGIES

4.1. Introduction

A considerable amount of research has been conducted on the behavior of suction anchors in cohesionless soil. The findings of these studies have culminated in the formulation of analytical and empirical solutions, as well as simplified theories, which are aimed at predicting the behavior of suction anchors.

The methodologies will be divided into two sections. The first section will be an analysis of the vertical capacity, and the second section will be an analysis of the horizontal capacity.

For the vertical capacity, three different analyses were conducted by Hirai (2023). These analyses were based on Janssen (1895), the limit equilibrium equations, and the "silo effect."

Zhao et al. (2018) conducted a three-dimensional finite elements(3D-FE) analysis. This analysis validated his model with the analytical solution of Houlsby et al. (2005). In the study conducted by Cheng et al. (2021), a 3D-FE analysis was employed to consider the relativity density of the soil. This analysis was then compared with the study by Houlsby et al. (2005).

The horizontal capacity will be explained through an empirical solution based on the behavior of lateral rigid piles capacity. The text will also present some results and behaviors achieved by Zhao et al. (2018) and Cheng et al. (2021).

4.2. Vertical Capacity

All the analytical models analyzing the vertical capacity of the axisymmetric model only consider the vertical load applied on the top cap of the caisson, therefore analyzing only the vertical translation of the caisson, and his behavior in the soil.

Subsequently, the behavior of the caisson will be examined in greater detail. This examination will include the application of load to the lateral skirt of the caisson, as well as a consideration of the caisson rotation.

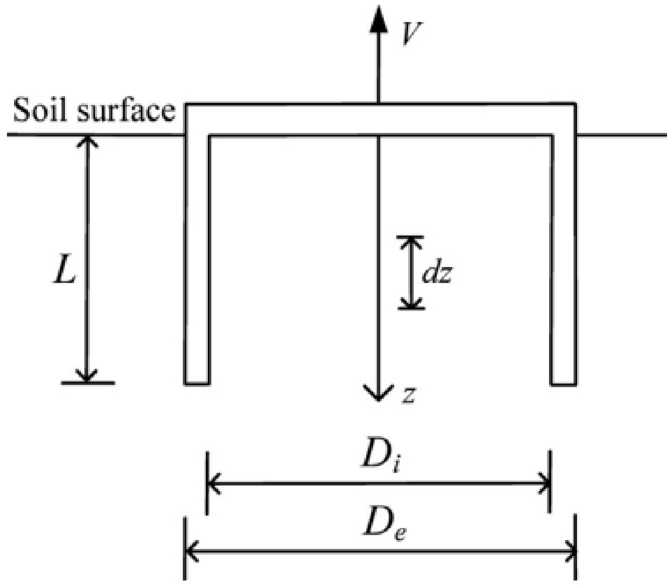

Figure 4.1 – Vertical load applied in the axisymmetric model and for the development of analytical solutions

4.2.1. HIRAI (2023)

In his work Hirai analyzes the behavior of the capacity of a suction anchor in sand, considering Equation (1), representing a limit equilibrium equation presented by Janssen (1895). He develops the vertical yield resistance of the soil inside and outside the suction caisson, which considers the ultimate tensile load capacity. Considering A_i, the area of the disk, dz an infinitesimal depth, σ'_{zi} an effective vertical pressure inside the skirt, γ' the effective soil weight, D_i as the internal diameter, D_e, as the external diameter, as follows Figure 4.2.

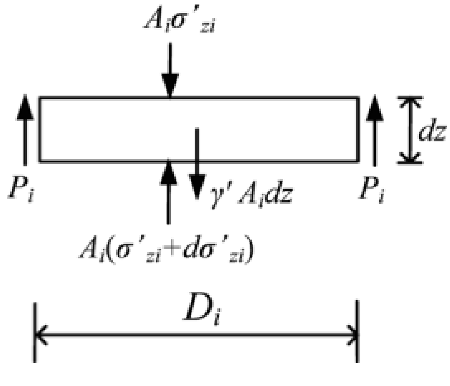

Figure 4.2 – Vertical equilibrium of an infinitesimal disk inside the caisson

The equilibrium solution is given by

$$\frac{d\sigma' zi}{dz} = \mu\sigma' zi + \gamma' \qquad (1)$$

Where, σ'_{zi} is an effective vertical pressure inside the skirt, and

$$\mu = -\frac{4K\tan\delta}{Di} \quad (2)$$

where K is the coefficient of lateral pressure, and δ the interface angle between the soil and the caisson.

The solution of equation 1 was given by

$$\sigma' zi = \frac{\gamma'}{\mu(e^{\mu z} - 1)} \quad (3)$$

In Equation 3, it was shown that the effective vertical stress of the soil within the caisson reaches a state of saturation with increasing depth. This phenomenon, commonly referred to as the "silo effect" and originally described by Janssen (1895), differs fundamentally from the behavior of fluids, in which the pressure at the bottom of a structure increases linearly with depth. In granular materials, however, this linear relationship does not apply. Instead, friction between the soil and the structure walls causes a redistribution of vertical stresses, limiting the rate at which pressure increases with depth. This effect was first observed experimentally using granular materials such as corn, where it was noted that the bottom pressure does not scale linearly with the total weight of the material above. As illustrated in the figure below, while a liquid exhibits a one-to-one linear pressure distribution, granular materials demonstrate a logarithmic increase in stress with depth, eventually reaching a plateau or "saturation" level.

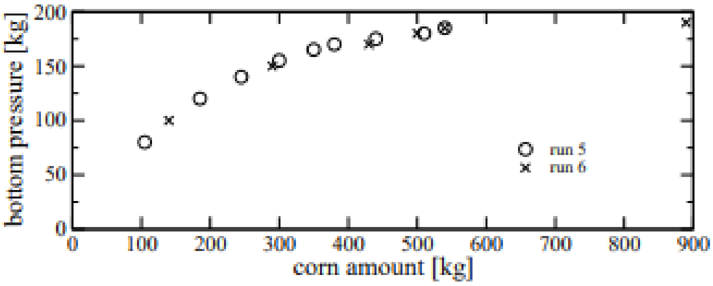

Figure 4.3 – Exemple of the silo effect, Janssen (1895)

Therefore, the vertical yield resistance of the soil outside the skirt, $P_{vye}(z)$, and that of the soil inside the skirt, $P_{vyi}(z)$, was written as:

$$P_{v_{ye}}(z) = K\tan\delta\,\sigma'_{ze}\pi D_e \quad (4)$$

$$P_{v_{yi}}(z) = K\tan\delta\,\sigma'_{zi}\pi D_i \quad (5)$$

And integrating the solution for a caisson with depth going from 0 to L, under a vertical load, the solution of the integral can be written as

$$V_t = \frac{\gamma'\pi D_i^{\,3}(e^{\mu L} - 1)}{16K\tan\delta} + \frac{\gamma'\pi D_i^{\,2} L}{4} + 0.5\gamma'\pi D_e L^2 K\tan\delta + W_c \quad (6)$$

Where W_c is the buoyant weight of the caisson, not considered in the integration of the vertical yield resistance outside and inside but applied at the end of the final solution to be a part of a resistance force.

4.2.2. ZHAO (2018)

Zhao, on the other hand, developed a correlation between the analytical solution proposed by Houlsby et al. (2005) and 3D-FE analysis.

The soil model of the numerical model was a Mohr-Coulomb criterion yielding, using parameters of Table 1.

Table 1 – Soil parameters of Zhao et al. (2018) analysis

Soil Parameters	Value	Units
Apparent cohesion (c)	0.1	kPa
Poisson's ratio (v)	0.3	-
Effective unit weight (γ')	9-11	kN/m^3
Dilation angle (ψ)	2	º
Peak friction angle (φ_{pk})	40	º
Critical-state friction angle (φ_{cv})	32	º
Coefficient earth pressure at rest (K_0)	(1-sin φ_{cv})	-
Relative density (D_r)	83	%

The numerical analyses were made using Abaqus/Implicit of a semicylindrical, taking advantage of the symmetry. A 3m to 5m outside diameter caisson (D_o), with a skirt thickness (t) of 0.1m were conducted to the analytical calculation with different aspect ratios of 0.5, 0.8 and 1. The interface friction angle for the surfaced aluminum usually ranges between 0.5-0.7δ/φ_{pk}, therefore a value of 0.6 was adopted in the analysis.

Using the soil stress level factor, and an ultimate vertical capacity proposed as, V_{ult}/W, a linear correlation between them was reached, and an agreement with the Houlsby solution. The soil stress level factor is written as Equation (7), and the Houlsby solution is written as equations 8-10:

$$k = \frac{\gamma' \lambda D_o}{p_a} \tag{7}$$

Where λ is the ratio between the length and the diameter, and p_a atmospheric pressure.

$$V_f = \gamma' \pi (K \tan \delta) \left[D_o {Z_o}^2 \left(e^{-\frac{L}{Z_o}} - 1 + \frac{L}{Z_o} \right) + D_i {Z_i}^2 \left(e^{-\frac{L}{Z_i}} - 1 + \frac{L}{Z_i} \right) \right] \tag{8}$$

Where Z_o and Z_i are written as Equations (9) and (10), respectively

$$Z_o = \frac{D_o(m^2 - 1)}{4(K \tan \delta)} \tag{9}$$

$$Z_i = \frac{D_i}{4(K \tan \delta)} \tag{10}$$

where m is the load-spreading parameter to account for vertical stress reduction in the soil outside the caisson.

After varying the diameter, aspect ratio of the caisson, and soil effective weight, the numerical results reached show a linear correlation of those two parameters, which was expressed as

$$\frac{V_{ult}}{W} = 0.73\, K \tan\delta \frac{p_a}{\gamma'_c t} k + 1.0 \tag{11}$$

where γ'_c is the effective weight of the caisson, t is the thickness of the caisson, K equal to the K_0 value, and V_{ult} the ultimate vertical capacity of the suction anchor.

The caisson geometries considered in this study offer valuable insights into the expected behavior of suction anchors. However, they do not fully reflect commercially available configurations, which may result in differences in performance, particularly when comparing caissons with higher aspect ratios to those with lower ones.

4.2.3. CHENG (2021)

Cheng et al. (2021) conducted an analysis that considered the relative density of the soil, using a Modified Mohr-Coulomb (MMC) model, leading to equations that were analogous to those of Zhao et al. (2018). However, Cheng et al. (2021) analysis considered the relative density, which underwent modifications throughout the developmental process.

The Modified Mohr-Coulomb (MMC) model is adopted, wherein the friction and dilation angles vary with the deviatoric plastic strain. This variation in the sand's friction angle enables both expansion and hardening, as well as contraction and softening of the failure surface in the q–p′ plane (deviatoric stress vs. mean effective stress). The initial friction angle, which corresponds to the in-situ stress condition, φ_{ini} is assumed to be equal to the critical state friction angle, φ_{cv}.

Table 2 - Soil parameters of Cheng et al. (2021) analysis

Soil Parameters	Value	Units
Apparent cohesion (*c*)	0.1	kPa
Poisson's ratio (v)	0.3	-
Effective unit weight (γ')	9	kN/m^3
Dilation angle (ψ)	1	º
Peak friction angle (φ_{pk})	$16D_r^2 + 0.17D_r + 28.4$	º
Critical-state friction angle (φ_{cv})	32	º
Coefficient earth pressure at rest (K_0)	(1-sin φ_{cv})	-
Relative density (D_r)	40, 60, 80	%

One of the investigations that he conducted was to determine the ultimate vertical capacity. This capacity was expressed through the analytical solution proposed by Houlsby et al. (2005), as presented in Equation (10):

$$V_{ult} = V_f + W_s \tag{12}$$

Where W_s is the weight of the caisson submerged in water, V_f is the frictional resistance along the soil-caisson interface, being the same formulation as Equation (8). In a similar manner to the research conducted by Zhao et al. (2018), Cheng et al. (2021) utilized the normalized ultimate vertical capacity, denoted by V_{ult}/W_s, to conduct a series of calculations. These calculations incorporated various aspect ratios of the caisson, distinct sand relative densities, and different diameters. The normalized ultimate vertical capacity was then plotted as a function of the soil stress level factor, designated as η.

The equation that demonstrated the greatest congruence with the findings of the numerical analysis and Houlsby et al. (2005) was Equation (11), expressed as follows:

$$\frac{V_{ult}}{W_s} = 0.8\, {D_r}^{0.17} K \tan\delta \frac{p_a}{\gamma'_c t}\eta + 1.0 \tag{13}$$

Considering the K as K_0 value, the thickness as t, equal to 0.1m, the caisson diameter as D, going through 4 to 8, and the aspect ratio from 1 to 2.

4.3. Horizontal Capacity

For the ultimate lateral capacity to be achieved, it is necessary that the suction anchor translate horizontally without rotation, being empirically estimated using the method developed for a rigid pile by integrating the limiting lateral resistance of the soil along the caisson depth

$$\frac{H_{ult}}{\gamma' D_o L^2} = \frac{N}{2} \tag{14}$$

Where N is the lateral capacity factor, which is a function of the passive soil pressure coefficient,

$$K_p = \frac{1 + \sin\varphi}{1 - \sin\varphi} \tag{15}$$

A variety of numerical simulations varying the diameter of the suction caisson, the effective soil weight, and the caisson length must be performed to arrive at an empirical factor that correlates with the lateral capacity factor and the soil stress level factor.

5
PYTHON SCRIPTS

5.1. INTRODUCTION

To perform multiple numerical analyses efficiently and consistently, and to extract large volumes of data under varied conditions, Python scripts were developed using the PLAXIS 2D Remote Scripting API. This interface, based on the *plxscripting* module, allows direct manipulation of PLAXIS 2D models, facilitating automated model generation, execution of calculation phases, and extraction of output results. This automation ensures reproducibility, minimizes human error, and significantly reduces modeling time when exploring a wide parameter space.

5.2. MODEL STRUCTURE AND WORKFLOW

Two models were developed for different purposes: an axisymmetric model, used for validation of vertical capacity under central loading conditions, and a plane strain model, used to investigate the anchor's behavior under vertical, horizontal and inclined loads.

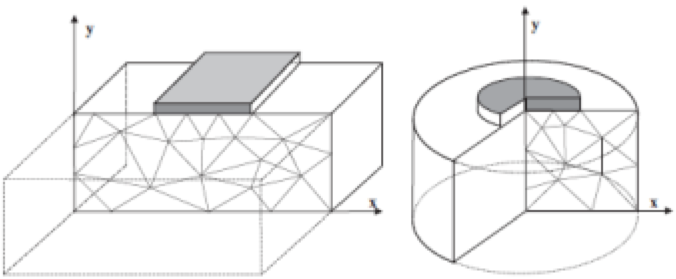

Figure 5.1 – A plane strain(left) and an axisymmetric(right) problem

Both models have the same core structure, but each one has specific adaptations aligned with its mechanical representation that will be shown with the following sub-chapters. To proceed with this comparison between the analytical solutions and the model, a Python script was made with the following structure:

- Project definition: model title, working units (kN, m), model type (axisymmetric or plane strain), and element type are established.
- Geometry generation: soil domain boundaries and anchor geometry are defined according to input parameters.

- Soil definition: a borehole is created, and the soil layer is assigned with appropriate mechanical and hydraulic properties. The definition of the suction anchor and applying the properties of the material.
- Anchor definition: the suction anchor geometry is generated parametrically, with varying dimensions (diameter, length) and aspect ratios.
- Interface assignment: plate elements are used to simulate the anchor wall, with interfaces applied on both sides to model soil-structure interaction.
- Load application: a point load is applied at the padeye location to simulate loading under vertical, horizontal or inclined conditions.
- Meshing strategy: the mesh is automatically refined near the anchor using a defined cluster, ensuring greater accuracy in regions of high stress gradients.
- Phases creation: different construction stages are defined, including the initial conditions, installation of the anchor, null phase, and loading phase.
- Water level specification: phreatic level is applied to simulate submerged conditions.
- Model calculation: execution of all phases and retrieval of output results (e.g., displacements, forces, failure mechanisms).

5.2.1. Axisymmetric model

The axisymmetric model was designed to validate the vertical load capacity of suction anchors under idealized central loading. The soil domain was constructed with dimensions scaled to the caisson diameter (5 times the diameter horizontally and 2 times the length vertically).

The mesh consists of 6-noded triangular elements, and a finer mesh cluster was generated within a radius of 1 time the diameter laterally and 1.5 times the length beneath the caisson. Multiple analyses were conducted by varying the caisson's diameter, length, and soil unit weight, aiming to compare the numerical results with analytical formulations presented in Chapter 4.

5.2.2. Plane strain model

The plane strain model was adapted to investigate horizontal and inclined loading scenarios, reflecting the horizontal and vertical components of the loads applied in the soil. The same general modeling flow was followed, with modifications to account for 2D planar representation. A larger domain was used in order to involve all the possible failures of the caisson under horizontal loads with 30 times the diameter of the anchor horizontally, and 3 times the length of the caisson vertically, a detailed explanation will be developed in chapter 6. The main differences in this model are:

- The anchor is modeled as a long strip, representing a 2D projection of a cylinder.
- Inclined point loads are applied at specific angles to study the effect of loading direction on capacity and failure mode.
- Point loads applied on different depths of the skirt length, to analyze the behavior in different scenarios of load application.

The inclined load angle and padeye position were varied to assess their influence on anchor rotation and displacement, contributing to a better understanding of anchor performance under mooring-type loads.

5.3. DATA HANDLING

Data from each simulation is automatically extracted using Python commands that access PLAXIS Output parameters. The key outputs include:

- Horizontal and vertical displacement at the top cap of the anchor.
- Horizontal and vertical displacement at the point load.
- Total reaction forces mobilized, vertical and horizontal.
- Rotation of the anchor at the maximum force applied.
- The error of the calculation.

These outputs are stored in structured format, Data Frame, for further analysis and plotting. This process enables the generation of result table for parametric studies and the construction of failure envelopes or validation results with respect to analytical solutions.

For numerical analyses, a load-controlled procedure was adopted. In this approach, a target load magnitude is predefined, and PLAXIS 2D progressively increases the applied force through incremental steps until either the full target load is reached, or soil failure is detected. Throughout the calculation process, the percentage of the total load mobilized at last step is accessible via the PLAXIS Output API. This percentage is subsequently multiplied by the predefined total load, enabling reaches the load applied in the soil failure.

6
MODEL AND BEHAVIOR UNDER LOADS

6.1. INTRODUCTION

To investigate the behavior of suction anchors in various environmental and loading conditions, a comprehensive numerical analysis was conducted using the finite element method (FEM) in PLAXIS 2D. The primary objective was to evaluate the mechanical response of suction anchors under vertical and horizontal loads by employing both axisymmetric and plane strain models. These simulations were designed to approximate pseudo-3D behavior while encompassing a range of soil conditions and geometries representative of commercially used suction anchors.

This chapter presents a detailed description of the modeling approach, including the geometric configuration, boundary conditions, and the constitutive soil models applied. The analysis also includes a validation phase, where the results of the axisymmetric and plane strain models are compared against analytical formulations discussed in Chapter 4. Through this approach, the study aims to provide insights into the performance of suction anchors subjected to different loading directions, while also assessing the influence of geometry and soil properties on their behavior.

6.2. THE MODEL

As mentioned before, the software used was PLAXIS 2D, conducted by a FE analysis, two models for validation and for analyze the behavior of the suction anchor was made, the axisymmetric and the plane strain model, both used the same constitutive soil model, Hardening Soil model.

The properties of the soil are presented in Table 3, and the properties of the suction anchor are presented in Table 4, both models used the same properties of soil and suction anchor.

Table 3 – Soil properties of the model

Parameter	Value	Units
Mechanical Properties		
Soil Model	Hardening Soil (HS)	(-)
Drainage Type	Drained	(-)
Cohesion (c)	0.5	kN/m^2
Poisson's ratio (v)	0.3	(-)
Saturated unit weight (γ_{sat})	19.81	kN/m^3
E_{ur}^{ref}	36000	kPa
E_{oed}^{ref}	9700	kPa
E_{50}^{ref}	12000	kPa
Power m stress dependency	0.5	(-)
Dilation angle (ψ)	0	º
Friction angle (φ)	variable	º
Initial void ratio (e_{init})	variable	(-)
Minimal void ratio (e_{min})	0.35	(-)
Maximum void ratio (e_{max})	0.8	(-)
Coefficient earth pressure at rest (K_0)	variable	(-)
Interface Properties		
Strength determination	Manual	(-)
R_{inter}	0.8245	(-)
Real Interface Thickness	0.1	m

The drained type was selected, to represent a drained soil, a cohesion equal to 0.5kN/m^2 was used to avoid numerical instabilities, an unsaturated unit weight was considered the same as the saturated unit weight due to the ground water level, which is positioned 1 meter above the top boundary, the dilation angle was defined as 0°, the real interface thickness equal to 0.1m and the friction angles was selected in function of the relative density of the soil using the API (1972) equation as

$$\varphi = 16{D_r}^2 + 0.17D_r + 28.4 \tag{16}$$

In order to obtain a broad range of possible responses for this parameter, the relative density of the soil was varied between 40%, 60%, and 80%. This approach also aimed to assess the influence of different friction angles on the behavior of the suction anchors, given that variations in relative density are directly correlated with changes in the soil's shear strength parameters, particularly the internal friction angle (δ).

The coefficient of earth pressure at rest, K_0, was varied based on two assumed values, one derived from Jaky's empirical equation (Equation 17), and another fixed at 0.5. This approach was adopted to investigate the behavioral differences in load response under varying soil conditions.

$$K_0 = 1 - \sin\varphi \tag{17}$$

Another important parameter used in the calculations is the tan(δ), which is the interface friction angle, related to the R_{inter}, PLAXIS considers this value as the following equation:

$$R_{inter} = \frac{\tan\delta}{\tan\varphi} \tag{18}$$

Table 4 – Suction anchor properties

Parameter	Value	Units
General		
Material Type	Elastic	(-)
Unit weight(W)	6.869	kN/m/m
Mechanical Properties		
Isotropic	True	(-)
EA	210×10^{11}	kN/m
EI	17.5×10^{9}	kNm^2/m

The unit weight of the suction anchor was considered the submerged unit weight, a rigid body with an elastic module of E = 210E12 kN/m^2, and considering a thickness(t) of 0.1m, therefore the calculations of EA and EI are the following equations:

$$EA = E * t * b \tag{19}$$

$$EI = E * b * \frac{t^3}{12} \tag{20}$$

Always considering b = 1m, for plane strain and axisymmetric.

The analysis was conducted using a load-controlled approach, in which force was incrementally applied to the structure. A load advancement procedure was implemented by applying a small percentage of the total force and evaluating the corresponding soil response. Once the global stiffness parameter became negative, the load was reduced and reapplied. If this behavior occurred five consecutive times, the collapse of the soil was assumed to have been reached, based on the arc-length control method recommended in the PLAXIS 2D Manual. This point is considered indicative of the onset of soil plastification, and thus, failure. To ensure the applied force exceeded the plastification threshold, it was defined as a function of both the caisson's diameter and length, thereby increasing proportionally with geometric size. However, a maximum load of 150 kN was imposed to prevent excessive loading that could compromise the analysis by artificially influencing soil behavior. This constraint was necessary as the primary objective of the analysis was to investigate the monotonic response of the soil-anchor system.

6.2.1. Axisymmetric

The boundary conditions of the model were defined according to the requirements of each modeling strategy. For the axisymmetric model, the geometric domain was extended sufficiently to minimize boundary effects and ensure accurate simulation of soil-structure interaction. Specifically, the model radius was set to five times the caisson diameter (5D), while the vertical extent of the domain was established as twice the caisson length (2L).

To improve the numerical resolution in the vicinity of the suction anchor, a refined mesh cluster was generated around the caisson. This cluster extended radially to a distance of one caisson diameter (1D) and vertically to 1.5 times the caisson length (1.5L) below the skirt tip. This meshing strategy allows for better capture of stress concentrations and displacement gradients near the anchor while maintaining computational efficiency in regions less affected by loading, a coarseness factor of 0.1 was establish for the mesh creation within the cluster, and a factor of 1 outside the cluster, for the mesh creation a relative element factor of 0.67 was settled, equivalent to the fine mesh option.

The load application was defined as a purely vertical load, applied concentrically on the top cap of the caisson, aligned with the model's axis of symmetry. This setup facilitates the assessment of uplift capacity and vertical displacement behavior under monotonic loading conditions. The configuration of the model boundaries, the cluster lines and the mesh refinement zone are illustrated in Figure 6.1:

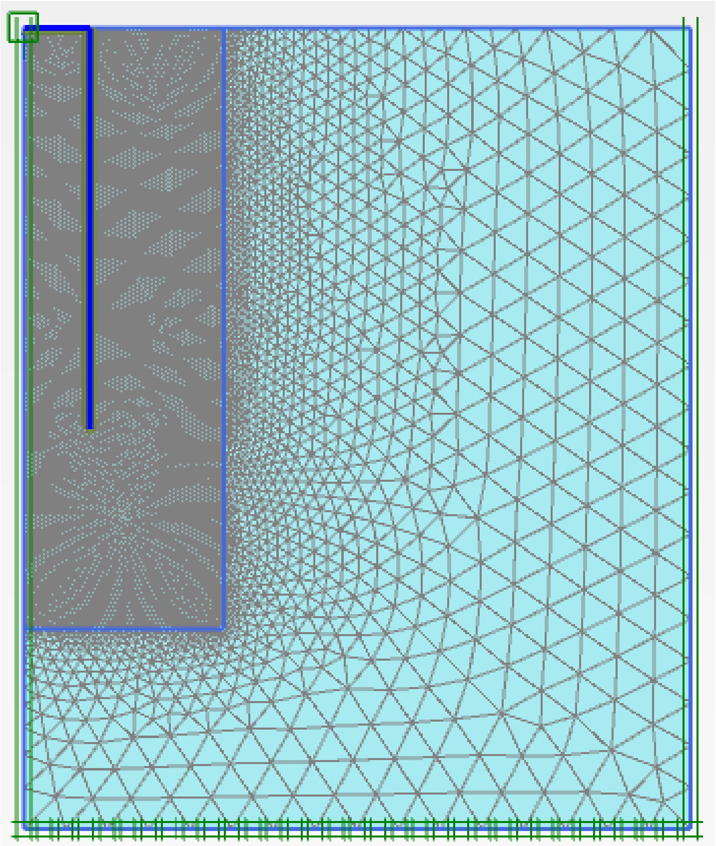

Figure 6.1 – Axisymmetric model in PLAXIS 2D

6.2.2. Plane Strain

For the plane strain model, a similar mesh refinement strategy was adopted through the implementation of a localized refined cluster around the suction anchor. However, due to the two-dimensional nature of the model and its inability to exploit axial symmetry, the boundary dimensions were extended considerably to avoid boundary effects and ensure a realistic simulation of stress propagation.

The initial model was defined with a horizontal extent of 12 times the caisson diameter (12D) and a vertical extent of 4 times the caisson length (4L), with the caisson positioned at the center of the domain following the configuration in previously studies on suction anchors in cohesionless soil in 3D-FEM Christian Jensen et al. (2023). However, significant interference from the lateral boundaries was observed when horizontal forces was applied, particularly when modeling caissons with varying geometries. To mitigate this, the model domain was extended to 30D in the horizontal direction and 3L in the vertical direction. Additionally, the caisson center was repositioned 12D from the left boundary to align with the direction of the applied load. This configuration ensures that the majority of the soil resisting the applied forces lies between the caisson's right skirt and the right model boundary. A spacing of 18D was maintained between the caisson center and the right boundary to accommodate aspect ratios ranging from 3 to 6. This adjustment effectively minimized potential boundary effects on the structural response of the anchor.

The mesh configurations used in the plane strain model were a coarseness factor of 0.1 inside the cluster, and a 0.25 coarseness factor outside the cluster, with a relative element size factor of 0.75, equivalent to a medium-fine mesh.

Regarding the refined mesh cluster, a similar vertical extension to that of the axisymmetric model was used 1.5 times the caisson length (1.5L) beneath the base of the caisson. For the lateral extension of the cluster (left and right sides), the distances were determined based on the theoretical failure mechanism of shallow foundations, as described in classical bearing capacity theory. This approach ensures that the refined mesh encompasses the most critical regions of stress concentration and plastic deformation, while maintaining a coarser mesh in peripheral areas to optimize computational efficiency.

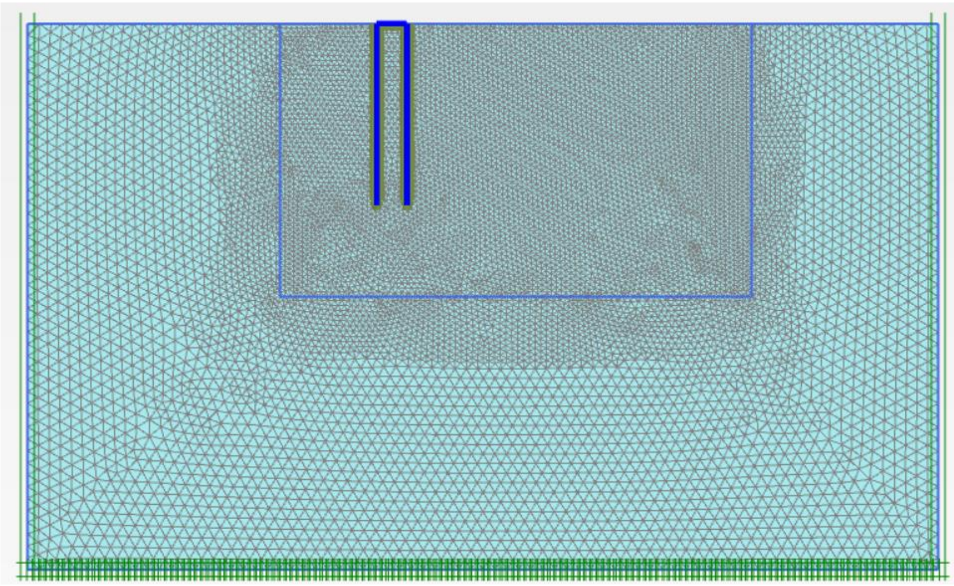

Figure 6.2 – Plane strain model in PLAXIS 2D

Considering the caisson embedded in the soil with all the length, a comparison with the failure mechanism of the shallow foundation is considered the depth of the radial section, d, as the length of the caisson, therefore the left side of the cluster is spaced by 2L/(tan(π/4+φ/2)), and the right side 1.2L/(tan(π/4-φ/2)).

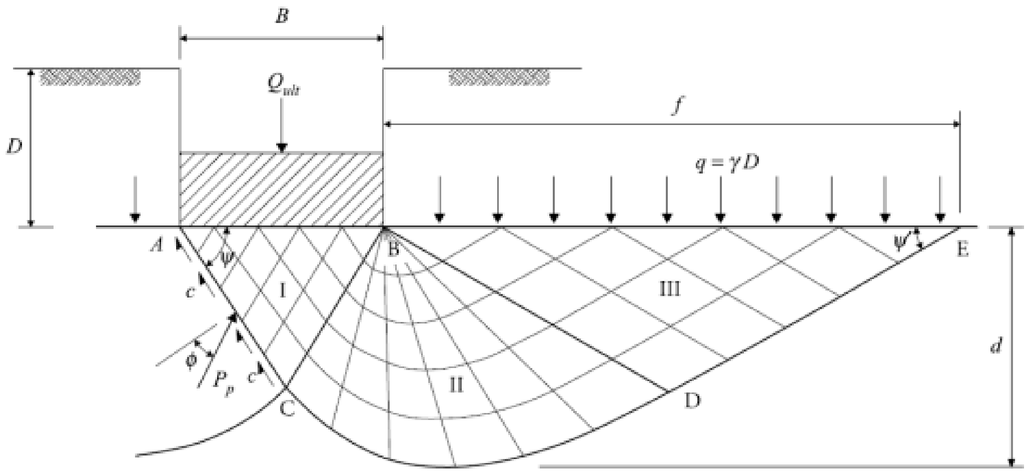

Figure 6.3 – Failure mechanism of a shallow foundation (Matos Fernandes, 2011)

6.3. VALIDATING THE MODEL

6.3.1. INTRODUCTION ABOUT CALCULATIONS

A series of calculations were made using different parameters such as the caisson diameter, length, unit weight of the soil and relative density to validate the model with the equilibrium and analytical equations, for the axisymmetric model under vertical loads.

The validation was made with the axisymmetric model, where the application of the equations was directly made, and, with the plane strain model, with the modification of the equations to a 2D plane strain model.

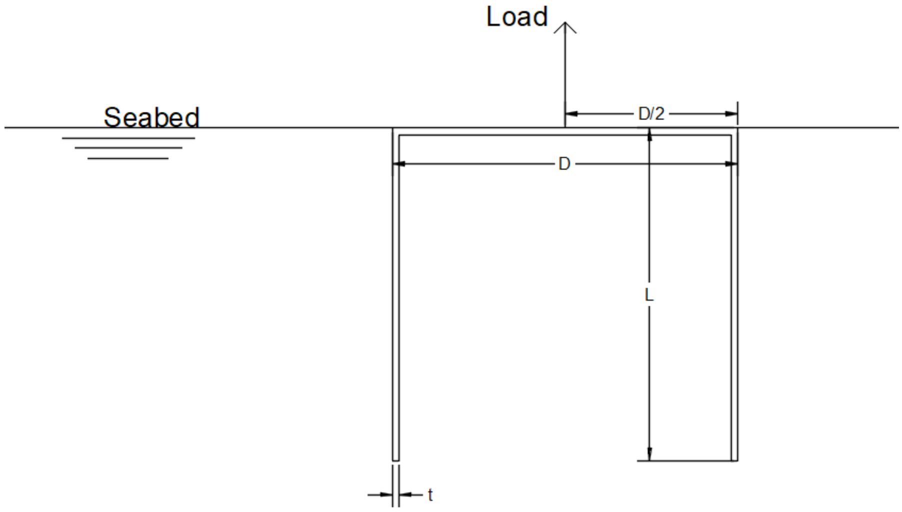

Figure 6.4 – Configuration of the suction anchor for the validation of the model

The equations used for validation are based on two distinct approaches: one proposed by Hirai (2023) and the other by Houlsby et al. (2005), which forms the basis for the studies conducted by Cheng et al. (2021) and Zhao et al. (2018). The main difference lies in the assumed soil behavior. Hirai (2023) considers that only the soil inside the anchor becomes saturated with depth, a phenomenon referred to as the "silo effect,". In contrast, Houlsby et al. (2005) assume that saturation occurs both inside and outside the anchor. These differing assumptions result in distinct vertical effective stress profiles. Under the silo effect, the increase in vertical effective stress follows a logarithmic trend and tends toward an "asymptotic" limit, thus constraining the vertical stress at greater depths. On the other hand, when no silo effect is considered, the vertical effective stress increases linearly with depth.

The aforementioned "silo effect" refers to the redistribution of vertical stresses with depth, where stresses do not increase linearly but instead stabilize at a limiting value. This occurs because vertical loads are partially transferred to adjacent structural elements through friction, generating a horizontal frictional reaction that reduces the vertical stress transmitted to the bottom of the anchor.

6.3.2. Axisymmetric

The caisson diameters considered in the validation process were 3m, 5m, and 8m, each analyzed with aspect ratios (L/D) of 3, 5, and 6. The corresponding results of vertical uplift capacity, are presented in Figure 6.4 as a normalized value, considering the uplift capacity divided by the weight of the caisson, and plotted with the soil stress level factor to represent each result for each variation of geometry and soil properties.

In the analytical calculations, the coefficient of lateral pressure (K) was initially determined using Jaky's formulation, Equation (17), which relates K_0 to the soil's internal friction angle. However, this approach led to minimal variation in the product $K\tan(\delta)$ across different friction angles. Consequently, the predicted uplift capacities exhibited limited sensitivity to changes in soil strength parameters, which does not align with the expected physical behavior of soil-structure interaction.

To overcome this limitation, an alternative approach based on the methodology proposed by Cheng et al. (2021) was implemented. In this revised framework, the K_0 value was held constant, equivalent to that obtained using Jaky's equation for a critical state friction angle(φ_{cv}). This allowed Ktan(δ) to vary with changes in the friction angle, better capturing the influence of soil strength on uplift capacity. A fixed K_0 value of 0.5 was adopted in the calculations, enabling a clearer assessment of the uplift response across different friction angles and enhancing the model's sensitivity to this key parameter.

Table 5 – Values of Ktan(δ) using K_0 = 1-sin(φ)

Relative Density (%)	Ktan(δ) (-)
40	0.24
60	0.245
80	0.248

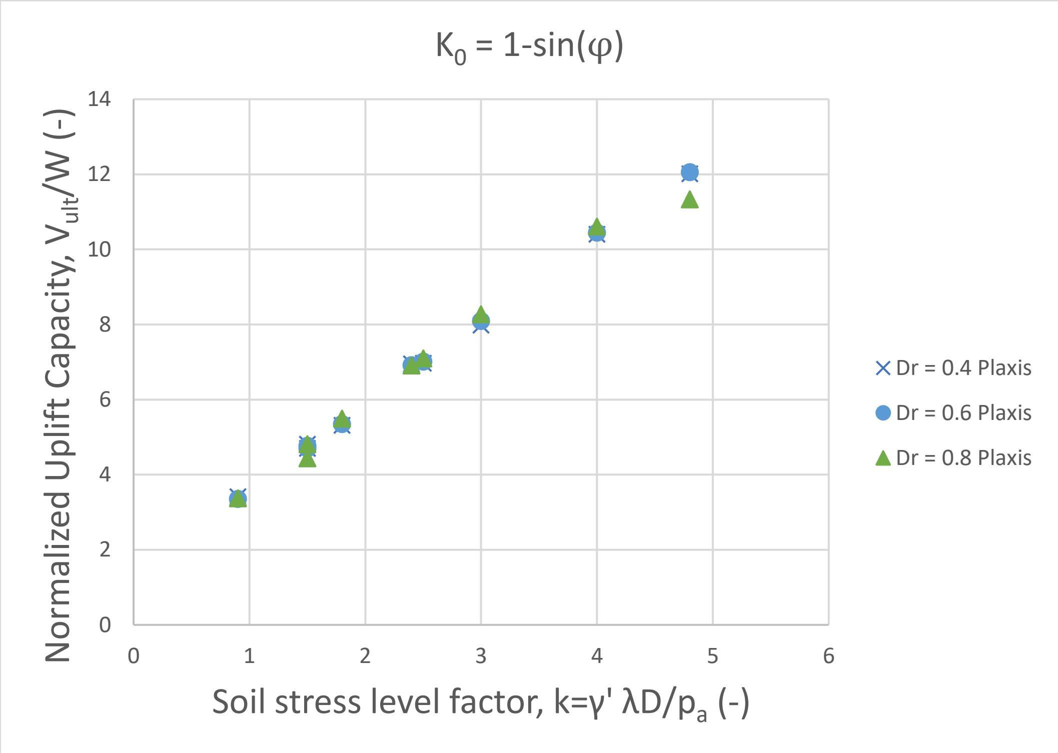

Figure 6.5 – Uplift capacity behavior using varied K_0 value

Therefore, to proceed with a consistent analysis varying the value of Ktan(δ), the following values were used for the following relative density, the final values of uplifting capacity also vary accordingly. As expected, increasing the relative density of the soil leads to an increase in the internal friction angle, and consequently, in the soil–structure interface angle. This trend directly influences the uplift resistance of the suction anchor and is illustrated in Figure 6.6.

Table 6 – Value of Ktan(δ) using K_0 = 0.5

Relative Density (%)	Ktan(δ) (-)
40	0.248
60	0.281
80	0.331

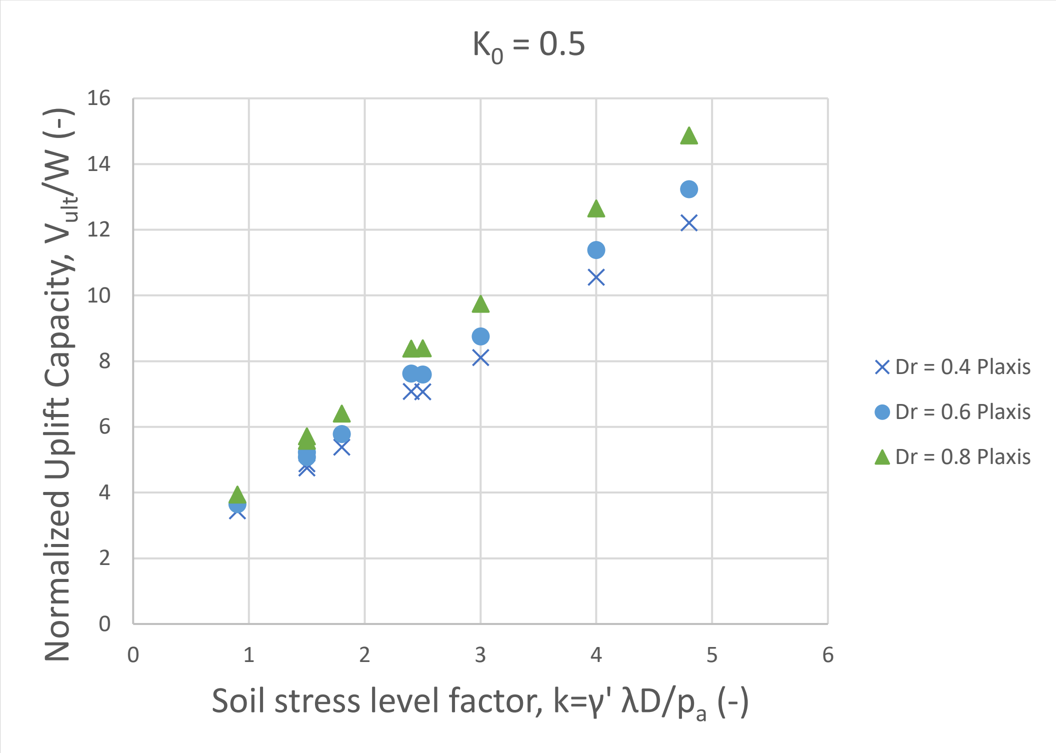

Figure 6.6 – Uplift capacity behavior using constant K_o value

A series of calculations was conducted to compare the results obtained from analytical equations with those derived from PLAXIS 2D simulations. The comparison highlights the differences in average error for each relative density. Notably, the equations proposed by Hirai exhibit significantly higher accuracy compared to the other formulations. It is also important to note that the equations by Cheng et al. (2021) and Zhao et al. (2018) do not consider the aspect ratios presented in the calculations here done, which conduct to high different values from the PLAXIS 2D calculations. The aspect ratio of the caissons from the studies was from 0.5 to 2.

Two key aspects must be considered when interpreting the results obtained from PLAXIS 2D simulations:

- The soil behavior influenced by the "silo effect."
- The approximation of the lateral pressure coefficient (K) and the coefficient of pressure at rest (K_0).

The soil–structure interaction modeled in PLAXIS 2D incorporates the most significant aspects of the “silo effect” within the interior soil of the anchor, following the same conceptual approach as the equation proposed by Hirai (2023). In contrast, the external soil behavior remains unaffected by the silo effect. Figure 6.7 illustrates the vertical effective stresses near the anchor, clearly showing the manifestation of the silo effect on the internal side, where the increase in vertical stress is attenuated. Meanwhile, on the external side, the vertical effective stresses increase linearly with depth.

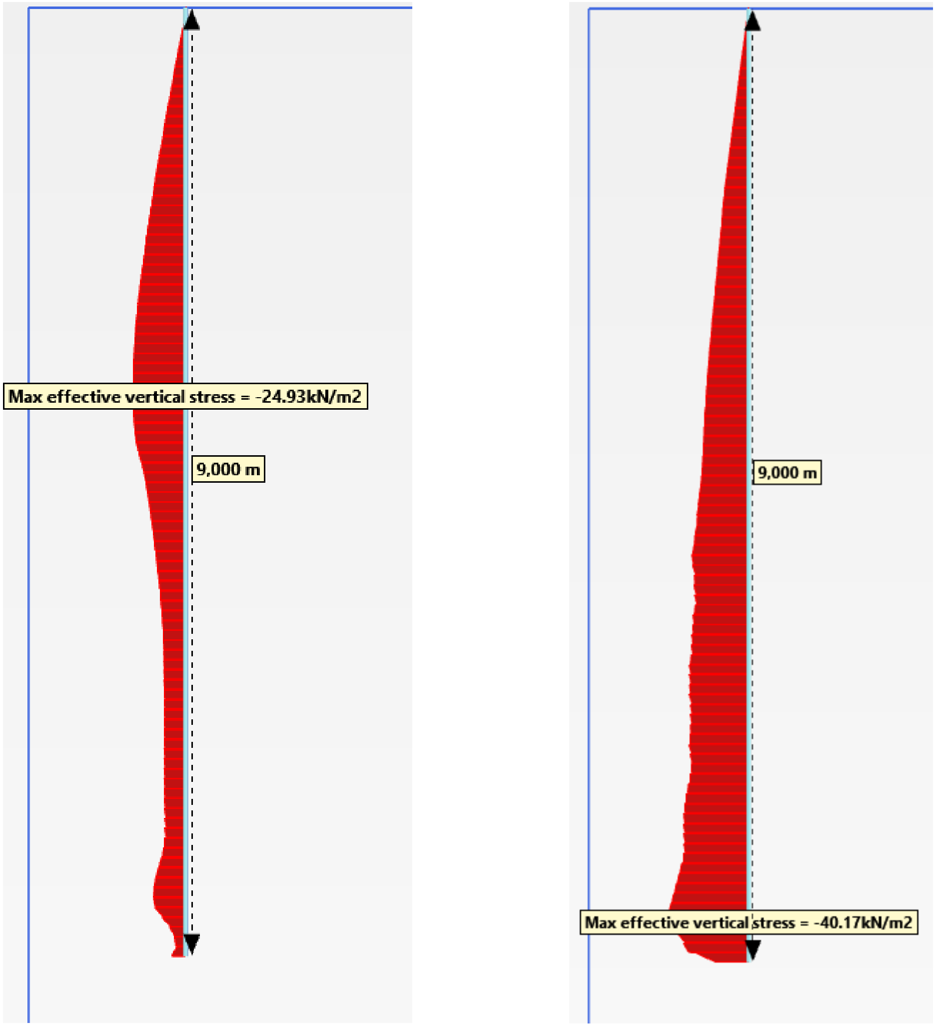

Figure 6.7 – Left side effective vertical stresses inside the caisson rigth side effective vertical stresses outside the caisson in a asymmetrical model

This process applies similarly across different caisson geometries and soil types. It is evident that in soils with higher relative density, the interface friction angle between the soil and the structure increases, resulting in a higher resistance mobilization.

Regarding the lateral earth pressure coefficient, two key observations were made:

- When a fixed lateral pressure coefficient at rest ($K_0 = 0.5$) was adopted, the computed values of K during the anchor installation phase showed a slight increase. In the axisymmetric model, the effective horizontal and vertical stresses (σ'_{xx} and $\sigma'_{\gamma\gamma}$) were assessed at a horizontal distance of 0.1 m from the caisson wall to avoid selecting stress points within the caisson. Measurements started at 0.5 m depth from the surface, analyzing 50 points along the caisson wall across various geometries and relative densities. An average K value of approximately 0.56 was obtained. Since the anchor was installed in a wished in place, the variation in K compared to K_0 remained minimal, for the K values within the caisson, the values are the same of the K_0.

- The majority of the mobilized shear resistance is concentrated near the base of the anchor. This implies that the upper portion of the caisson contributes little to no shear resistance before failure occurs. It is well established that the lateral earth pressure coefficient tends to be significantly higher near the surface and decreases with depth, eventually becoming lower than K_0.

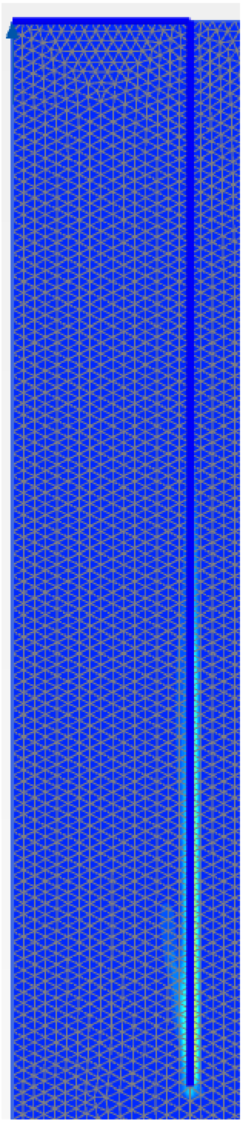

Figure 6.8 – Total deviatoric strain of a suction caisson in a axisymmetrical model under a uplift load

Considering these behaviors, and in the interest of optimizing computational time, the calculations adopted a simplified assumption of $K = K_0$.

In Table 7 below, a comparison of the error values among the three approaches can be analyzed, with the values from Hirai (2023) being clearly closer to the presented model behavior, reinforcing that the soil–structure interaction behavior is better represented by the analysis that considers the silo effect in the internal soil and the linear increase of vertical stresses with depth in the external soil.

Table 7 – Error between equations and PLAXIS 2D results for Axisymmetric model

Hirai (2023) error	Cheng (2021) error	Zhao (2018) error
	Dr = 0.4	
5.43±1.32	3.11±1.83	5.77±3.02
	Dr = 0.6	
4.01±1.36	8.79±3.87	8.42±3.86
	Dr = 0.8	
2.1±1.36	16.49±3.6	12.47±3.53

The errors between the PLAXIS 2D and the analytical results was calculated using the following equation:

$$Error = \left|\frac{Analytical\ Result - Numerical\ Result}{Analytical\ Result}\right| \times 100 \tag{21}$$

6.3.3. Plane strain

For the plane strain model, validation focused solely on uplift capacity, as lateral capacity assessments are inherently empirical. Accurate determination of lateral resistance requires full translation of the caisson to mobilize the ultimate capacity, a process that typically involves displacement-controlled analyses. This approach allows for controlling the caisson's rotation by prescribing displacements. In the context of 3D-FE analyses, several studies suggest that imposing a lateral displacement of approximately 10% of the caisson diameter provides a reasonable estimate for developing force–displacement curves without a plateau. However, this behavior has not been extensively investigated in 2D-FE models.

It is important to note that the current study employed a load-controlled approach, which allows the suction anchor to move freely in response to applied loads. Consequently, the lateral capacity values obtained are dependent on the chosen loading control method and may differ significantly from those obtained under displacement-controlled conditions. However, with a displacement-controlled analysis, the real behavior of the caisson is not represented.

Regarding the vertical capacity validation for the plane strain model, the comparison was again made using the formulations from Chapter 4. However, the Hirai (2023) equation required adaptation, as it was originally developed for axisymmetric conditions. Equations (11) and (13), which are primarily dependent on the caisson's unit weight, remained applicable with minimal modification. Therefore, replacing the caisson's unit weight with an equivalent plane strain unit weight was sufficient to estimate the ultimate vertical capacity under 2D conditions for Equations (11) and (13).

The adaptation process began with revisiting Equation (2), originally based on Janssen's (1895) formulation for a rectangular geometry, while Hirai's model assumes a cylindrical shape. Thus, Equation (2) was reformulated as:

$$\mu = -\frac{C_i K \tan\delta}{A_i} \tag{22}$$

Where C_i is the perimeter, and A_i is the area of the soil within the caisson. Proceeding through the equilibrium equations, the same theoretical framework applies under the plane strain assumption, with adjustments made to reflect the strip geometry of the caisson. Consequently Equation (4) and (5) are adapted as follows:

$$P_{v_{ye}}(z) = 2K \tan\delta\, \sigma'_{ze} \tag{23}$$

$$P_{v_{yi}}(z) = 2K \tan\delta\, \sigma'_{zi} \tag{24}$$

These expressions represent the external and internal vertical resistance, respectively, at a certain depth z. Assuming the skirt length of L, the total uplift resistance can be obtained by integrating Equations (22) and (23), considering Equation (3), which accounts for the saturation of the internal vertical pressure with depth:

$$V_{ult} = K \tan\delta\, \gamma' L^2 + \frac{2K \tan\delta\, \gamma'(e^{\mu L} - 1)}{\mu^2} - \frac{2K \tan\delta\, L}{\mu} + W_c \tag{25}$$

Therefore, with this equation an application was done for the comparison between the results of the plane strain model, calculations were conducted to validate the equation and the model. The same behavior of the $K_0 = 1 - \sin(\varphi)$ occurs with the plane strain model, therefore, the approach used in the axisymmetric model was employed to establish a correlation between the normalized uplift capacity and the soil stress level factor. The results of this comparison are shown below.

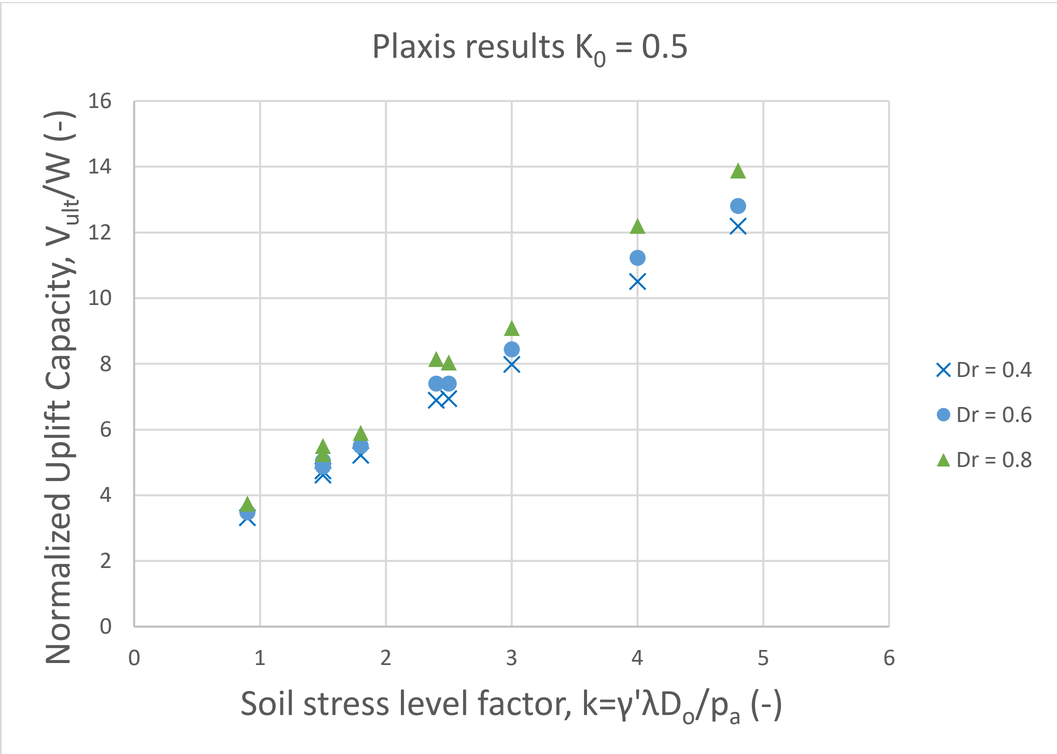

Figure 6.9 – Uplift capacity for plane strain model

The results can also be observed for different relative densities of the soil through the force–displacement curves presented below of a caisson with 3m of diameter and a $\lambda = 3$.

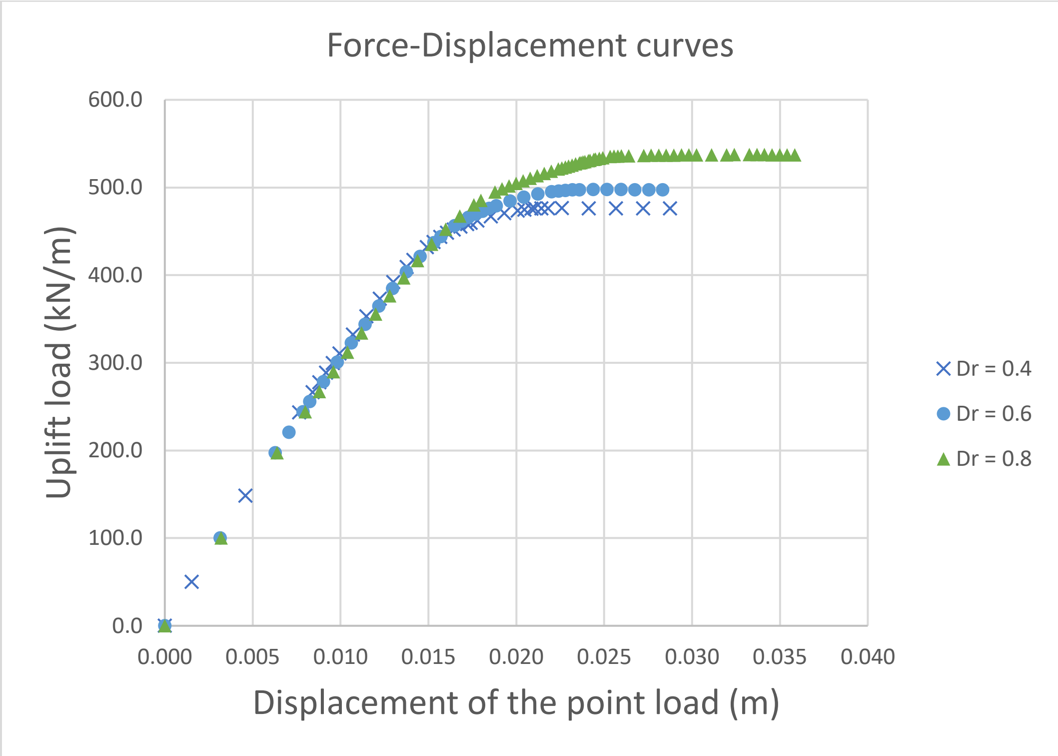

Figure 6.10 – Force-Displacement curves of a suction anchor with D=3m and L=9m

These findings indicate that the behavior of the suction anchor in the plane strain model is similar with that previously observed in the axisymmetric model. The adoption of a fixed value of K_0 = 0.5 in PLAXIS 2D resulted in a progressive increase in load resistance with increasing relative density of the soil, which aligns with both the axisymmetric results and the expected behavior of granular soils.

The "silo effect," previously identified in the axisymmetric simulations, is also evident in the plane strain model across all tested geometries and relative density levels. This reaffirms the numerical model's ability to replicate this characteristic behavior of confined soils within the caisson.

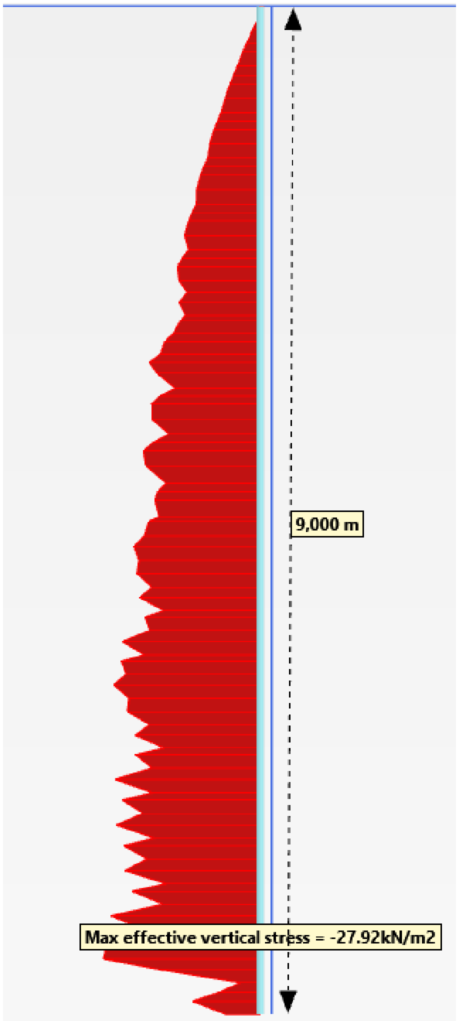

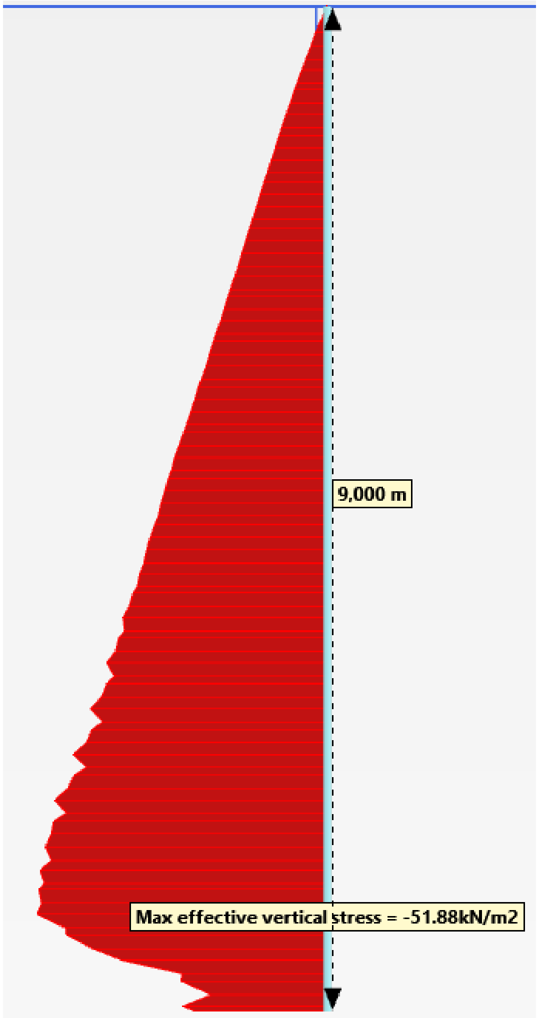

Figure 6.11 - Left side effective vertical stresses inside the caisson, rigth side effective vertical stresses outside the caisson in a plane strain model

As in the axisymmetric analysis, the deviatoric strain localizes predominantly near the bottom of the caisson, indicating that the mobilized shear resistance occurs primarily at depth, where the lateral earth pressure coefficient (K) approaches K_0.

It is important to note that the plane strain model generally produces higher levels of error compared to the axisymmetric model. This discrepancy arises because the axisymmetric model better represents the actual cylindrical geometry of the suction anchor with an open base, while the plane strain model idealizes the anchor as an infinitely long rectangular strip, thus tending to overestimate resistance values.

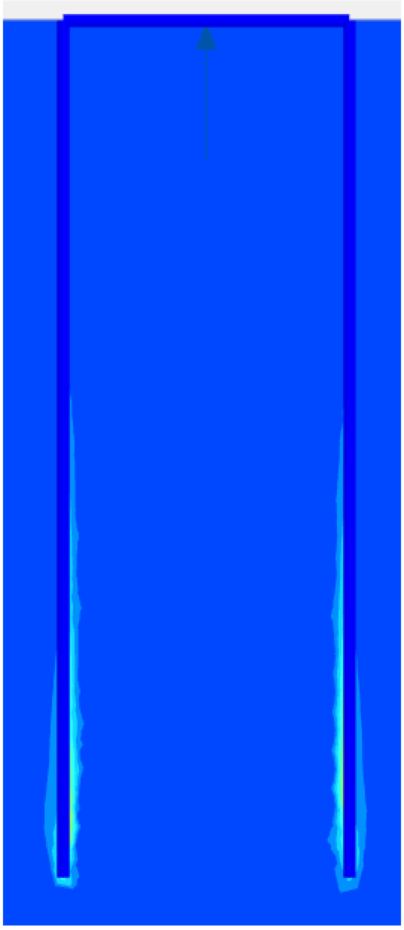

Figure 6.12 – Total deviatoric strain of a suction caisson in plane strain model under a uplift load

Table 8 – Error between equations and PLAXIS 2D results for Plane strain model

Hirai (2023) error	Cheng (2021) error	Zhao (2018) error
	Dr = 0.4	
2.5±0.88	3.06±1.62	7.36±2.85
	Dr = 0.6	
4.97±1.59	12.03±3.32	11.7±3.31
	Dr = 0.8	
8.19±2.11	20.8±3.93	17±3.92

By observing the values of V_{ult2D} (V_{ult} from the plane strain model) and V_{ult3D} (V_{ult} from the axisymmetric model) from the previous numerical analyses and comparing the non-dimensional vertical ultimate capacities $V_{ult2D}/(\gamma D^2)$ and $V_{ult3D}/(\gamma D^3)$, a standard curve was obtained in which the values were correlated, as shown in Figure 6.13.

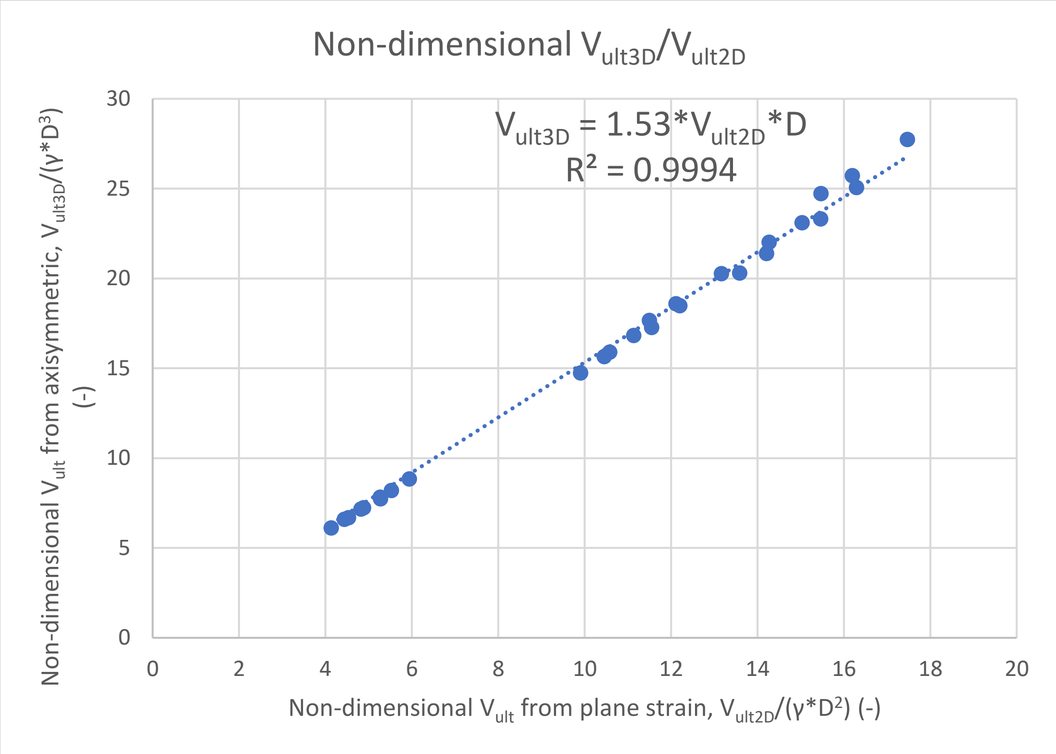

Figure 6.13 – Correlation between normalized V_{ult3D} and V_{ult2D}

It can be noted that there is a direct linearity between the normalized values, following $R^2 = 0.9994$, and a standard curve given by $V_{ult3D} = 1.53*V_{ult2D}*D$. This relationship was possible to establish between the plane strain and axisymmetric models; however, for evaluating the subsequent applied forces at z_{pad}, it was not possible to develop any relationship between the plane strain and axisymmetric models, since the formulation of the axisymmetric model with a force acting on the side of the anchor would be developed around the entire circumference, as can be seen in Figure 5.1.

6.4. Behavior under localized drag forces

6.4.1. Introduction

This chapter presents an analysis of the caisson's behavior under various loading conditions, using the previously validated plane strain model. The applied forces are evaluated along the skirt length of the caisson, with their positions defined by the normalized padeye depth, z_{pad}, expressed as the ratio between the load application depth, L_p and the total skirt length (L), i.e., L_p/L.

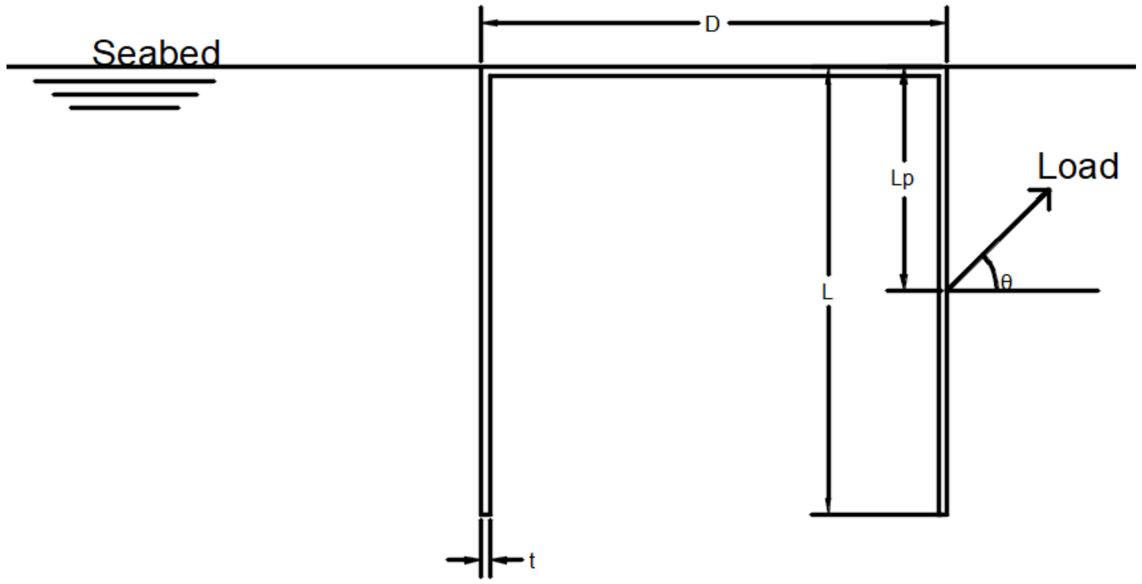

Figure 6.14 – Configuration of the suction anchor under loads attached on the skirt length

Vertical loads are defined as those applied at a 90° angle relative to the horizontal, while horizontal loads act at 0°, the objective is to determine the optimal padeye range and behavior under a plane strain model for vertical and horizontal loading conditions. The analysis includes suction caissons with a single commercial diameter due to the plane strain condition of the model, resulting in any difference in the behavior, assessed at minimum and maximum aspect ratios (L/D). The influence of relative density, and consequently the soil friction angle, was considered for each caisson geometry. Additionally, the effect of the coefficient of earth pressure at rest (K_0) was examined by comparing results using Jaky's formulation and a fixed value of $K_0 = 0.5$. Differences in load response under these varying conditions are presented for vertical and horizontal loading cases, along with the corresponding failure mechanisms.

6.4.2. Vertical forces

To analyze the vertical load response of suction anchors, specifically considering loads applied along the skirt length, with an eccentricity now considered, a 3 m anchor diameter was investigated. This analysis included λ of 3 and 6, enabling a comprehensive assessment of how geometry influences load behavior. The influence of different values of K_0, and the friction angle also was investigated to analyze the behavior under different soil conditions.

The normalized load application depth, represented by the z_{pad} (L_p/L), was varied across a range from 0.5 to 0.75. This range allowed for the examination of anchor behavior before the commonly recognized optimal padeye position (typically between 0.6 and 0.7), within this optimal range (including 0.6, 0.65, and 0.7), and after it. A substantial number of simulations were conducted to investigate the vertical load-bearing capacity of the suction anchors across these varying z_{pad} values. The results, derived from diverse input configurations, were graphically plotted to facilitate comparison and interpretation.

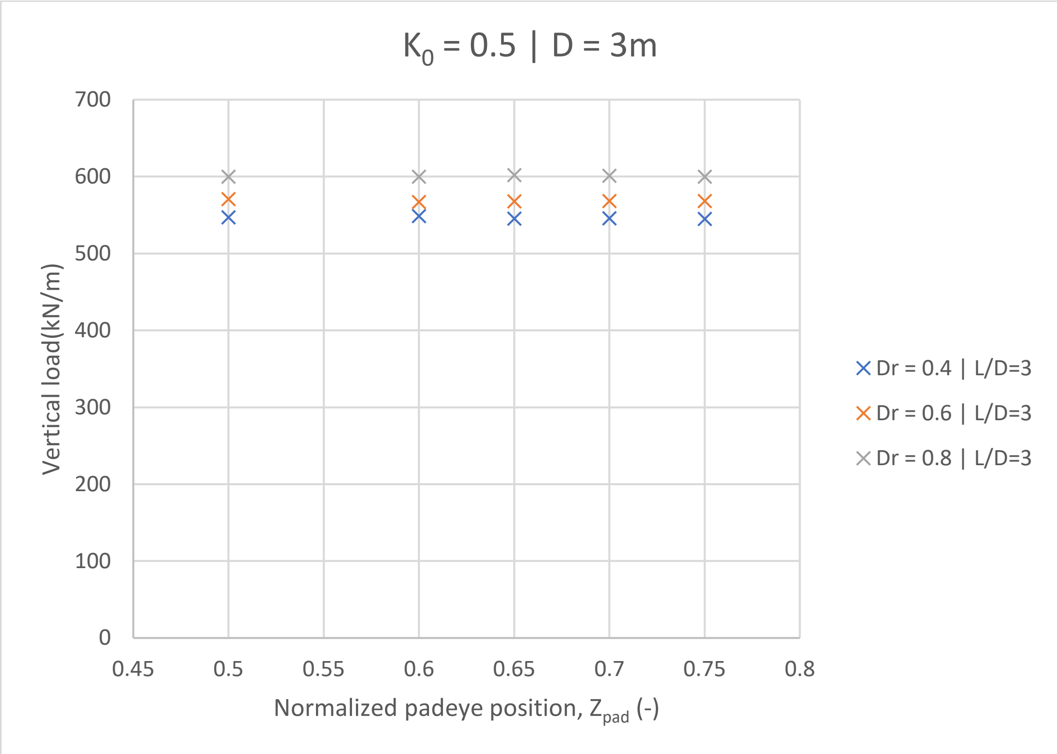

Figure 6.15 – Vertical loads applied on the skirt length with a fix K_0

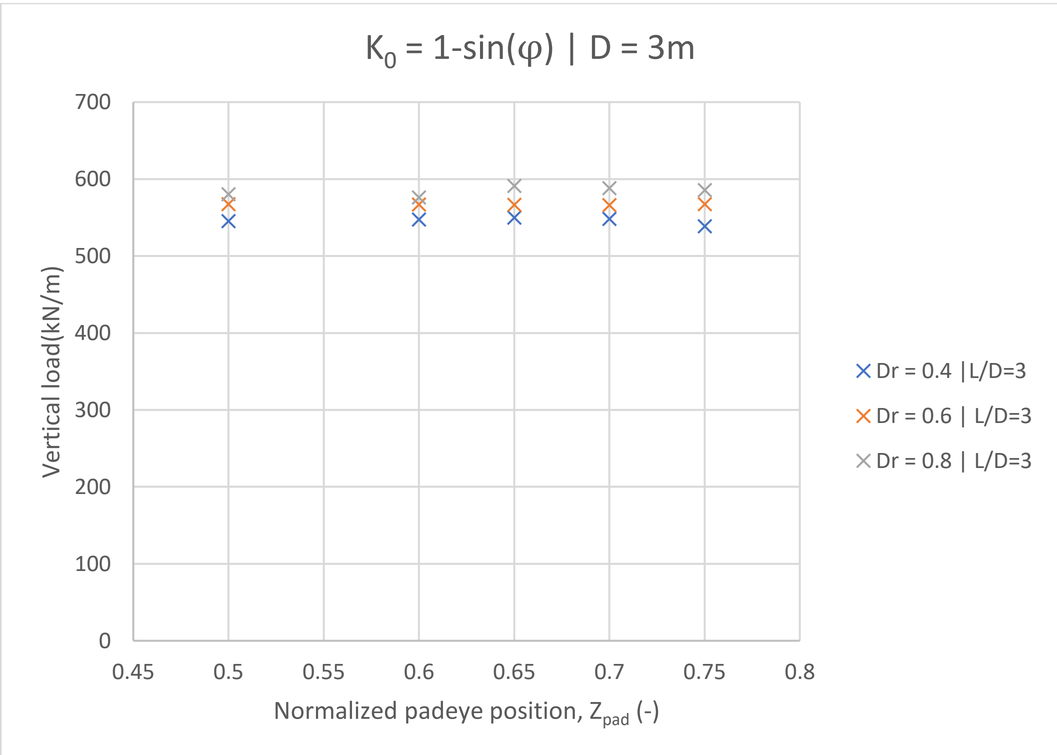

Figure 6.16 – Vertical loads applied on the skirt length with a variable K_0

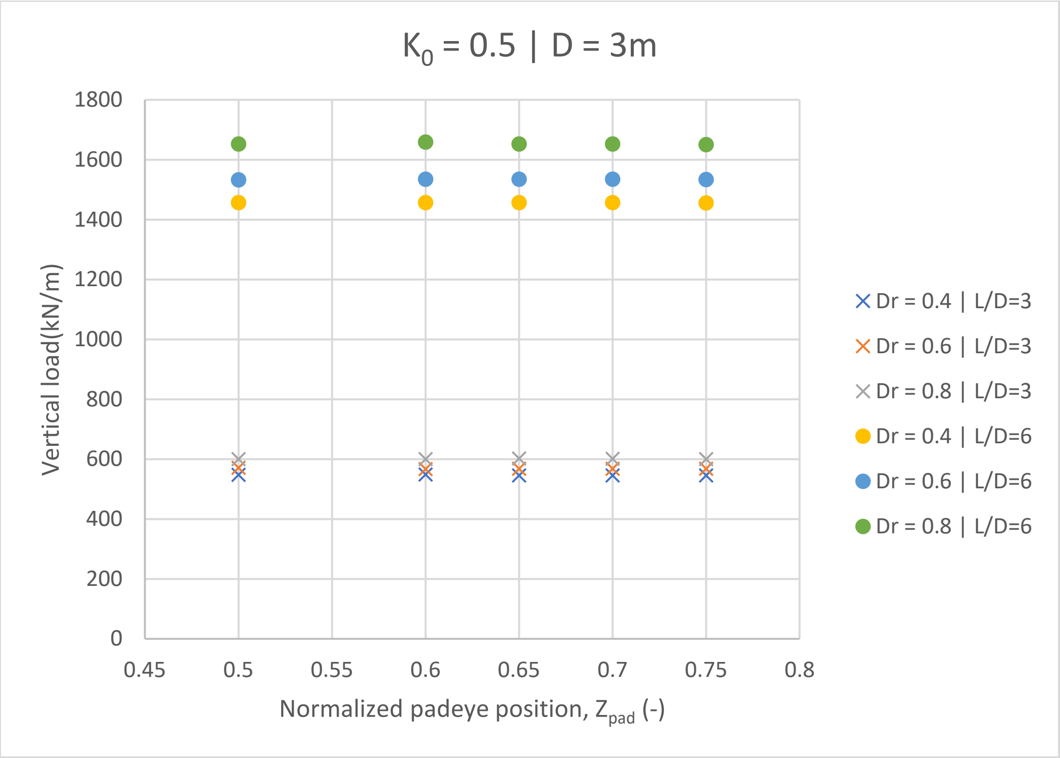

Figure 6.17 – Vertical loads applied on the skirt length with different aspect ratio for K_0 fixed

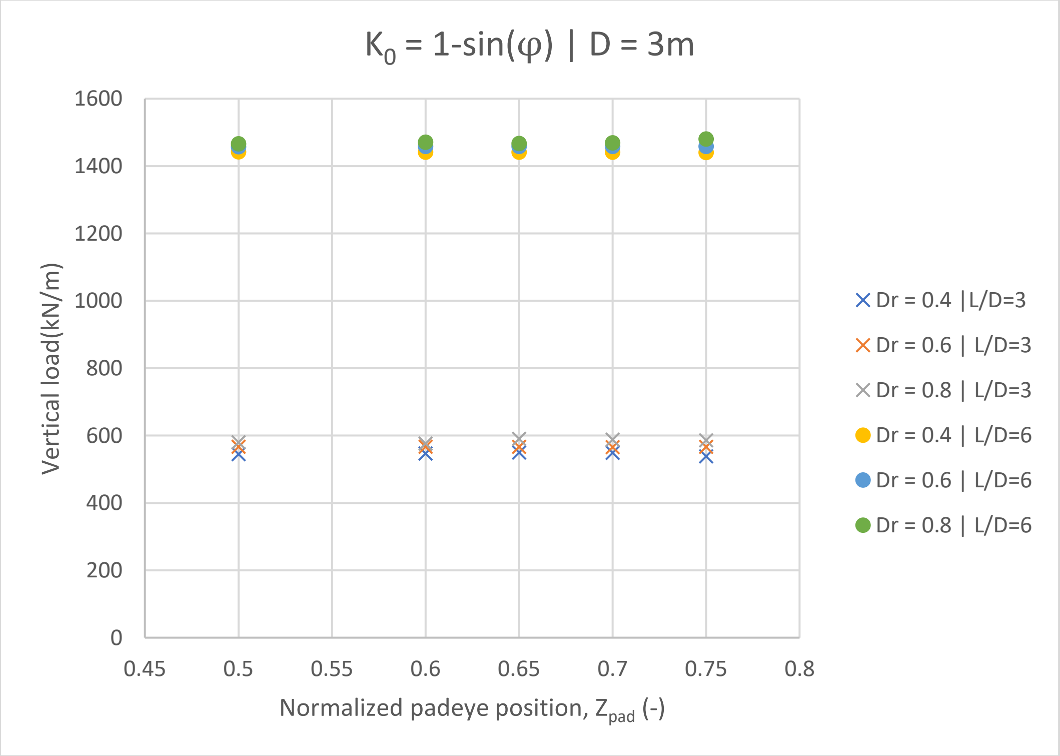

Figure 6.18 – Vertical loads applied on the skirt length with different aspect ratio for K_0 variable

Three relevant behavioral trends can be observed in the graphs, particularly regarding specific aspects of the anchor performance under analysis:

- For λ of 3 and 6, the vertical uplift capacity remains largely unaffected by changes in the applied padeye position.
- As the relative density increases, a corresponding increase in vertical capacity is observed. This trend is consistent for both fixed K_0 values and those derived from Jaky's equation. Notably, the increase in capacity exhibits smaller discrepancies when K_0 is computed using Jaky's formulation, and in the case of an aspect ratio of 6, such discrepancies become negligible. This behavior aligns with the previously observed trends in uplift capacity and can be attributed to the greater mobilization of shear resistance in cases with a higher fixed $K_0 = 0.5$, in contrast to the lower values obtained using $K_0 = 1 - \sin(\varphi)$, due to the increase in the $K\tan(\delta)$. It can be observed when comparing the results for a relative density of 40%, the ultimate uplift capacities obtained using different K_0 assumptions are remarkably similar, due to the similar final value of $K\tan(\delta)$.
- For caissons with an aspect ratio of 3, the mechanism of stress mobilization and failure appears to differ from that of caissons with an aspect ratio of 6. These shorter caissons show a reduced sensitivity to variations in K_0 under eccentric vertical loading, suggesting a different governing failure mechanism.

Analyzing two different λ and K_0 values, with the same D_r (80%) and z_{pad} (0.65), the two figures show the total deviatoric strains from the last calculation step, in order to assess the full mobilization of the soil in the final stages of the calculations.

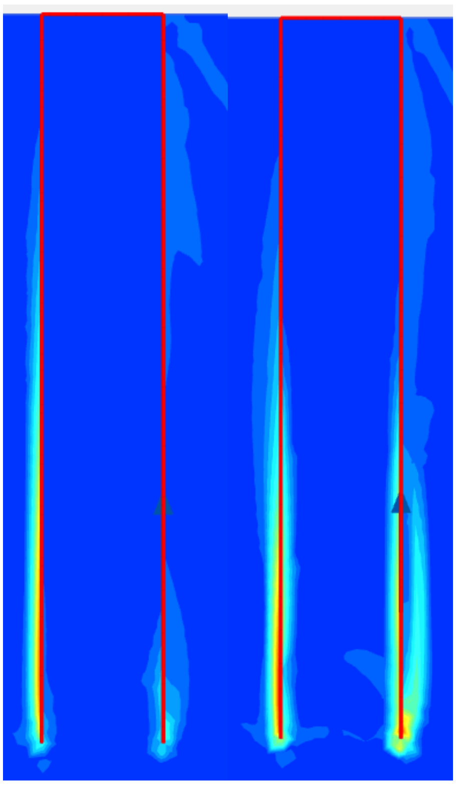

Figure 6.19 – Total deviatoric strain (γ_s) for a L/D = 6, D_r = 80%, z_{pad} = 0.65; Left side $K_0 = 1 - \sin(\varphi)$, rigth side $K_0 = 0.5$

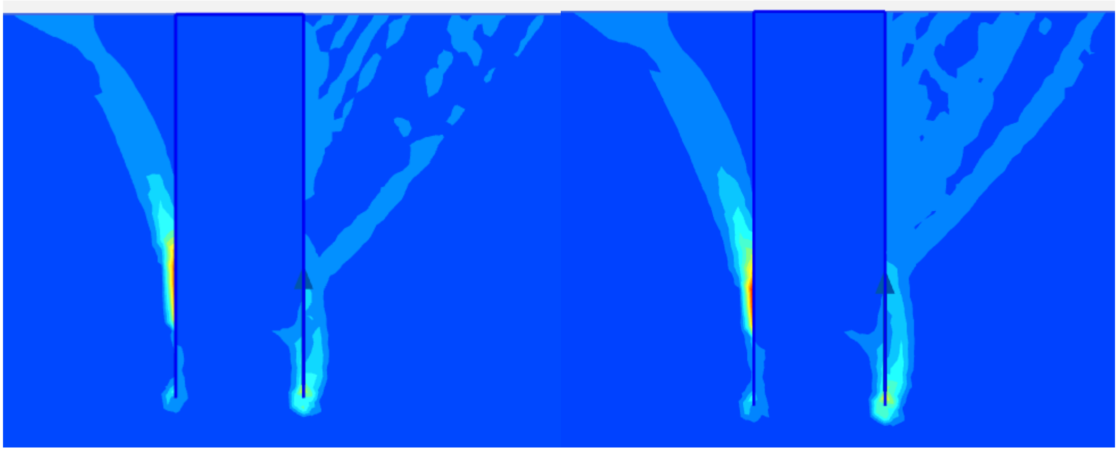

Figure 6.20 - Total deviatoric strain (γ_s) for a L/D = 3, D_r = 80%, z_{pad} = 0.65; Left side $K_0 = 1 - \sin(\varphi)$, rigth side K_0 = 0.5

Some important considerations must be highlighted at this stage:

- As observed, different anchor geometries exhibit distinct mobilization mechanisms. For anchors with a λ = 3, the mobilization is governed not only by shaft friction but also by the surrounding soil. Two soil wedges are formed along the sides of the caisson, and on the loaded side, a depression in the soil occurs. The soil on the opposite side of the applied load also contributes to the load-bearing capacity. This mobilization pattern remains consistent across different load application points, relative densities and K_0 values.
- For anchors with a λ of 6, the mobilization is predominantly concentrated along the skirts of the anchor. Unlike the λ = 3 case, the surrounding soil plays a minimal role in resistance. This behavior also helps explain the greater variation in uplift capacity when a fixed K_0 is used and the reduced variation when K_0 is computed via Jaky's equation. The mobilization pattern is consistent for all load application positions.
- A more pronounced mobilization is observed for models with K_0 = 0.5, as expected, given that load-bearing capacity is directly influenced by the value of the lateral earth pressure coefficient across different geometries and load application conditions.

Regarding the failure mechanism, the incremental deviatoric strains were analyzed in the last calculation steps in order to understand the soil mobilization prior to its plastification, thereby providing a better understanding of how shear strain mobilization in the soil develop, which constitute the failure mechanism, using the same values of D_r (80%) and z_{pad} (0.65) with different λ and K_0 values.

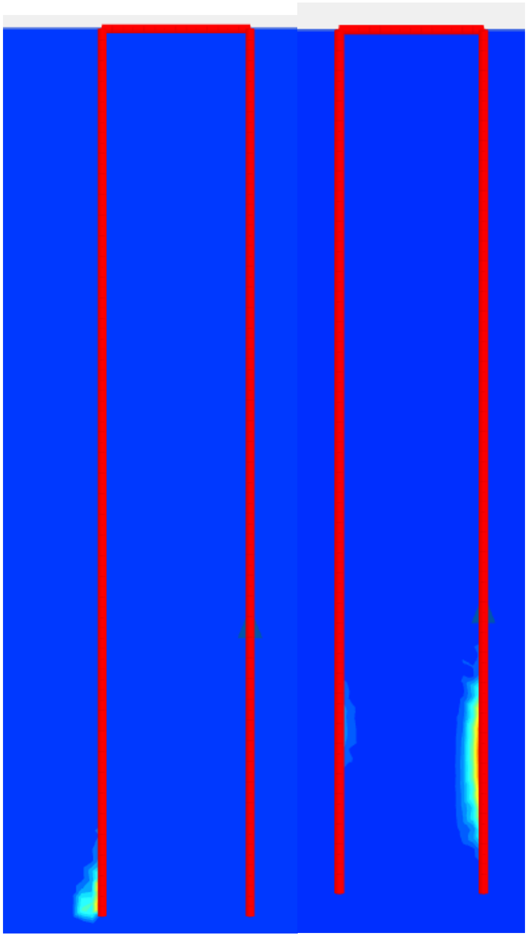

Figure 6.21 – Incremental deviatoric strain ($\Delta\gamma_s$) for a L/D = 6, D_r = 80%, z_{pad} = 0.65; Left side $K_0 = 1 - \sin(\varphi)$, rigth side K_0 = 0.5

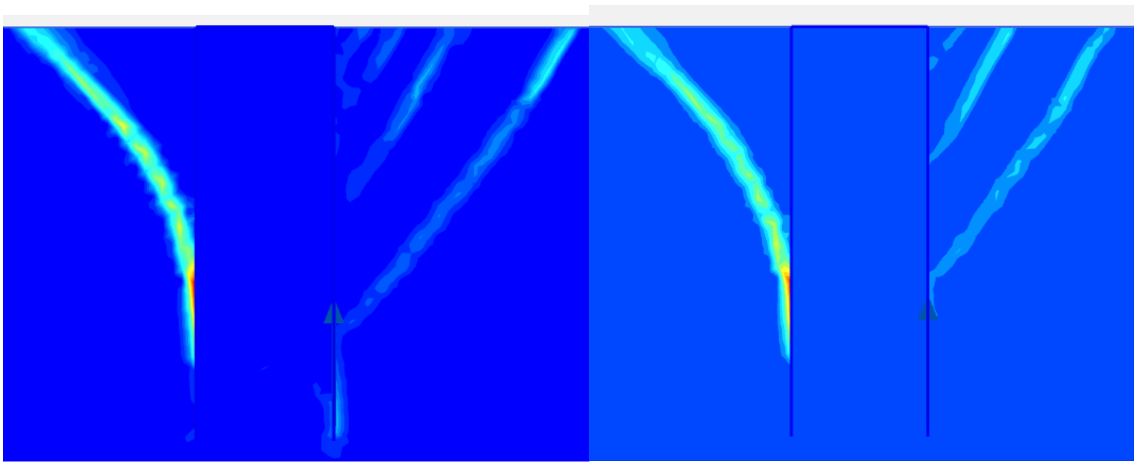

Figure 6.22 - Incremental deviatoric strain ($\Delta\gamma_s$) for a L/D = 3, D_r = 80%, z_{pad} = 0.65; Left side $K_0 = 1 - \sin(\varphi)$, rigth side K_0 = 0.5

From the strain contours at failure, the following observations can be made: For anchors with λ = 3, failure occurs through significant mobilization of the surrounding soil, consistent with the previously described wedge mechanism. In contrast, for anchors with $\lambda = 6$, failure is primarily concentrated along the skirts, indicating a distinct failure mode. These patterns are consistently observed across all relative densities and load positions analyzed.

6.4.3. Horizontal forces

There exists a well-established range for the normalized padeye position, z_{pad}, between 0.6 and 0.7, which is commonly recognized as optimal for the application of horizontal loads. In practical applications, the padeye is typically positioned at $z_{pad} = 0.65$. To investigate this behavior in greater detail, a series of numerical simulations was conducted using a caisson diameter of 3 m and λ of 3 and 6. This choice was based on the understanding that caisson diameter does not significantly influence the failure mechanism under lateral loading conditions. Simulations were carried out under consistent relative density conditions.

The analysis considered z_{pad} values of 0.5 (to capture behavior prior to the optimal range), 0.6, 0.65, and 0.7 (within the optimal range), and 0.75 (to assess post-optimal behavior). The maximum horizontal load capacity is typically observed when the caisson rotation is nearly zero. However, determining the precise z_{pad} that achieves this condition is challenging due to numerical instabilities encountered in PLAXIS 2D as the load application point approaches this critical region. Consequently, the midpoint of the established optimal range ($z_{pad} = 0.65$) was adopted for further analysis.

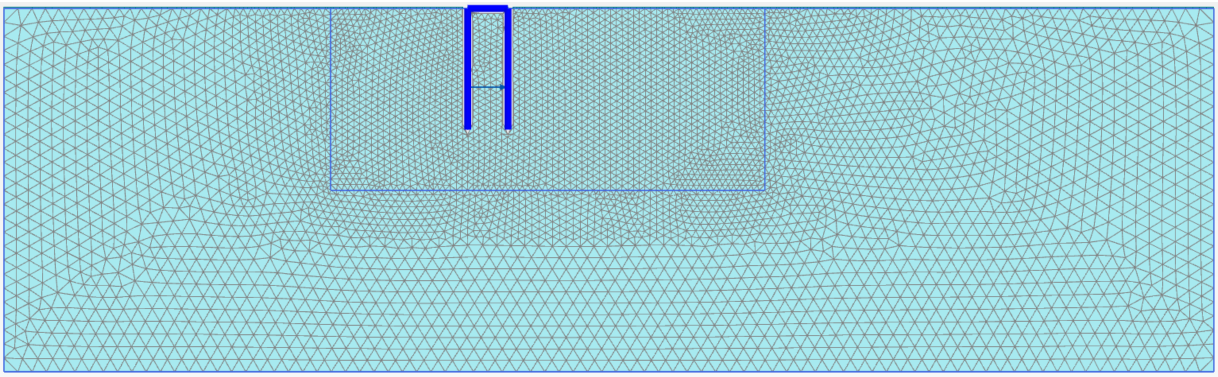

Figure 6.23 – Horizontal force applied to the anchor at $z_{pad} = 0.65$

To improve numerical accuracy, mesh refinement was applied. For the $\lambda = 3$ and $\lambda = 6$ configuration, the mesh was refined to a level equivalent to a “fine” mesh setting, the element numbers increased while the soil domain increased.

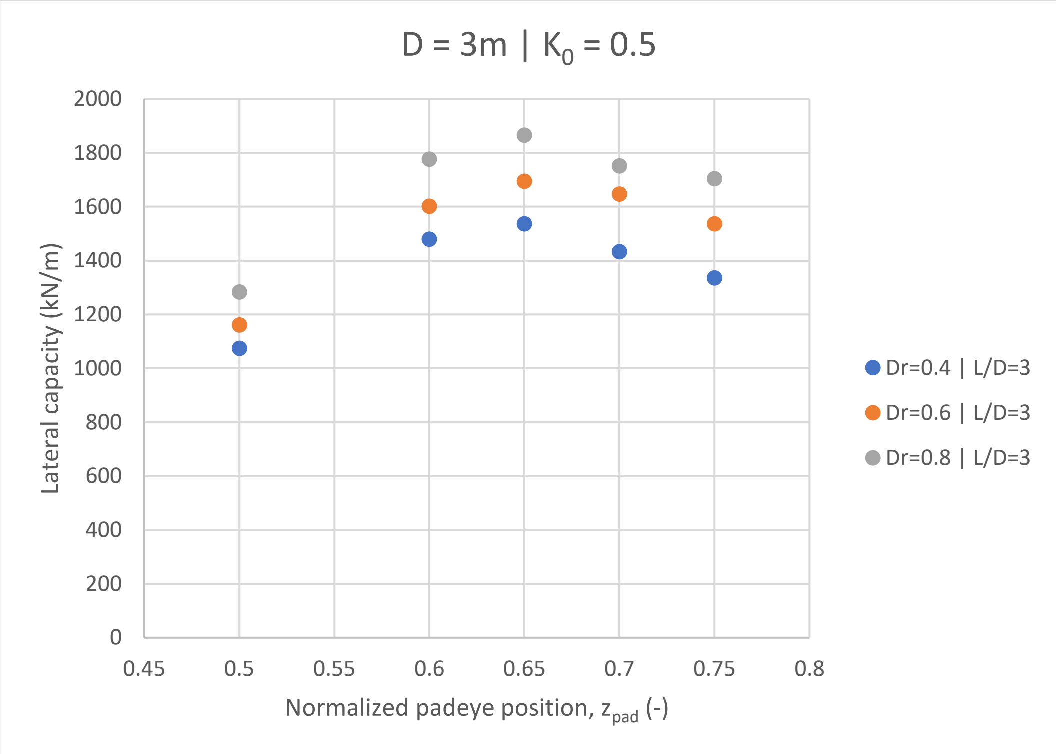

Figure 6.24 - Lateral capacity for different padeye positions using a fix K_0 and λ of 3

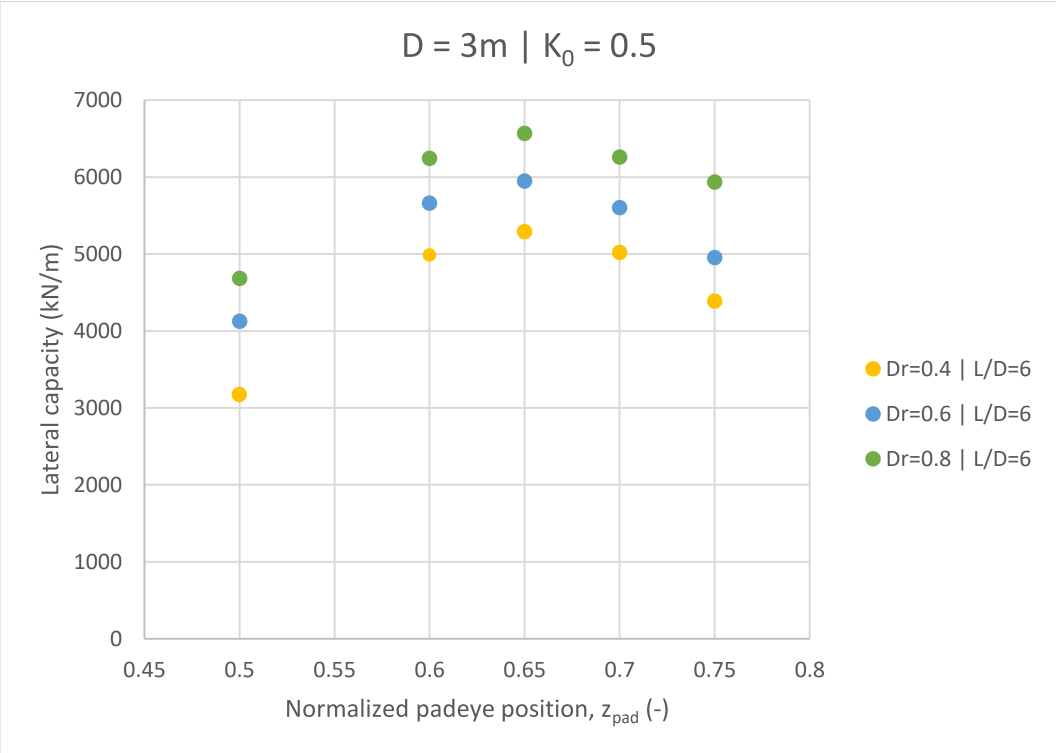

Figure 6.25 - Lateral capacity for different padeye positions using a fix K_0 and λ of 6

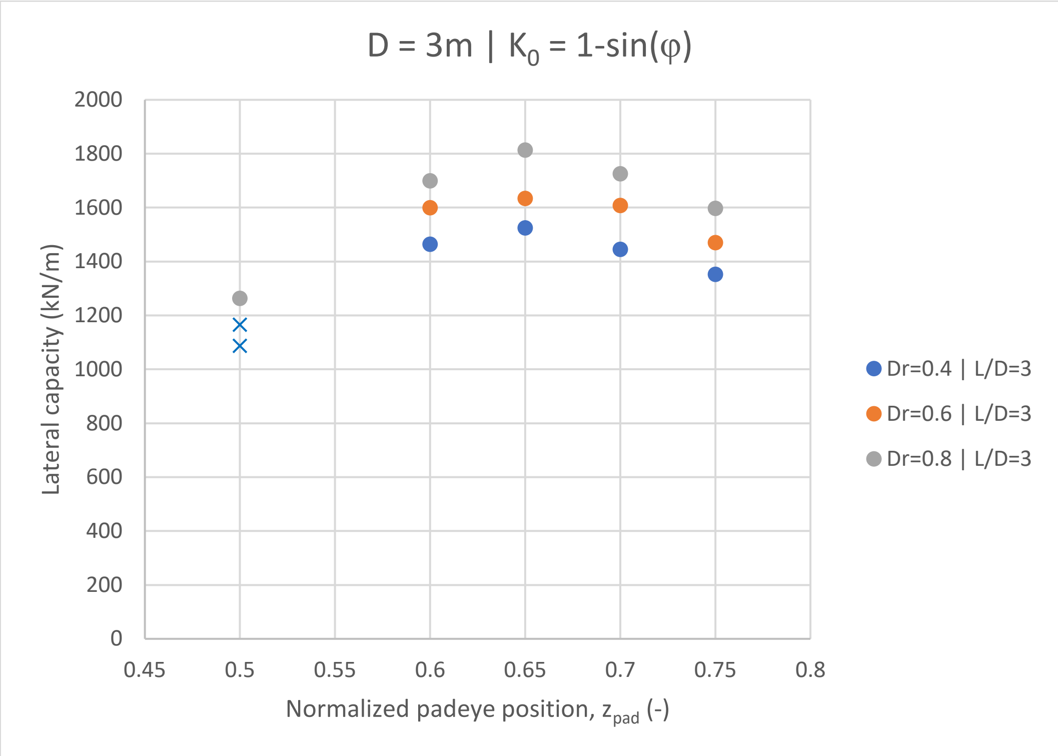

Figure 6.26 - Lateral capacity for different padeye positions using a variable K_0 and λ of 3

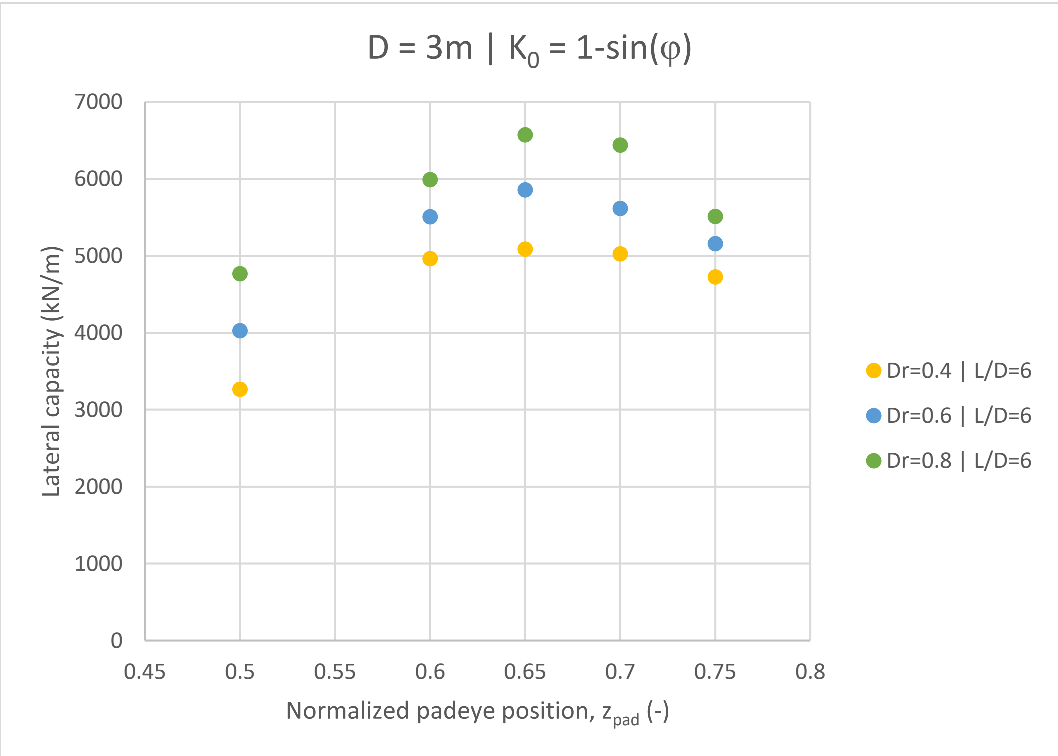

Figure 6.27 – Lateral capacity for different padeye positions using a variable K_0 and λ of 6

For both cases with z_{pad} = 0.5 in Figure 6.26 showed instability in the soil mobilization patterns, preventing the results from accurately capturing the real behavior of suction anchors.

Based on these figures, several conclusions can be drawn:

- For the cases analyzed, the optimal loading position across all soil conditions and anchor geometries is at approximately 65% of the embedment depth. This is attributed to greater soil mobilization and reduced rotation of the caisson when the load is applied at this depth.
- Lateral capacity increases with higher relative density, regardless of whether a fixed or variable K_0 is used. This reinforces the direct correlation between the soil's friction angle and the ultimate capacity of the anchor under horizontal loading. In this context, the anchor behavior resembles that of piles, being primarily governed by the passive earth pressure coefficient K_p.
- When comparing results with the same relative density but different K_0 assumptions, the fixed K_0 = 0.5 scenario shows slightly higher capacities. This can be explained by the unrestricted movement of the anchor, which, even under horizontal loading, undergoes slight vertical displacements, thereby contributing to the overall resistance.
- Previous studies have suggested that increasing the λ leads to a shift in the optimal padeye position. However, such a trend was not observed in the present results. It is important to note that those studies considered λ values between 0.5 and 2 and were conducted under different conditions. In contrast, the present work employs a different constitutive model and a plane strain formulation, which represents a uniform, linear geometry. In 3D models, the cylindrical shape of the caisson may significantly influence soil mobilization under lateral loads.
- A substantial increase in lateral capacity is observed between z_{pad} = 0.5 and z_{pad} = 0.6, suggesting a distinct soil mobilization mechanism. Beyond z_{pad} = 0.6, the variation in capacity becomes less significant compared to the difference observed between 0.5 and 0.6.

The failure mechanisms observed in the various simulations can be grouped into three distinct patterns. It is known that when the load is applied above the optimal z_{pad}, the caisson rotates clockwise. When applied at the optimal, the rotation is negligible or absent, and when applied below the optimal depth, the caisson rotates counterclockwise. These three failure mechanisms are illustrated below for λ = 3, along with the corresponding soil mobilization patterns. For the better understanding, the anchor was selected in PLAXIS 2D Output and marked as red, with any correlation with the incremental deviatoric strain.

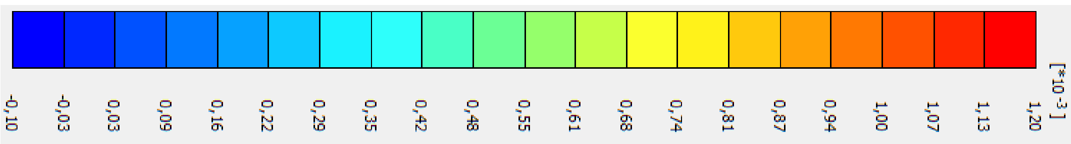

Figure 6.28 – Legend used for all the analisys of the incremental deviatoric strains for lateral capacity

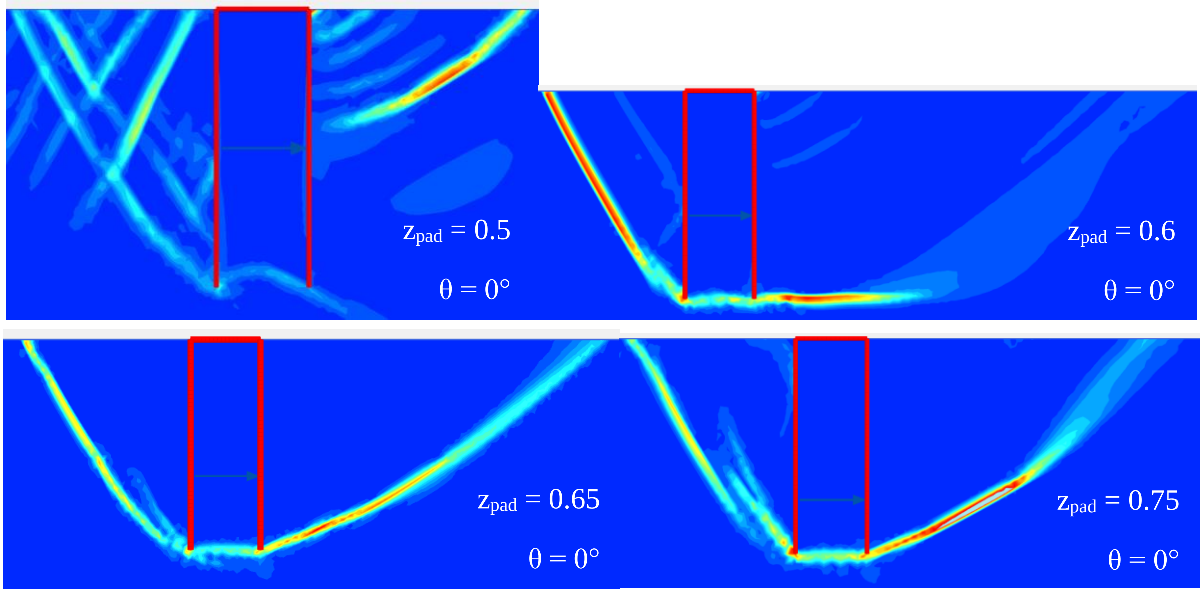

Figure 6.29 – Incremental deviatoric strain at the last step for a z_{pad} = 0.5, 0.6, 0.65, 0.75(top left to bottom right) for the same soil; K_0 = 0.5 , D_r = 0.6

Based on the observed soil failure mechanisms and mobilization, several previously presented points can be explained:

- For loads applied at z_{pad} = 0.5, a wedge of soil is mobilized both in front of and behind the anchor. This failure mechanism aligns with findings from previous studies, Christian Jensen et al. (2023). The majority of the resistance is clearly provided by the front soil wedge, which is directly influenced by the applied force and resists it through the mobilization of passive earth pressures.
- At z_{pad} = 0.6, the soil mobilization mechanism exhibits transitional characteristics. This position shows a combination of the mobilization patterns observed at z_{pad} = 0.5 and a new pattern involving mobilization near the base of the anchor. There is a clear tendency for the mobilization zone to extend upward toward the surface, as more distinctly seen in the case of z_{pad} = 0.65.
- Loads applied at z_{pad} = 0.65 demonstrate a failure mechanism consistent with the global failure mode typically observed in shallow foundations. In this scenario, the mobilized zone reaches its maximum extent, indicating efficient engagement of the surrounding soil mass.
- At z_{pad} = 0.75, a reduction in the extent of the mobilized zone is observed, particularly in the frontal region of the anchor. This diminished mobilization explains the lower load capacities recorded at this loading position.

By analyzing the different soil responses, particularly at z_{pad} = 0.65, the position associated with the highest load capacity, it is evident that increasing the relative density leads to an enhancement in the anchor's ultimate capacity. This behavior can be further illustrated in the Figure 6.30:

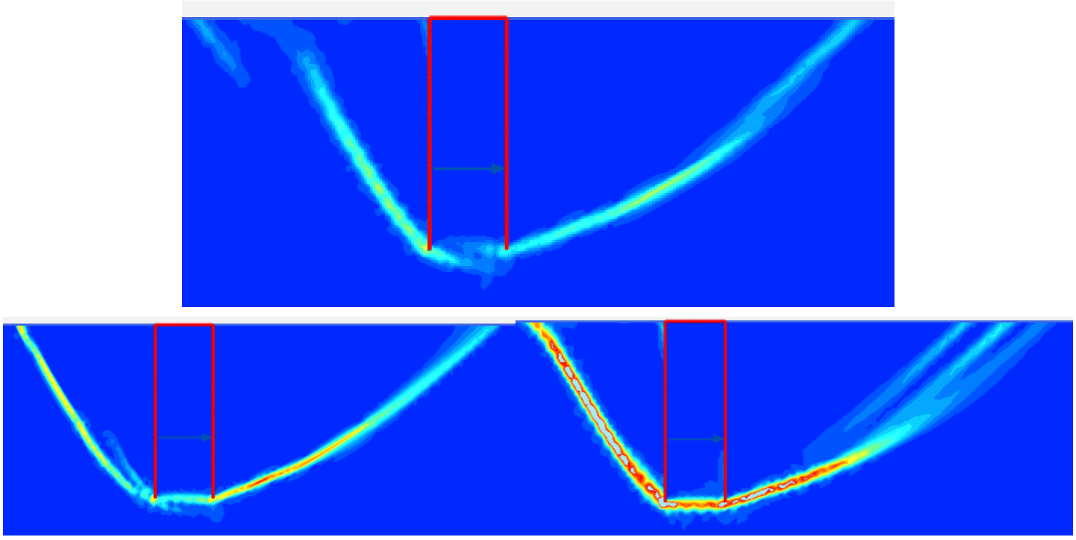

Figure 6.30 – Incremental deviatoric strains for different D_r (0.4, top, 0.6, left, 0.8, rigth) for a z_{pad} = 0.65, K_0 = 0.5

A clear distinction in soil mobilization can be observed for different values of relative density. For lower D_r values, the extent of mobilization is significantly reduced. As D_r increases, a progressive enhancement in soil mobilization becomes evident, explaining the increased values illustrated in Figures 6.23 to 6.26.

By performing a simple earth pressure calculation following Rankine's Theory, for the z_{pad} equal to 0.65, where rotation is minimal, the earth pressure values obtained for D_r = 0.4, 0.6, and 0.8 were 1138 kN/m, 1337 kN/m, and 1669 kN/m, respectively, using the equation $I = 0.5*(Kp – Ka)*\gamma'*L^2$. When compared with the numerically obtained values of 1524 kN/m, 1634 kN/m, and 1813 kN/m for D_r = 0.4, 0.6, and 0.8, respectively, it can be observed that there is an acceptable relation between the values simply calculated using Rankine's formulation and those obtained from the numerical analyses.

A ratio between the previously mentioned values was calculated for D_r = 0.4, 0.6, and 0.8, resulting in 1.34, 1.22, and 1.11, respectively, indicating a direct convergence of the values with the increase of D_r.

An analysis of the anchor behavior with an aspect ratio of $\lambda = 6$ reveals mobilization patterns similar to those observed for anchors with $\lambda = 3$. However, as expected with the increase in geometric slenderness, a more pronounced soil mobilization is observed, as illustrated below:

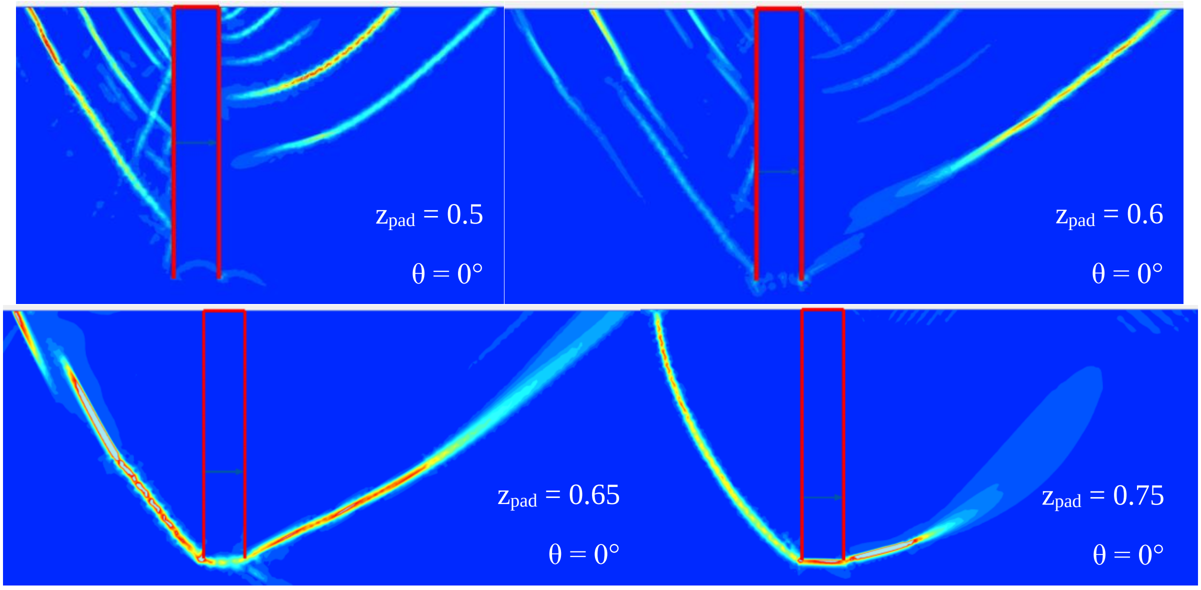

Figure 6.31 - Incremental deviatoric strain at the last step for a z_{pad} = 0.5, 0.6, 0.65, 0.75(top left to bottom right) for the same soil; K_0 = 0.5 , D_r = 0.6

Observations can be drawn from the figure:

- The mobilized soil wedges at z_{pad} = 0.5 exhibit greater depth when compared to those associated with the smaller geometry. In the case of λ = 3, the wedges tend to develop above the applied load, whereas for λ = 6, mobilization occurs below the load application point.
- For z_{pad} = 0.6, the mobilized wedges near the surface become more pronounced, and the formation of a continuous mobilization path, as seen in z_{pad} = 0.65, begins to emerge.
- When the load is applied at z_{pad} = 0.65, the failure mechanism remains consistent with the global failure mode typically observed in shallow foundations. Proceeding with a simple earth pressure calculation, comparing the numerical values with those obtained using the equation $I = 0.5*(Kp – Ka)*\gamma'*L^2$, the results are 5948 kN/m and 5346 kN/m, respectively, a significant difference between them is evident.
- At z_{pad} = 0.75, a circular wedge forms on the side opposite to the applied load, indicating a more pronounced rotational behavior of the anchor.

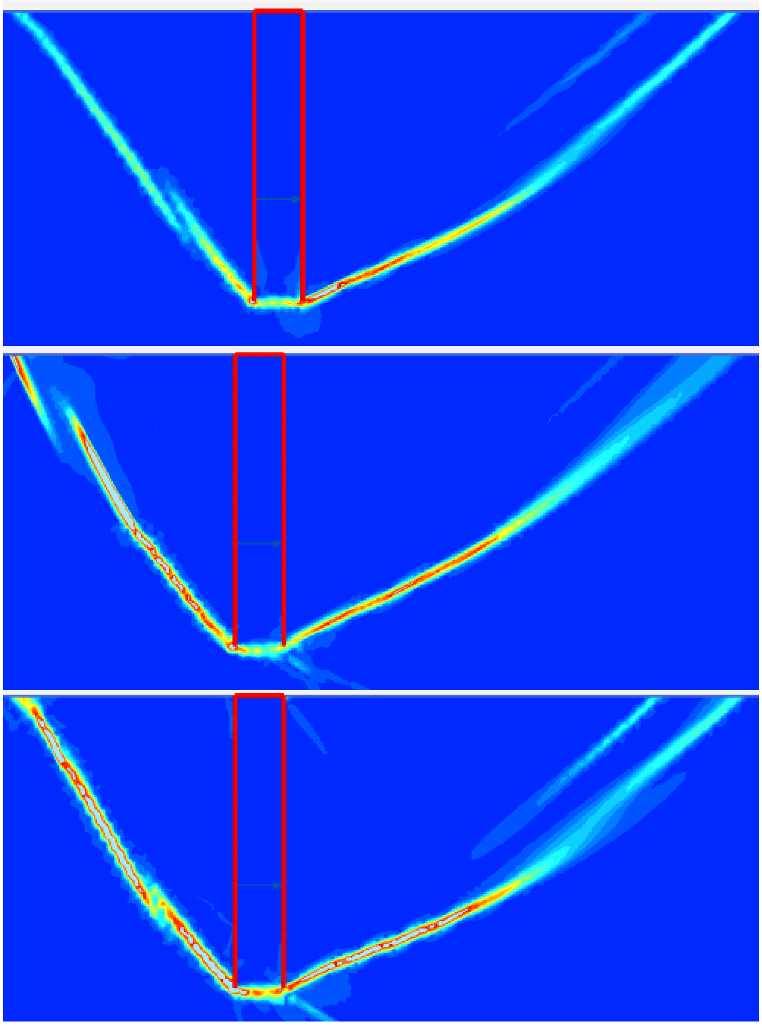

Figure 6.32 – Incremental strains at the last step for a z_{pad} = 0.65, K_0 = 0.5, D_r = 0.4, 0.6, 0.8(Top to bottom)

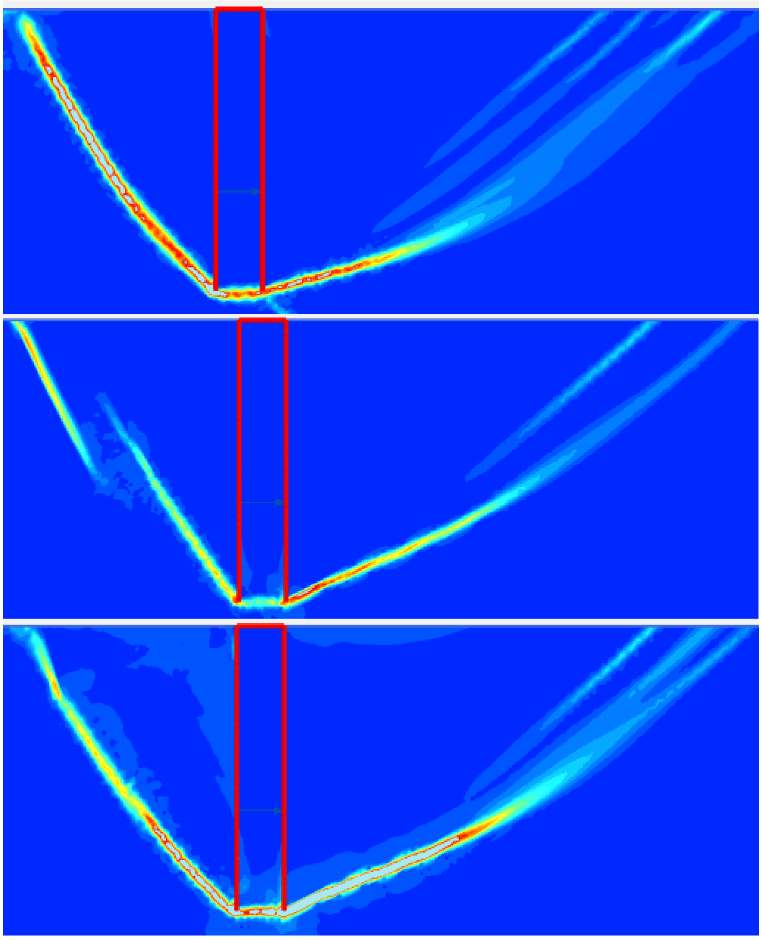

Figure 6.33 - Incremental strains at the last step for a z_{pad} = 0.65, K_0 = 1-sin(φ), D_r = 0.4, 0.6, 0.8(Top to bottom)

Regarding the differences in K_0 values, the soil mobilization patterns observed under fixed and variable K_0 conditions exhibit only slight variations. For a relative density of D_r = 0.4, the mobilization mechanisms are similar; however, the cases with K_0 = 0.5 consistently show higher capacity values. This trend is evident for suction anchors with both aspect ratios and across various z_{pad} positions.

6.4.4. Inclined forces

An inclined loading condition was analyzed at an angle of 30 degrees relative to the horizontal. This analysis was compared with the approach presented in "Offshore Geotechnical Engineering", which reports that, for inclined loads acting at 30 degrees in cohesive soils, the optimal z_{pad} lies between 0.60 and 0.64 for caissons with λ of 3 and 5.

In the analyses conducted with a load inclined at 30 degrees, different z_{pad} were evaluated following the same pattern as that used for horizontal loading. However, additional positions were incorporated in order to ensure that a peak in the pullout capacity response could be captured, thereby identifying the region corresponding to the optimal z_{pad}. Specifically, two new values, 0.8 and 0.9, were introduced into the analysis. The caisson diameter was maintained at 3 meters, and λ of 3 and 6 were adopted, representing commercially relevant geometries.

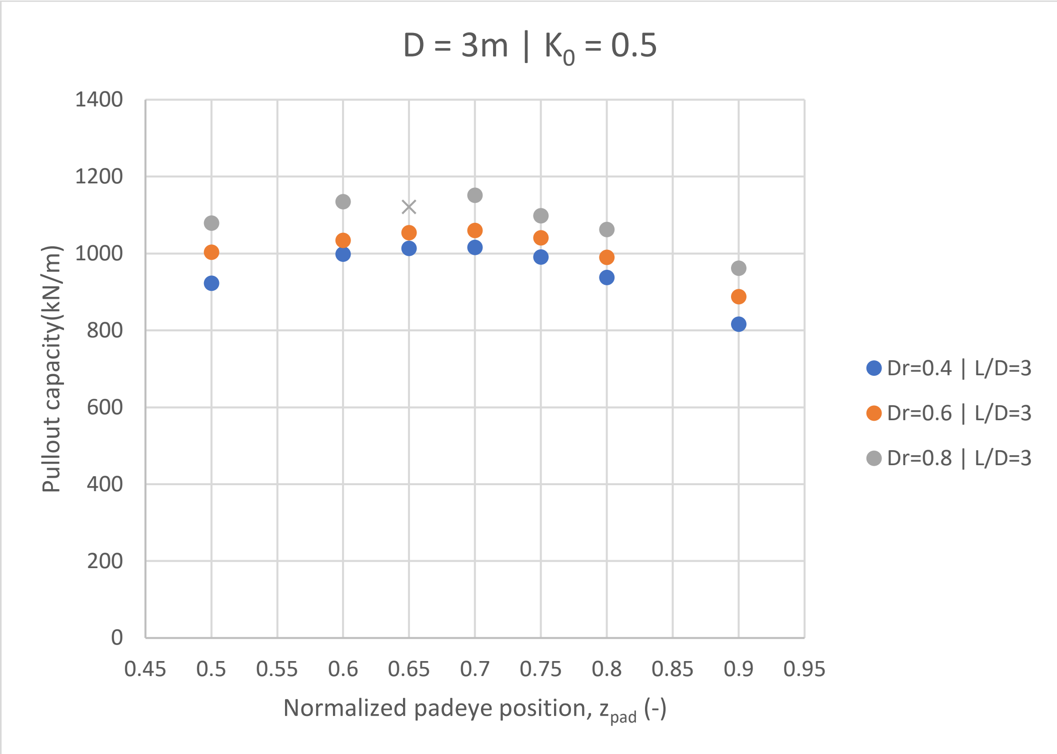

Figure 6.34 – Pullout capacity for different padeye positions using a fix K_0 and λ of 3

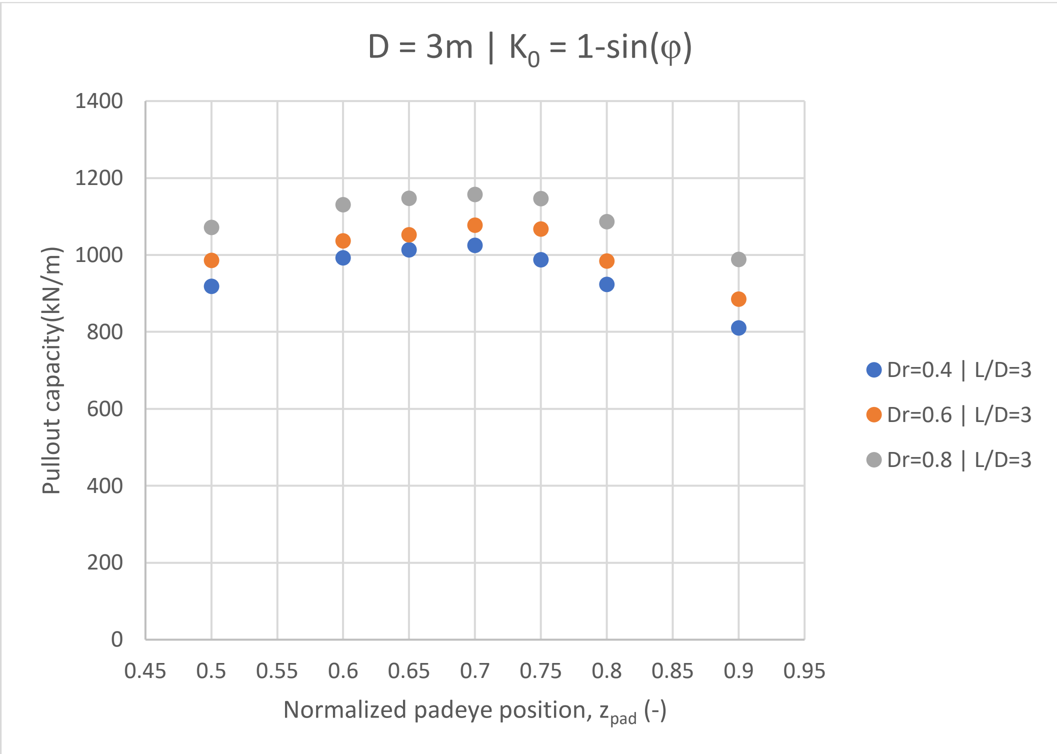

Figure 6.35 – Pullout capacity for different padeye positions using a variable K_0 and λ of 3

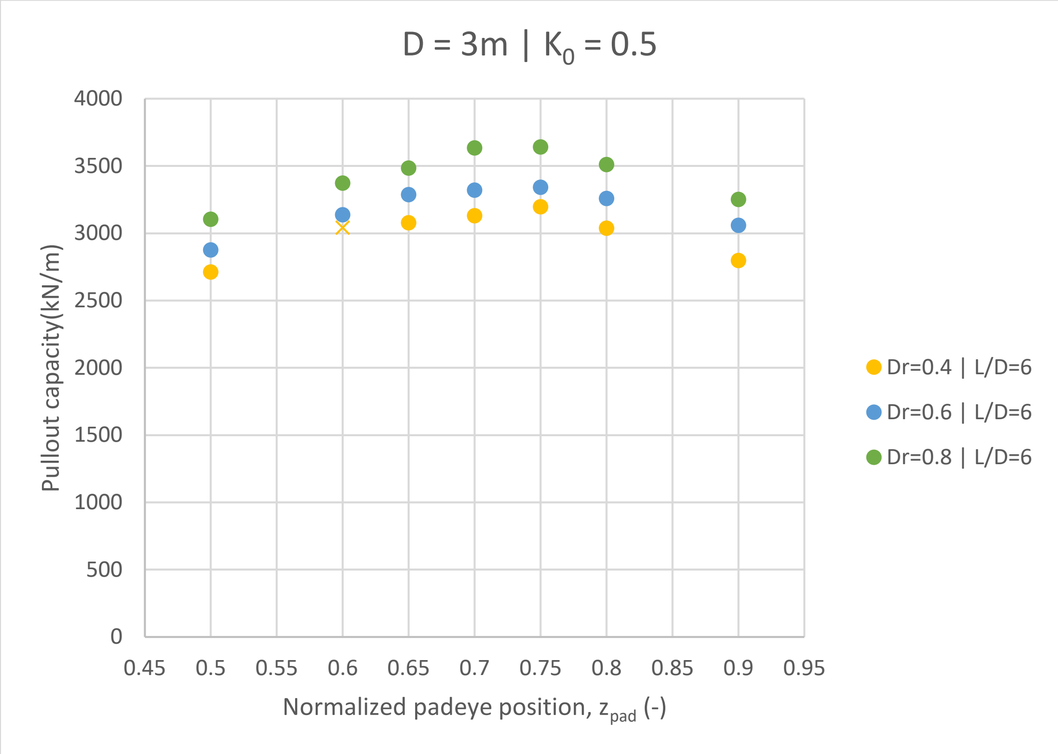

Figure 6.36 – Pullout capacity for different padeye positions using a fix K_0 and λ of 6

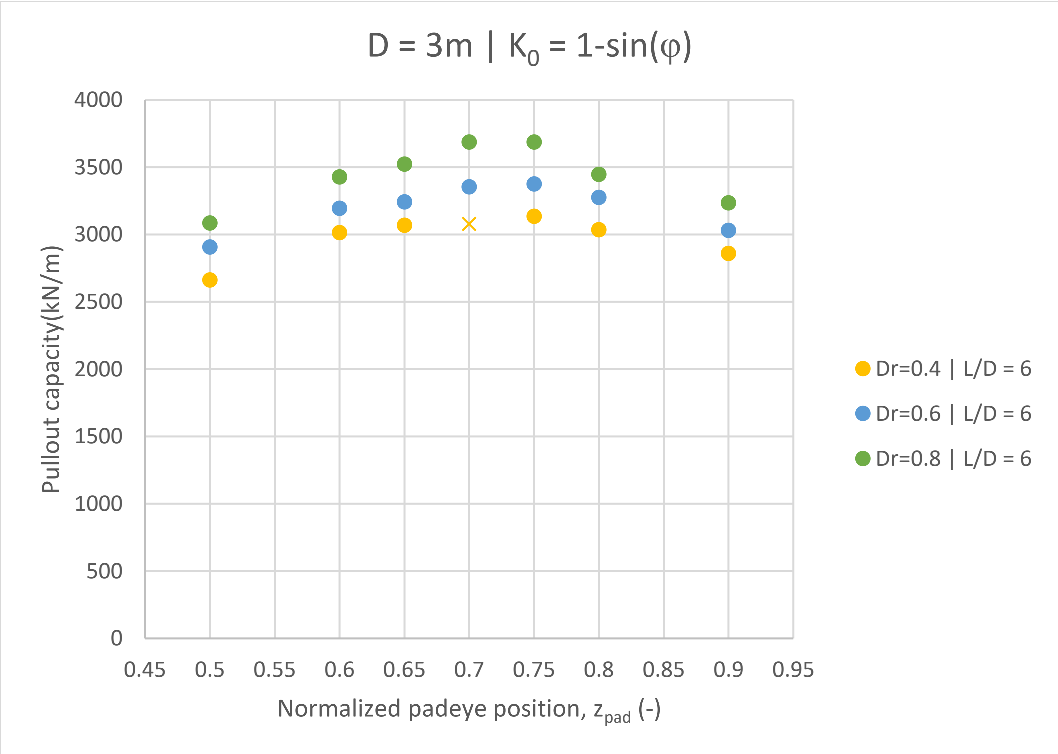

Figure 6.37 – Pullout capacity for different padeye positions using a variable K_0 and λ of 6

The pullout capacity was considered as the resultant of the horizontal and vertical components obtained from the analyses.

Several observations can be made based on the plotted results:

- For caissons with a λ of 3, the optimal z_{pad} is approximately 0.7, while for λ equal to 6, the optimal position increases to around 0.75. This indicates a relationship between the increase of z_{pad} from 0.7 to 0.75, together with the increase of λ from 3 to 6, which suggests that for a caisson with λ between 3 and 6, the optimal z_{pad} will lie between 0.7 and 0.75.
- Unlike the behavior observed under purely horizontal loading, the variation in capacity values before reaching the optimal z_{pad} is more gradual. However, beyond the optimal point, the pullout capacity drops significantly, suggesting a shift in the failure mechanism of the soil.
- Regarding the influence of the K_0, no significant differences were observed between fixed and variable values. In contrast, changes in relative density, D_r, had a substantial impact on the results. Even though the loading includes a vertical component, the increase in capacity for $K_0=1-\sin(\varphi)$ highlights the predominance of the horizontal component in governing the soil response under inclined loading at 30°.
- For caissons with $\lambda = 6$, the increase in D_r results in a much more pronounced peak in the pullout capacity at the optimal z_{pad} position compared to caissons with $\lambda = 3$. This may be attributed to the higher soil mobilization potential at the optimal padeye position when the caisson has a greater aspect ratio, allowing a substantially larger volume of soil to be engaged in resistance.

To support and further clarify some of the previously discussed observations, the incremental deviatoric strains at the final calculation step is presented, thus showing the soil shear behavior and consequently providing a better understanding of the soil mobilization and failure induced by the applied load. The following figure illustrates all the soil failure mechanisms observed for a caisson geometry with an aspect ratio of $\lambda = 3$.

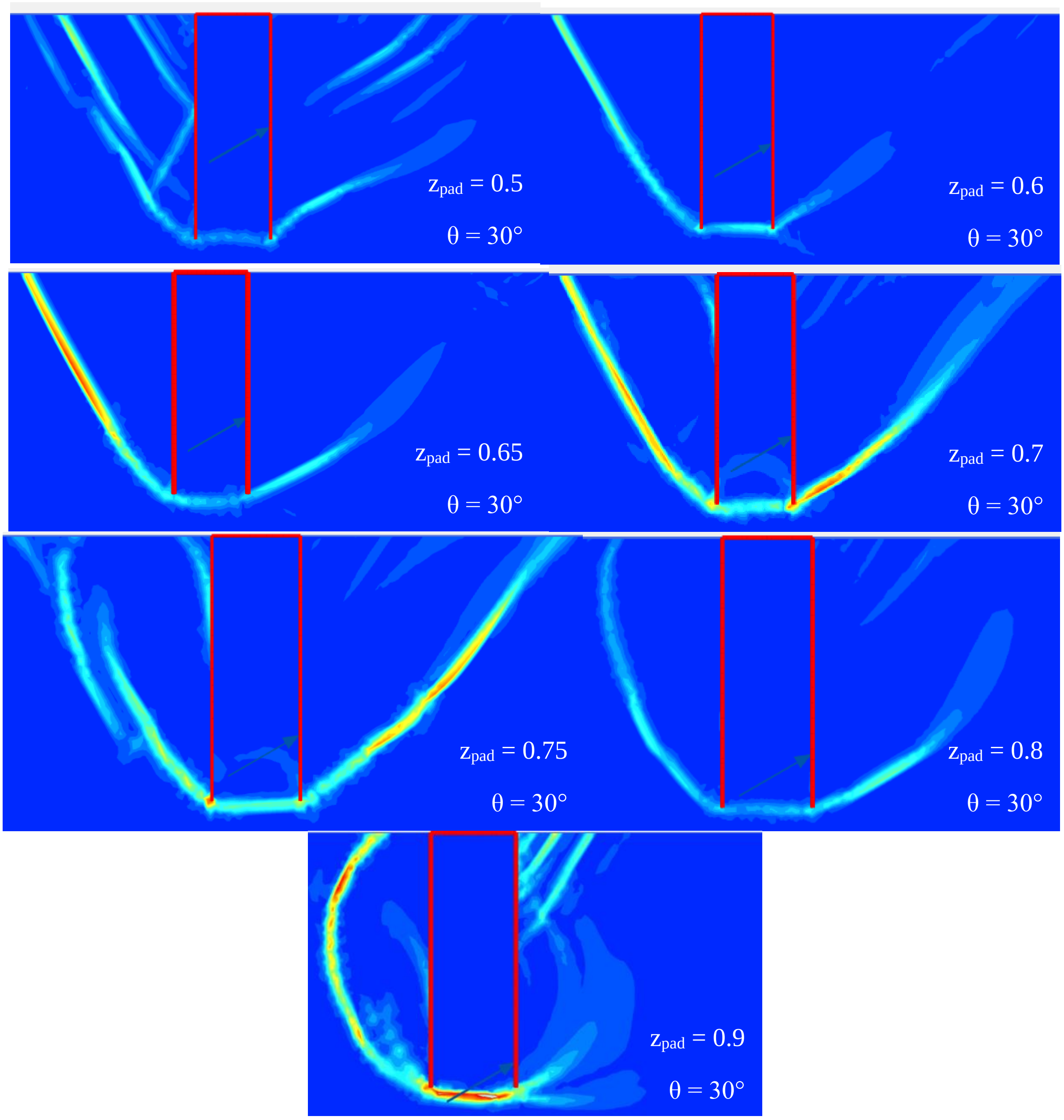

Figure 6.38 - Incremental deviatoric strain at the last step for a z_{pad} = 0.5, 0.6, 0.65, 0.7, 0.75, 0.8, 0.9 (Top left to bottom), for the same soil; $K_0 = 1 - \sin(\varphi)$, $D_r = 0.6$

Based on the analysis of the figure above, several conclusions can be drawn:

- The soil mobilization in the figure with z_{pad} equal to 0.7 is greater than in the other cases, with a much more developed mobilization line, especially at the base, demonstrating the peak in load capacity. The failure mechanism resembles that observed in shallow foundation failure modes.
- Three distinct failure mechanisms can be identified, with the change in the application depth of the load influencing the incremental deviatoric strains:

1. $z_{pad} = 0.5$: The failure mechanism here resembles that of horizontal loading, with two mobilized wedges, one at the front and one at the rear of the caisson, and slight soil mobilization at the base of the anchor. The rotation is clockwise.
2. $z_{pad} = 0.65$: The soil mobilization pattern represents a transitional mechanism between the behavior observed at $z_{pad} = 0.5$ and a global failure mechanism typically associated with shallow foundations. The rotation here and beyond is counterclockwise.
3. $z_{pad} = 0.8$: A change in both the front and rear mobilization lines is noted, with a tendency toward a circular pattern, indicating that beyond this point, the anchor undergoes greater rotation compared to the previous cases, altering the failure behavior.

- Proceeding with a simple earth pressure calculation, for soil conditions with $D_r = 0.6$ and $\varphi = 34.26°$, the corresponding values are Ka = 0.28 and Kp = 3.58. The final value of the difference between passive and active earth pressures, using the equation $I = 0.5*(Kp - Ka)*\gamma'*L^2$, results in 1337 kN/m, which is a higher value when compared with the applied load values at $z_{pad} = 0.65$ and 0.7, where greater soil mobilization occurs, with total values of 1052 kN/m and 1077 kN/m, respectively.

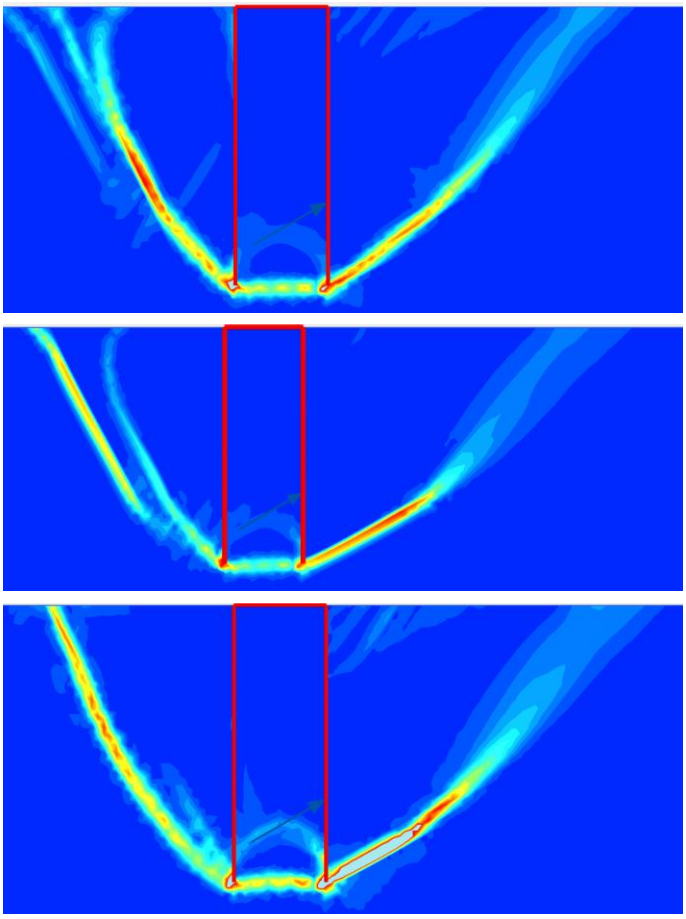

Figure 6.39 – Incremental deviatoric strains in the last step for a $D_r = 0.4$, 0.6, 0.8(Top to bottom), for the same soil; $K_0 = 0.5$, $z_{pad} = 0.7$

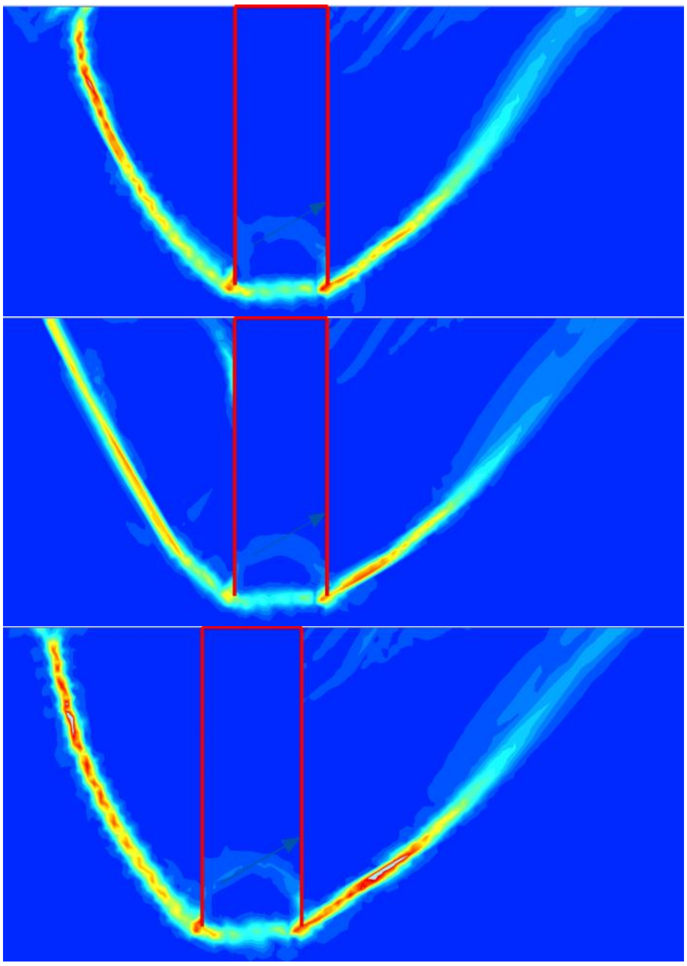

Figure 6.40 – Incremental deviatoric strains in the last step for a D_r = 0.4, 0.6, 0.8(Top to bottom), for the same soil; $K_0 = 1 – \sin(\varphi)$, z_{pad} = 0.7

As observed in the figure above, the soil behavior exhibits a straight mobilization line on the front side of the anchor in all cases. With increasing values of D_r, it is evident that soil mobilization becomes progressively more extensive. Among the three scenarios analyzed, the case with D_r = 0.8 demonstrates the greatest mobilized soil volume, highlighting the influence of relative density on the extent of soil activation, following the same behavior of the global shallow foundation failure, as can be seen in Figure 6.5, with the values of ψ and ψ' accompanying the variation of the soil friction angle.

A comparison between the two K_0 approaches reveals an increased soil mobilization when K_0 = 0.5 is adopted. This trend is maintained across all cases, where an increase in D_r consistently leads to greater soil mobilization and more developed failure mechanisms. Despite the difference in lateral earth pressure coefficient, the qualitative behavior of soil failure remains consistent, with enhanced mobilization observed for higher K_0 values.

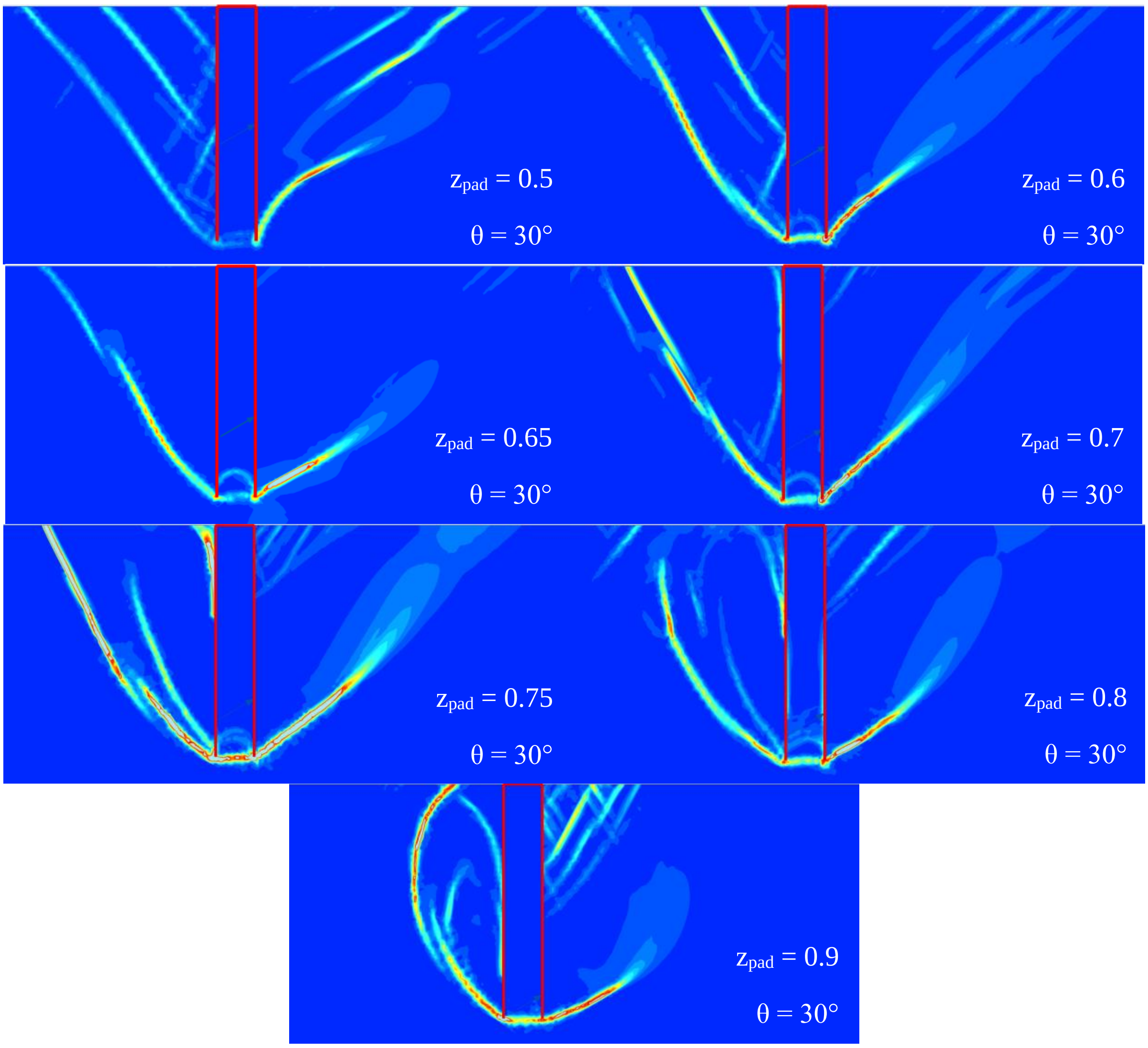

Figure 6.41 - Incremental deviatoric strain at the last step for a z_{pad} = 0.5, 0.6, 0.65, 0.7, 0.75, 0.8, 0.9 (Top left to bottom), for the same soil; K_0 = 0.5, D_r = 0.8

For the cases with $\lambda = 6$, several observations can be made:

- The failure mechanisms generally follow the same pattern as those observed for smaller geometries. However, a distinct difference is noted for $\lambda = 6$, where the highest degree of soil mobilization occurs at $z_{pad} = 0.75$, rather than at $z_{pad} = 0.7$, as previously identified for $\lambda = 3$.
- At $z_{pad} = 0.5$, the failure mechanism appears to transition between the behavior typical of a horizontally applied load at the same z_{pad} and that of a global failure in shallow foundations. This is characterized by frontal wedges that are not fully rounded and by noticeable mobilization at the caisson base.
- The greatest extent of soil mobilization is observed for $z_{pad} = 0.75$, which also corresponds to the optimal padeye position for all relative densities in the $\lambda = 6$ configuration. The mobilization pattern extends from the caisson base up to the soil surface. As previously discussed, the mobilized soil volume for $z_{pad} = 0.7$ is larger than that for $z_{pad} = 0.8$, indicating a shift in the

failure mechanism. This shift is marked by the formation of frontal soil wedges near the surface and a curved mobilization zone at the rear, suggesting a greater degree of caisson rotation.

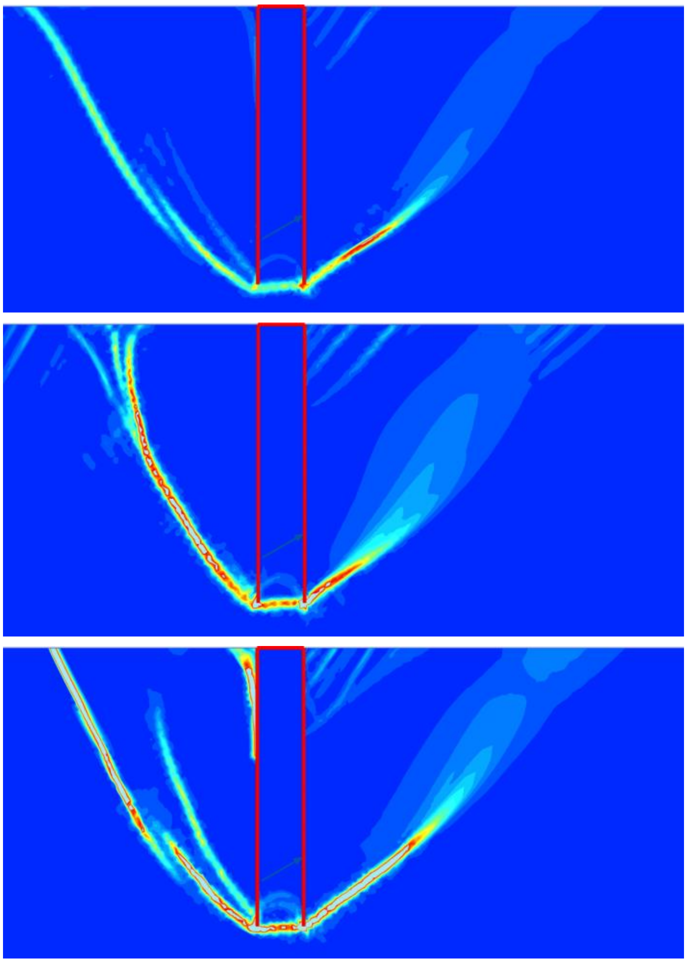

Figure 6.42 - Incremental deviatoric strain at the last step for a D_r = 0.4, 0.6, 0.8(Top to bottom), for the same soil; K_0 = 0.5, z_{pad} = 0.75

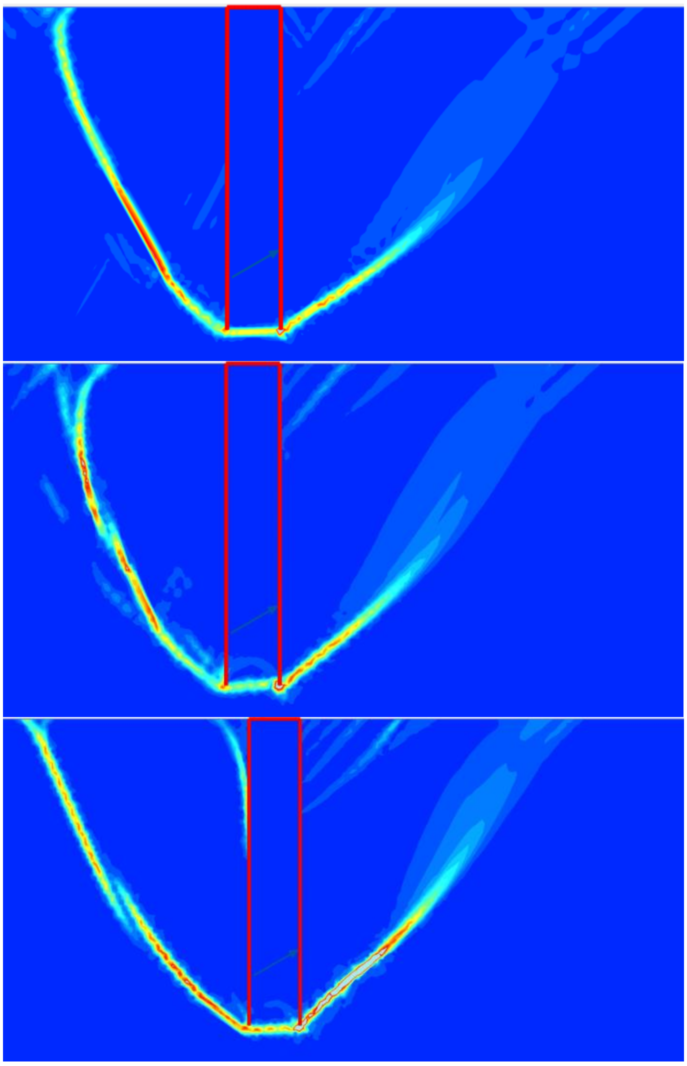

Figure 6.43 - Incremental deviatoric strain at the last step for a D_r = 0.4, 0.6, 0.8(Top to bottom), for the same soil; K_0 = 1-sin(φ), z_{pad} = 0.75

As can be observed, the trend lines of the soil failure mechanisms become more pronounced with increasing D_r, consequently φ, following the same behavior previously noted for $\lambda = 3$. For $D_r = 0.4$, the soil mobilization at the front of the suction caisson extends up to the surface. However, when compared to the cases with $D_r = 0.6$ and $D_r = 0.8$, the extent of mobilized soil increases significantly. Although the soil behavior remains consistent across different values of K_0, a greater degree of mobilization is clearly observed when $K_0 = 0.5$.

6.4.5. Failure envelope

To a deeper understanding of the behavior of suction anchors, several studies, such as those by Cheng et al. (2021) and Randolph and Gourvenec (2005), have investigated the response under varying load inclinations, ranging from 0° (horizontal) to 90° (vertical), and at different z_{pad}. These investigations produced failure envelopes that represent the combined resistance to horizontal and vertical loading, plotted along the x and y axes, respectively. Any load combination falling within this envelope is considered to be safely supported by the anchor.

This failure envelope is a function of the soil characteristics, the anchor geometry, and the position of the z_{pad}. Each of these variables influences the shape and extent of the failure envelope. For cohesive soils, an ellipsoidal failure envelope has been observed, as demonstrated in the study by Randolph and Gourvenec (2005). However, for cohesionless soils, a different failure mechanism and envelope behavior have been identified, reflecting the distinct interaction between the soil and the anchor under varying loading conditions.

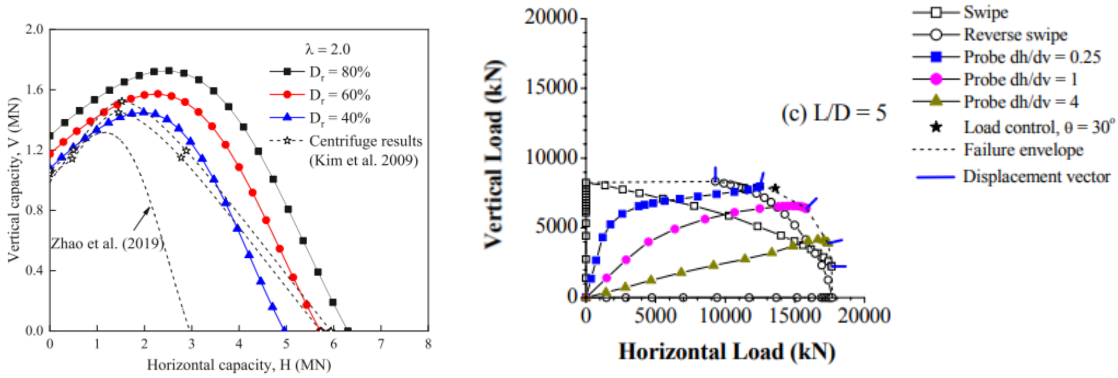

Figure 6.44 – Failure envelope for different soils

As can be observed, there is a distinct difference between the two failure envelopes:

- For the failure envelope associated with cohesionless soils, the vertical capacity increases with the horizontal capacity for load inclinations approaching 90°. In contrast, for cohesive soils, the vertical capacity initially remains constant with increasing horizontal load, but subsequently decreases.
- In both cases, the maximum capacity is observed under horizontal loading (0°) when compared to vertical loading (90°).
- Due to the differing failure mechanisms, separate formulations are used to define the failure envelopes: for cohesive soils, the failure envelope is calculated using Equation (26), while for cohesionless soils, the formulation is based on Equation (29).

To clearly understand the nature of the failure envelopes for different soil types, a distinction was made between cohesive and cohesionless soils. For cohesive soils, the failure envelope is defined by the following equation:

$$\left(\frac{H}{H_{ult}}\right)^a + \left(\frac{V}{V_{ult}}\right)^b = 1 \tag{26}$$

Where H_{ult} represent the maximum horizontal capacity of the anchor with the load applied at the padeye, and V_{ult} the maximum vertical capacity under the same condition. The exponential components are expressed as functions of the aspect ratio as follows:

$$a = 0.5 + \frac{L}{D} \tag{27}$$

$$b = 4.5 - \frac{L}{D} \tag{28}$$

For cohesionless soils, the equation describing the behavior of the failure envelope is given as follows:

$$\left(\frac{V}{V_o}\right)\left(1 - a\left(\frac{H}{H_o}\right) + b\left(\frac{H}{H_o}\right)^d\right) + \left(\frac{H}{H_o}\right)^e = 1 \tag{29}$$

Where V_o is the vertical component of the load applied at the padeye, and H_o the horizontal component. The coefficients are defined as follows: $a = 0.5 + 1.47 \cdot z_{pad}$, $b = -1.03 + 2.85 \cdot z_{pad}$, both as functions of z_{pad}; d as a function of the D_r and λ, defined by $d = \lambda - 0.07 \cdot D_r$; and e as a function solely of the aspect ratio, with $e = 1.14 + 0.14 \cdot \lambda$.

It is important to highlight that, in Equation (29), the values of λ analyzed were limited to the range between 0.5 and 2, which fall outside the typical commercial geometries and is therefore not consistent with the behavior and results presented here by the calculations.

This study initially aimed to investigate the behavior of the failure envelopes, however, it was not possible to perform a proper calibration as was done in the previous chapters. Nevertheless, some important behavioral trends observed during the construction of the envelopes are discussed.

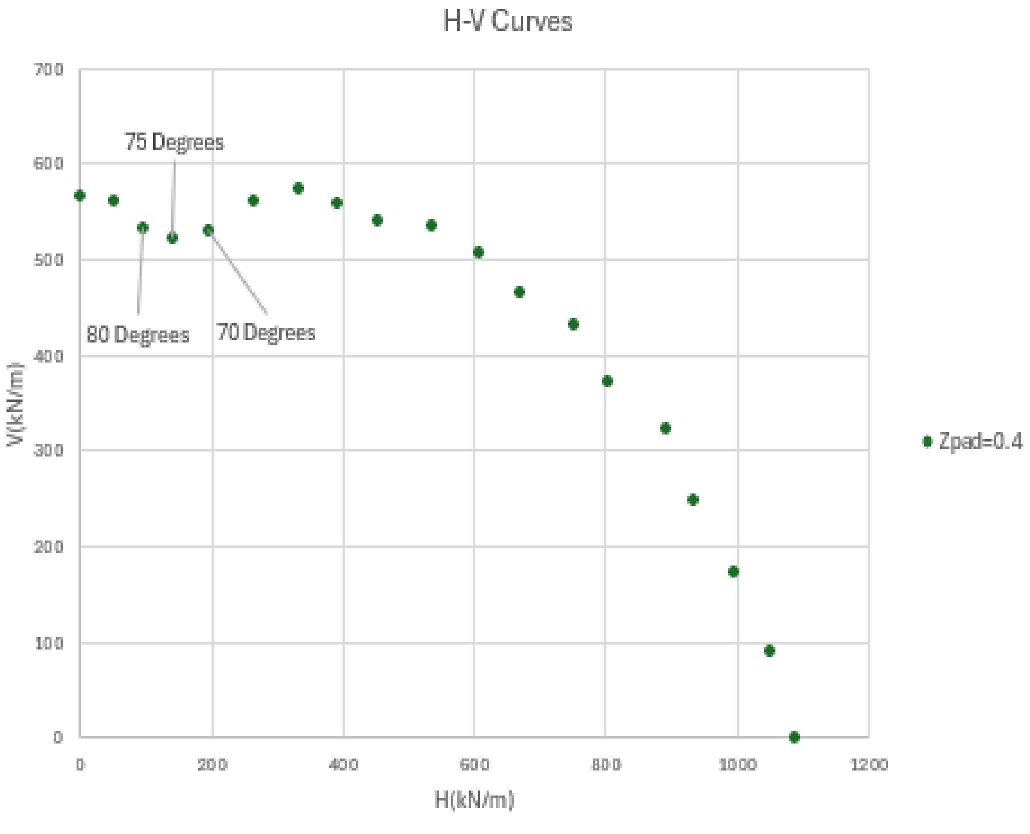

Figure 6.45 – Failure envelope for a L/D = 3, $K_0 = 1 - \sin(\varphi)$, $D_r = 0.6$, $z_{pad} = 0.4$

As it can be seen in Figure 6.45 the applied force values between 80° and 70°, there is an abrupt drop in the vertical values for z_{pad}=0.4 and lower. However, as the z_{pad} values increase, there is a tendency for the vertical values to rise at these inclinations. This behavior can be explained by the rotational response of the anchor, whereby, when subjected to a load with an inclination of 75 degrees at z_{pad}=0.4, the rotation is close to zero, with very low horizontal displacements and high vertical displacements, resulting solely in the uplift of the anchor, as illustrated in the following Figure 6.46.

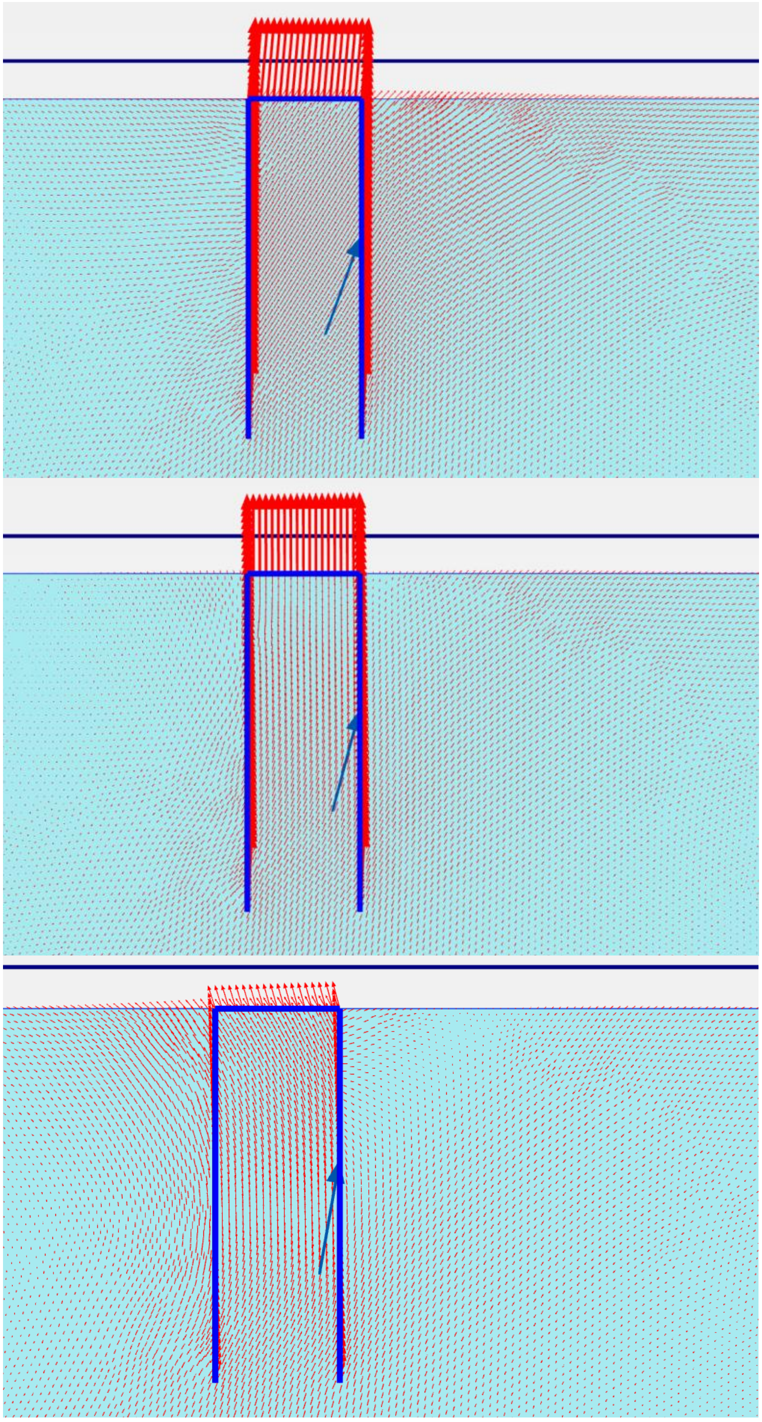

Figure 6.46 – Total displacements for a L/D = 3, $K_0 = 1 - \sin(\varphi)$, $D_r = 0.6$, $z_{pad} = 0.4$, θ =70°, 75°, 80° (Top to bottom)

Based on the figure above, it can also be observed that the total displacement values for an inclination of 80 degrees are smaller than those for an inclination of 70 degrees with the same vertical capacity for both inclinations. This can be explained by the direction of the anchor's rotation, where a counterclockwise rotation results in a greater contribution from the soil's passive components, while for a clockwise rotation, the sum of the forces acting on the anchor's side is lower than for rotations in the opposite direction.

For higher values of z_{pad}, such as 0.65, this behavior is no longer observed, and the response follows directly the envelope shown in Figure 6.47.

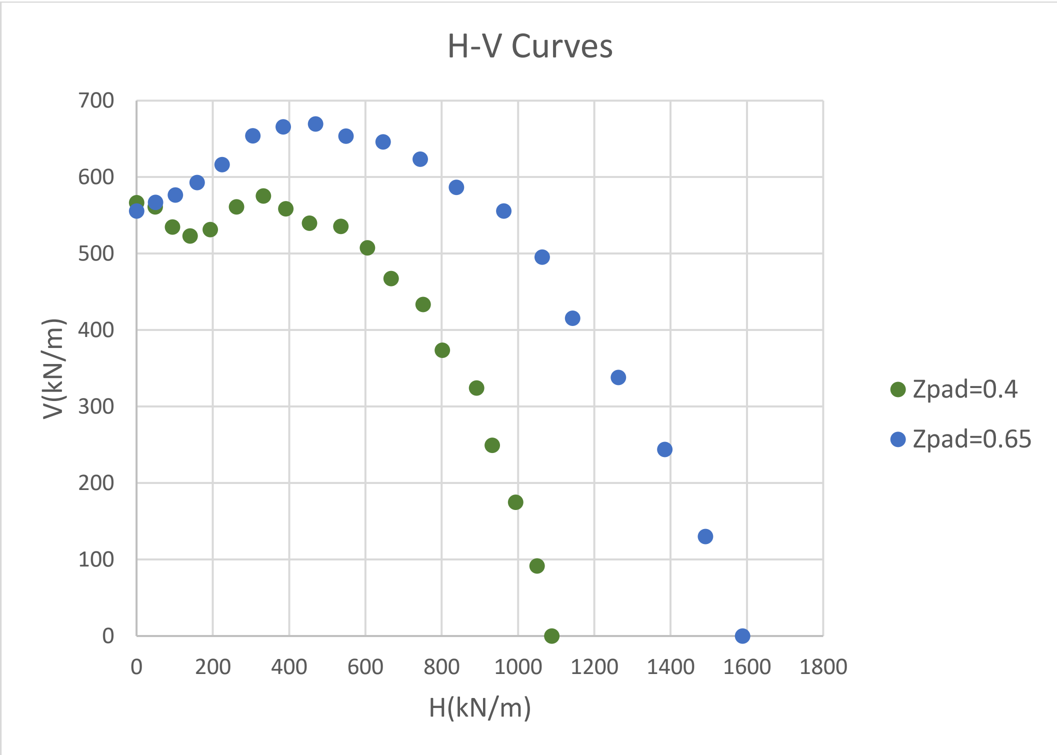

Figure 6.47 – Failure envelope for a L/D = 3, $K_0 = 1 - \sin(\varphi)$, $D_r = 0.6$, $z_{pad} = 0.4, 0.65$

The values for an inclination of 90° are very close, as previously presented in Chapter 6.4.2, as well as the increase in horizontal and inclined values with the increase of z_{pad} from 0.4 to 0.65, also previously shown in Chapters 6.4.3 and 6.4.4, respectively.

As can be seen below, for these load inclination values, the anchor rotation values are different from zero, in the counterclockwise direction. It is also possible to observe, with the increase in inclination, the formation of the failure mechanism analyzed for vertically applied forces, featuring a mobilization wedge at the front of the anchor and soil uplift at the rear.

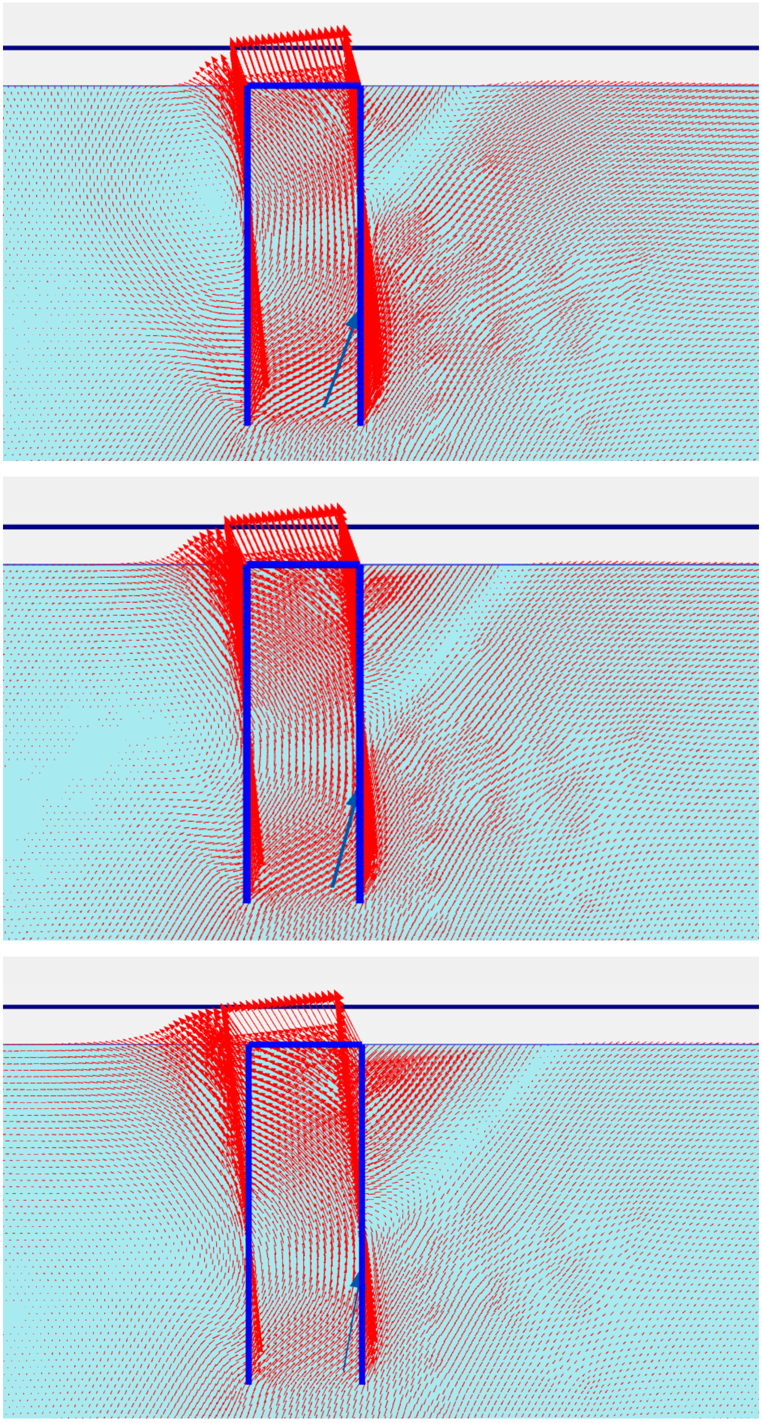

Figure 6.48 – Total displacements for a L/D = 3, $K_0 = 1 - \sin(\varphi)$, $D_r = 0.6$, $z_{pad} = 0.65$, θ =70°, 75°, 80° (Top to bottom)

7
CONCLUSION

7.1. CONCLUSIONS

This study aimed to contribute to a better understanding of the behavior of suction anchors in cohesionless soils. To this end, an extensive review of the existing literature was conducted. However, it was observed that most previous studies did not fully address the behavior of suction anchors with realistic geometries, nor did they account for the influence of the coefficient of earth pressure at rest (K_0) during anchor installation. These issues were addressed in this work, with appropriate simplifications and limitations imposed by the use of 2D FEM. The main reference studies used were Cheng et al. (2021), Hirai (2023), and Zhao et al. (2018). Notably, Hirai (2023) proposed an analytical approach distinct from the others by incorporating the “silo effect” within the interior of the anchor, leading to a nonlinear saturation of vertical effective stresses with depth. In contrast, Cheng et al. (2021) and Zhao et al. (2018) follow the approach developed by Houlsby et al. (2005), assuming that this “stress saturation” occurs externally at a distance “m” from the anchor.

Based on the results obtained in PLAXIS 2D simulations, for both axisymmetric and plane strain models, the following conclusions were drawn:

Findings Related to Vertical Loads Applied on the Top Cap of the Anchor

- When assessing the soil behavior under vertical loads applied to the top of the caisson, the “silo effect” was evident in both axisymmetric and plane strain models. This validates the comparison of numerical results with the analytical predictions from Cheng et al. (2021), Zhao et al. (2018), and Hirai (2023), with results showing closer agreement with Hirai's model. The vertical stress reduction inside the caisson, illustrated in both model types, supports the presence of the silo effect.
- Two K_0 approaches were considered: one based on Jaky's equation and another with a fixed value of 0.5. When K_0 was calculated via Jaky's equation, variations in the friction angle φ did not significantly affect the product Ktan(δ), leading to stable uplift capacity values across different φ. In contrast, when K_0 was fixed, increasing φ resulted in higher Ktan(δ) and thus greater uplift capacity.
- During anchor installation, lateral earth pressure coefficients near the surface approached values close to K_p, while values near the base were often lower than K_0. This suggests that K_0 values assumed in the analysis are representative of the actual K values in the mobilized zones. Therefore, the correlation between numerical and analytical results is validated.

Findings Related to Vertical Loads Applied on the Padeye Position

- The behavior of the caisson under vertical loads applied along the lateral skirt can be assessed in terms of uplift capacity and failure mechanisms. Unlike top-applied vertical loads, skirt-applied loads, even when using Jaky's K_0, showed increasing capacity with increasing relative density, indicating different rupture mechanisms and soil mobilization.
- For low aspect ratios ($\lambda = 3$), the failure occurs through two soil wedges, one in front of and another behind the applied load, suggesting a lower dependency on $K\tan(\delta)$ due to the anchor mobilizing surrounding soil mass.
- For higher aspect ratios ($\lambda = 6$), failure is concentrated along the caisson skirts and governed by interface friction, making $K\tan(\delta)$ a more dominant factor in defining capacity.
- Regardless of the z_{pad}, the vertical capacity remained consistent across different soil types and K_0 values. The failure mode was influenced only by caisson geometry, and the rupture mechanism remained the same for deep and shallow load application points.

Findings Related to Horizontal Loads Applied on the Padeye Position

- Relative density significantly influences soil mobilization. For higher densities, a more pronounced mobilization is observed. For varying z_{pad} values, Jaky-based K_0 causes shifts in the optimal padeye position, especially evident at z_{pad} values of 0.6 and 0.7. The disparity between these values grows with increasing D_r, indicating a shift in optimal attachment depth.
- Higher absolute capacities were recorded with fixed $K_0 = 0.5$. This is due to the free movement of the caisson under load-controlled conditions. Although a horizontal force is applied, vertical displacements also occur due to interface interaction, allowing the shear resistance component $K\tan(\delta)$ to contribute to equilibrium, increasing total load resistance.
- Different z_{pad} values correspond to distinct failure mechanisms:
    1. At $z_{pad} = 0.5$, failure occurs via two wedges: a circular wedge formed in front of the anchor due to uplift and a rear wedge sliding along the anchor, indicating clockwise rotation.
    2. At $z_{pad} = 0.65$, the failure mechanism resembles global bearing failure in shallow foundations. The front soil is uplifted, the rear wedge slides along the anchor, and the mobilized failure planes are linear. Minimal rotation occurs, indicating predominantly horizontal translation.
    3. At $z_{pad} = 0.75$, a similar failure pattern occurs, though with curved mobilization lines and incomplete surface connection. Larger counterclockwise rotations are observed compared to the $z_{pad} = 0.65$ case.

Findings Related to Inclined Loads Applied on the Padeye Position

- The influence of aspect ratio on the optimal z_{pad} position for forces inclined at 30 degrees. For cases with an aspect ratio λ=3, the optimal z_{pad} values were found within a range of 0.65 to 0.75, with the peak pullout capacity occurring at z_{pad}=0.70. In contrast, for λ=6, the optimal range shifted upward, falling between 0.70 and 0.80, with the highest capacity observed at z_{pad}=0.75. This indicates a clear relationship between the anchor's aspect ratio and the optimal point of force application under inclined loading.

- The difference between fixed and variable K_0 values showed negligible impact on pullout capacity. However, increasing the relative density D_r led to a significant rise in pullout capacity, regardless of whether a fixed or variable K_0 was used. Notably, the increase in D_r did not result in a meaningful shift in the optimal z_{pad} position.
- For the geometry with $\lambda = 6$, a greater mobilization of the optimal z_{pad} values was observed, with a more pronounced peak in pullout capacity as the relative density D_r increased, when compared to the $\lambda = 3$ case.

7.2. FUTURE WORKS

The comprehensive study on this subject remains incomplete, with several important topics yet to be fully explored or discussed in the present work. However, these aspects have been considered and analyzed to some extent and represent promising avenues for future research. Further investigation into these topics could significantly enhance the overall understanding of suction anchor behavior. Some of the key areas for future development include:

- Different Load Application Angles: When loads are applied at varying angles between 0° and 90°, the resulting maximum capacities for each angle define a failure envelope. Any combination of vertical and horizontal loads that falls within this envelope can be sustained by the anchor. Previous studies have investigated this phenomenon primarily in clay soils using commercial anchor geometries (Randolph and Gourvenec, 2005). More recent research has addressed suction anchor behavior in sands; however, these studies often do not cover commercial-scale (Cheng et al., 2021). Nevertheless, the resulting curve fits show a closer match to the real behavior of suction anchors in sand, making this an important topic for further development.
- Analysis of Anchors in Varied Soil Layers: This study focused exclusively on the behavior of suction anchors in homogeneous soil conditions, without considering the presence of stratified layers. A future investigation involving anchors embedded in layered soil profiles, whether consisting of non-cohesive soils with varying properties or combinations of cohesive and non-cohesive soils, could significantly alter the anchor behavior observed in the present work. Such an analysis would provide a more comprehensive understanding of anchor performance in more realistic geotechnical scenarios.
- Analysis of Loads Applied by Mooring Lines: It is well known that suction anchors are primarily designed to resist the forces transmitted by mooring lines. However, in this study, the mooring line itself was not explicitly modeled; instead, a simplified load was applied at a single point. A more detailed investigation that considers the actual horizontal, vertical, and inclined forces imposed by mooring lines could significantly influence the stress distribution and soil behavior around the anchor, potentially leading to different performance outcomes than those observed in the present analysis.

BIBLIOGRAPHY

All Lifting. (2019). *Different types of fiber rope*.

API RP 2SK. (2005). *Recommended Practice for Design and Analysis of Stationkeeping Systems for Floating Structures*. American Petroleum Institute.

Broms, B.B., (1964). *Lateral resistance of piles in cohesionless soils*. J. Soil Mech. Found. Div., ASCE. 90 (SM3), 123-156.

Chairat Supachawarote, Mark Randolph, and Susan Gourvenec. (2005). *Inclined Pull-out Capacity of Suction Caissons.*

Christian Lykke Jensen, Stefan Rysgaard Houmann, Troels Juul Pedersen, and Lars Bo Ibsen (2023). *Modelling the Drained Capacity of Inclined Loaded Suction Anchors in Cohesionless Soil: A Finite Element Study*.

DNVGL-RP-E303. (2017). *Recommended Practice - Geotechnical design and installation of suction anchors in clay*.

H.A. Janssen. (1895). *Experiments on Corn Pressure in Silo Cells*.

Helena Raquel Ferreira Dias. (2013). *Uma Contribuição para Conhecimento do Comportamento de Âncoras em Leitos Marinhos Arenosos para Estruturas Flutuantes.* Master thesis of University of Porto.

Hirai, H. (2023). *Failure envelope considering the ultimate tensile capacity of suction caisson in sand*.

Houlsby, G. T., Richard B. Kelly, & Byrne, B. W. (2005). *The tensile capacity of suction caissons in sand under rapid loading*. Department of Engineering Science, Oxford University.

L. Cheng, M.S. Hossain, Y. Hu, S.N Ullah. (2021). *Failure envelope of suction caisson anchors subjected to combined loadings in sand.*

L. Zhao; C. Gaudin; C. D. O'Loughlin; J. P. Hambleton, A.M. ASCE; M. J. Cassidy; and M. Herduin. (2018). *Drained Capacity of a Suction Caisson in Sand Under Inclined Loading*.

Lu, W. (2021). *Hybrid configuration of mooring line*.

Mascarucci, Y., Miliziano, S. & Mandolini, A. (2014) *A numerical approach to estimate shaft friction of bored piles in sands*. *Acta Geotech.* **9**, 547–560. https://doi.org/10.1007/s11440-014-0305-4

Matos Fernandes, M. (2020). Shallow Foundations. *Analysis and Design of Geotechnical Structures* (1st ed.). CRC Press. Boca Raton.

PLAXIS (2018). Reference manual 2D. Bentley Systems

Randolph, M. F., & Gourvenec, S. (2011). *Offshore Geotechnical Engineering*. Taylor & Francis.

Rui, S.; Xu, H.; Teng, L.; Xi, C.; Sun, X.; Zhang, H.; Shen, K. (2023). *A Framework for Mooring and Anchor Design in Sand Considering Seabed Trenches Based on Floater Hydrodynamics.* Sustainability 2023, 15, 9403. https://doi.org/10.3390/su15129403

Subrata Chakrabarti, John Halkyard, Cuneyt Capanoglu. (2005). *Handbook of Offshore Engineering. https://doi.org/10.1016/B978-008044381-2.50004-7*

Sunji Park. (2023). *Installation and Operation of Suction Caisson Anchors in Calcareous Sand*. PhD thesis of the University of Western Australia.

S.D. Nielsen. (2019). *Finite element modeling of the tensile capacity of suction caisson in cohesionless soil.* https://doi.org/10.1016/j.apor.2019.101866

Vryhof Anchors. *The Guide to Anchoring – VRYHOF Manual*.

Wenyue Lu; Lingzhi Xiong; Jianmin Yang; Xin Li. (2021). *Experimental investigation of a taut mooring line accounting for the chain–sand interaction at model scale*. https://doi.org/10.1007/s00773-021-00833-x

Zhiyu Jiang. (2021). *Installation of offshore wind turbines: A technical review* *https://doi.org/10.1016/j.rser.2020.110576*

APPENDIX

A – PYTHON SCRIPTS USED

The following section presents the Python scripts used in this study. The first command establishes the connection with PLAXIS 2D, which is executed at the beginning of every script.

```
localhostport_input = 10000
localhostport_output = 10001

import numpy as np
from plxscripting.easy import *
import os
from time import sleep

s_i, g_i = new_server('localhost', localhostport_input, password='passwordhere')
s_o, g_o = new_server('localhost', localhostport_output, password='passwordhere')
```

After establishing the connection with PLAXIS 2D, the scripts are executed, performing all the steps that would otherwise be carried out manually.

The script used for the axisymmetric model is as follows:

```
print(os.getcwd())
g_i.clear()
s_i.new()
# Input to save the file
save_file = 1 # 0 = don't save the plaxis 2d file | 1 = save the file

print("Fy", "        ", "phi", "    ", "         ", "Dr", "                         ", "error", "          ", "kvalue_pinst") #The header of the table results
```

```
# Defining the variables of the model
'''To avoid some problems with the loops, the variables are defined before the loops,
to prevent a loop with a constant variable,
and the loop can be just outlined in the code, without outlining the variables.'''
length = 9 #The length of the caisson, in meters
diam = 3 #The diameter of the caisson, in meters
gamma_unsat = 10 #The unsaturated volumetric weight of the soil, in kN/m**3
z_pad = 0 #The normalized position of the point load/displacement (z_pad = length application of the point load/ length of the caisson)
r_inter = 0.8245 #The relative interface factor, Rinter = tan(delta)/tan(phi)
phi = 35 # For a free selection of Dr
# phi = 31.028 # For a Dr = 0.4
# phi = 34.262 # For a Dr = 0.6
# phi = 38.776 # For a Dr = 0.8

'''Those are some loops that could be used to calculate the model with different values of phi, gamma unsat, diameter, length and padeye position.'''
# for gamma_unsat in [10]:
#         g_i.clear() #Is necessary to clean the model every time the loop is finished and to create a new model
#         s_i.new()
# for phi in [31.028, 34.262, 38.776]:
#         g_i.clear()
#         s_i.new()
# for diam in [3, 5, 8]:
#         g_i.clear()
#         s_i.new()
# for length in [3*diam, 5*diam ,6*diam]:
#         g_i.clear()
#         s_i.new()

x_max = 5*diam #The maximun distance of the X bounderies of the model
ko= 1 - np.sin(np.radians(phi)) #This is the calculation of the K0 value, using Jaky's equation
# ko = 0.5
```

```
f_apply_y = 350*diam**2 #The load applied in the point load, with the vertical direction

re_el = 0.06*0.667

'''This is the relative element factor, mesh() -> relative element factor(0.06*re) 0.06*0.5 for a very fine mesh 0.06*0.667 for a fine mesh, 0.06*1 for a medium mesh, 0.06*1.33 for a coarse mesh, 0.06*2 for a very coarse mesh.'''


cwd = os.getcwd()

file_name = f"plaxis_results_d_{diam}_l_{length}_gamma_{gamma_unsat}_phi_{str(phi).replace('.', '_')}_r_inter_{str(r_inter).replace('.', '_')}_ko_{str(ko).replace('.','_')}.p2dx"

file_path = r"C:\Users\Path_of_the_file"

save_path = os.path.join(file_path, file_name)

full_save_path = os.path.join(cwd, save_path)

'''In case to save the file, it will be saved in this name and path'''


#Defining the Bounderies and Project properties

g_i.Project.setproperties( "Title", "Suction Anchor", "UnitForce", "kN" , "UnitLength", "m", "UnitTemperature",

"°C", "ModelType", "Axisymmetry", "ElementType", "6-Noded")

g_i.SoilContour.initializerectangular(0, 0, x_max, x_max) #(Xmin, Ymin, Xmax, Ymax)


#Defining the plates

x_caisson_points_right = (diam/2)

A_x = np.array([0, x_caisson_points_right, x_caisson_points_right])

A_y = np.array([0, 0, -length])


#Borehole

borehole_1 = g_i.borehole(0)


#Soil

#Calculating the value of Dr following the equation of: phi=28.4 + 16*Dr**2 + 0.17*Dr

a = 16

b = 0.17

c = 28.4 - phi


# Calculate the discriminant
```

```
discriminant = b**2 - 4*a*c
if discriminant < 0:
    raise ValueError(f"Phi, for this value, do not have a real solution, phi = {phi}")

# Calculate dr (choosing the positive root)
dr = (-b + np.sqrt(discriminant)) / (2*a)
emin= 0.35
emax= 0.8
g_i.soillayer(2*length)
soil_1 = g_i.soilmat("Identification", "Sand", "SoilModel", "Hardening Soil", "gammaUnsat", gamma_unsat,
"gammaSat", gamma_unsat + 9.81, "eInit", emax-dr*(emax-emin) , "EURRef", 36E3, "EOedRef" , 9700 , "E50Ref" , 12E3 , "nuUR", 0.3, "cRef", 0.5, "phi", phi,
"psi", 0, "DilatancyCutOff", True, "eMin", emin, "eMax", emax, "TensionCutOff", False,
"GroundwaterClassificationType", "USDA", "GroundwaterSoilClassUSDA", "Sand", "GwUseDefaults", True, "GwDefaultsMethod",
"From grain size distribution", "InterfaceStrengthDetermination", "Manual", "Rinter", 0.8245, "DeltaInter", 0.1,
"K0Determination", "Manual", "K0Primary", ko)

'''Those are some other attributions possibilities for the soil properties, different from the last one, this don't need to follow a sequence.'''
# g_i.Sand.TensionCutOff.set(False)
# g_i.Sand.DilatancyCutOff.set(True)
# g_i.Sand.eMin.set(0.35)
g_i.Soils[0].Material = soil_1    #Applying the soil_1

#Defining points
points = []
for i in range(len(A_x)):
    points.append(g_i.Geometry.point(A_x[i], A_y[i]))
    points.append(g_i.Geometry.point(0, 0)) #Point of the caisson to apply the force
caisson_contour = g_i.Geometry.point((x_caisson_points_right + diam, - length*1.5), (x_caisson_points_right + diam, 0), (x_caisson_points_right + diam, -length*1.5), (0, -length*1.5))
'''The caisson contour will have 1D of radius distance and 1.5L of the depth below the caisson tip'''
```

```
#Defining lines
lines = []
for i in range(len(A_x) -1 ):
        lines.append(g_i.Geometry.line(points[i], points[i + 1]))

#Defining the Plates
caisson = g_i.plate(lines[0], lines[1])
steel = g_i.platemat("Identification", "Steel", "MaterialType", "Elastic", "w", 6.869,
"EA1", 21e12, "EI", 17.5e9)
#Volumetric weight of the steel (78.5-9.81) kN/m^3 * 0.1m(thickness) = 6.869 kN/m/m
#EA = E * h(thickness) b = 1m(plane strain/axisymmetry)
g_i.setmaterial(caisson, steel) #EI = E * (h**3)/ 12
load_point_4 = g_i.pointload(points[-1], "Fx", 0, "Fy", f_apply_y) #Application of the load in the last point defined, the point on the center top cap of the caisson

#Defining Negative and Positive interface
g_i.neginterface(lines)
g_i.posinterface(lines)

#Defining the polygon around the caisson
retang_refinement = g_i.Geometry.line(caisson_contour[0], caisson_contour[1], caisson_contour[2], caisson_contour[3])

#Defining the Phases
g_i.gotostages()
phase_initial = g_i.InitialPhase #The initial phase
phase_initial.Deform.SumMweight.set(1) #Applying the weight of the soil in the initial phase
phase_instalation = g_i.phase(phase_initial) #The instalation phase
phase_plastic_nil = g_i.phase(phase_instalation) #The plastic nil phase, to ensure that the stress field is in equilibrium before the load is applied
phase_1 = g_i.phase(phase_plastic_nil) #The loading phase
phase_initial.UseCompressionForResultFiles.set(True) #Compression for the result files, to save space in the disk
phase_instalation.UseCompressionForResultFiles.set(True)
```

phase_plastic_nil.UseCompressionForResultFiles.set(True)

phase_1.UseCompressionForResultFiles.set(True)

phase_plastic_nil.Deform.ResetDisplacementsToZero.set(False) #Reset the displacements to zero in the plastic nil phase

phase_instalation.Deform.ResetDisplacementsToZero.set(False) #Reset the displacements to zero in the instalation phase

phase_1.Deform.ResetDisplacementsToZero.set(True) #Reset the displacements to zero in the loading phase

phase_1.Deform.ResetSmallStrain.set(True) #Reset the small strain in the loading phase

Defining the parameters of the calculation phase

phase_1.Deform.UseDefaultIterationParams.set(False)

phase_1.Deform.MaxLoadFractionPerStep.set(50/f_apply_y) #The max load fraction per step avoid application of a load that is too high, and the model goes to the wrong collapse

phase_1.Deform.MaxIterations.set(100) #The max iterations in the calculation phase

phase_1.Deform.ArcLengthControl.set('on') #Arc length control is recomended for a load-controled analysis

phase_1.Deform.MaxSteps.set(2000) #The max steps in the calculation phase

phase_1.Deform.OverRelaxation.set(1) #For friction angles, lower than 20 degrees, the overrelaxation should be around 1.5,for high friction angles, the overrelaxation sould be lower than 1

Defining the name of the phases and activating the Groundwater Flow, Plates, Interfaces and Line/Point loads

phase_plastic_nil.setproperties("Identification", "Plastic Nil Phase") #The name of the plastic nil phase

phase_instalation.setproperties("Identification", "Instalation of the Pile") #The name of the instalation phase

phase_1.setproperties("Identification", "Instalation of the Load") #The name of the loading phase

g_i.Plates.activate(phase_instalation) #Activating the plates in the instalation phase

g_i.Interfaces.activate(phase_instalation) #Activating the interfaces in the instalation phase

g_i.GroundwaterFlowBCs.activate(phase_instalation) #Activating the groundwater flow in the instalation phase

g_i.PointLoads.activate(phase_1) #Activating the point loads in the loading phase

#Defining the Water Level

g_i.gotowater()

water_level = g_i.waterlevel((0,1), (x_max,1)) #Defining the water level in the model 1m above the mudline

g_i.UserWaterLevel_1.Points[1].Pinc.set(1)

g_i.UserWaterLevel_1.Points[0].Pinc.set(1)

g_i.setglobalwaterlevel(water_level, phase_initial) #Setting the global water level in the initial phase

#Defining the mesh

g_i.gotomesh()

g_i.BoreholePolygon_1_1.CoarsenessFactor.set(0.1) #The coarseness factor of the soil inside the cluster

g_i.BoreholePolygon_1_2.CoarsenessFactor.set(1) #The coarseness factor of the soil outside the cluster

g_i.Line_1_1.CoarsenessFactor.set(0.1) #The coarseness factor of the caissons lines

g_i.Line_2_1.CoarsenessFactor.set(0.1)

g_i.BoundaryLine_1.CoarsenessFactor.set(0.1) #The coarseness factor f the top boundary within the cluster

g_i.BoundaryLine_2.CoarsenessFactor.set(1) #The coarseness factor of the top boundary outside the cluster

g_i.BoundaryLine_3.CoarsenessFactor.set(0.1) #The coarseness factor of the left boundary within the cluster

g_i.BoundaryLine_4.CoarsenessFactor.set(1) #The coarseness factor of the right boundary

g_i.BoundaryLine_5.CoarsenessFactor.set(1) #The coarseness factor of the left boundary outside the cluster

g_i.BoundaryLine_6.CoarsenessFactor.set(1) #The coarseness factor of the bottom boundary

g_i.mesh(re_el) #for mesh() -> relative element factor(0.06*re_el) 0.06*0.5 for a very fine mesh, 0.06*0.67 for a fine mesh, 0.06*1 for a medium mesh, 0.06*1.33 for a coarse mesh, 0.06*2 for a very coarse mesh

#for meshd()-> element relative size(le = 0.06 * re_el * sqrt((xmax - xmin)**2+(ymax - ymin)**2))

g_i.selectmeshpoints() #Opening the PLAXIS 2D Output to select the curve points

for i in np.arange(0.5 , length, length/50):

    g_o.addcurvepoint('stresspoint', (diam/2+0.01, -i))

g_o.update() #Updating the PLAXIS 2D Output to apply the curve points in the calculations

#Calculating the model

g_i.gotostages()

g_i.calculate()

```
# Handling with the results
g_i.view(phase_1) #Opening the PLAXIS 2D Output in the Phase 1 to see the results
phase_instalation_o = get_equivalent(phase_instalation, g_o) #Equivalent phases in the PLAXIS 2D Output
phase_1_o = get_equivalent(phase_1, g_o)
sigma_xx_eff_p1 = []
sigma_yy_eff_p1 = []
sigma_xx_eff_pinst = []
sigma_yy_eff_pinst = []
kvalue_p1 = []
kvalue_pinst = []
for i in range(0, len(g_o.CurvePoints)): #Getting the results of the curve points to calculate the kvalue in the instalation phase
    sigma_xx_eff_pinst.append(g_o.getcurveresults(g_o.CurvePoints[i], phase_instalation_o, g_o.RT_Soil.SigxxE))
    sigma_yy_eff_pinst.append(g_o.getcurveresults(g_o.CurvePoints[i], phase_instalation_o, g_o.RT_Soil.SigyyE))
    kvalue_pinst.append(sigma_xx_eff_pinst[i]/sigma_yy_eff_pinst[i])
g_o.structureplot(caisson) #Plotting the caisson in the PLAXIS 2D Output
g_o.Plots[-1].ScaleFactor.set(20) #Setting the scale factor of the caisson plot
sum_mstage_raw = g_o.Steps[-6].Reached.SumMstage.echo() #Getting the SumMstage in the Step with the maximun load applied as a string
sum_mstage = float(sum_mstage_raw[sum_mstage_raw.find(":")+1:]) #Converting the string to a float
error_last_phase1 = g_i.Phases[-1].LogInfo.echo()[18:] #Getting the error of the last phase as a printed in the PLAXIS 2D
error_last_phase = error_last_phase1[:error_last_phase1.find(".")+1] #Converting the error of the last phase to a single sentence
kvalue_pinst_mean = sum(kvalue_pinst)/len(kvalue_pinst) #Calculating the mean of the kvalue in the instalation phase of each curve point
print(round(sum_mstage*2*np.pi*f_apply_y,2),"     ", phi,"      ","     ", round(dr,2),"      ", error_last_phase, "     ", round(kvalue_pinst_mean,3)) #Printing the results in the console
sleep(3) #Waiting for 3 seconds to ensure that the Output will not close without saving
g_o.close() #Closing the PLAXIS 2D Output
sleep(3) #Waiting for 3 seconds to ensure that the computer will start the next calculation with the PLAXIS 2D Output closed
```

#Save the file

if save_file == 1 and error_last_phase == "Soil body seems to collapse.": #The file will be saved only if the error of the last phase is "Soil body seems to collapse." to analyze the results

g_i.save(full_save_path)

For the Plane strain model:

```
print(os.getcwd())
g_i.clear()
s_i.new()
# Input to save the file

save_file = 1 # 0 = don't save the plaxis 2d file | 1 = save the file
save_image = 0 # 0 = don't save the image of the ratation | 1 = save the image of the rotation

# Defining the variables of the model
'''To avoid some problems with the loops, the variables are defined before the loops,
to prevent a loop with a constant variable,
and the loop can be just outlined in the code, without outlining the variables.'''
gamma_unsat = 10 #The volumetric unsaturated weight of the soil in kN/m**3
z_pad = -0.65 #The normalized position of the point load/displacement (z_pad = length application of the point load/ length of the caisson)
# phi = 35 # For a free selection of phi
# phi = 31.028 # For a Dr = 0.4
# phi = 34.262 # For a Dr = 0.6
phi = 38.776 # For a Dr = 0.8
diam = 3 #The diameter of the caisson in meters
length = 6*diam #The length of the caisson in meters
alpha_pad = 0 #The angle of the load in degrees
r_inter = 0.8245 #The relative interface factor, Rinter = tan(delta)/tan(phi)
alpha_pad_i = 10 #The initial angle of the load in degrees
alpha_pad_f = 60 #The final angle of the load in degrees

'''Those are some loops that could be used to calculate the model with different values of phi, gamma unsat, diameter, length and padeye position.'''
# for phi in []:
#	g_i.clear() #Is necessary to clean the model every time the loop is finished and to create a new model
#	s_i.new()
```

```
# for ko in []:
#       g_i.clear()
#       s_i.new()
# for diam in []:
#       g_i.clear()
#       s_i.new()
# for length in []:
#       g_i.clear()
#       s_i.new()
# for alpha_pad in []:
#       g_i.clear()
#       s_i.new()
# for z_pad in []:
#       g_i.clear()
#       s_i.new()

x_max = 30*diam #The maximun distance of the X bounderies of the model
ko = 1 - np.sin(phi*np.pi/180) #This is the calculation of the K0 value, using Jaky's equation
# ko = 0.5
f_apply_x = 250*np.cos(alpha_pad*np.pi/180)*length*diam #The load applied in the point load, with the horizontal direction
f_apply_y = 250*np.sin(alpha_pad*np.pi/180)*length*diam #The load applied in the point load, with the vertical direction
re_el = 0.06*0.667
'''This is the relative element factor, mesh() -> relative element factor(0.06*re) 0.06*0.5 for a very fine mesh
0.06*0.667 for a fine mesh, 0.06*1 for a medium mesh, 0.06*1.33 for a coarse mesh, 0.06*2 for a very coarse mesh.'''

cwd = os.getcwd()
file_name = f"plaxis_results_d_{diam}_l_{length}_gamma_{gamma_unsat}_phi_{str(phi).replace('.', '_')}_alpha_{alpha_pad}_zpad_{str(z_pad).replace('.', '_')}_r_inter_{str(r_inter).replace('.', '_')}_ko_{str(ko).replace('.','_')}.p2dx"
file_path = r"C:\Users\Path_of_the_file"
save_path = os.path.join(file_path, file_name)
```

```
full_save_path = os.path.join(cwd, save_path)
'''In case to save the file, it will be saved in this name and path'''

#Defining the Bounderies and Project properties
g_i.Project.setproperties( "Title", "Suction Anchor", "UnitForce", "kN" , "UnitLength", "m", "UnitTemperature", "°C", "ModelType", "Plane strain", "ElementType", "6-Noded")
g_i.SoilContour.initializerectangular(0, 0, x_max, x_max) #(Xmin, Ymin, Xmax, Ymax)

#Defining the plates
x_caisson_point_center = x_max/2.5
x_caisson_points_left = (x_caisson_point_center - diam/2) #The caisson will be placed 1/2.5 distance of the left boundary
x_caisson_points_right = (x_caisson_point_center + diam/2)
A_x = np.array([x_caisson_points_left, x_caisson_points_left,x_caisson_points_right,x_caisson_points_right])
A_y = np.array([-length, 0, 0, -length])

#Borehole
borehole_1 = g_i.borehole(0)

#Soil
#Calculating the value of Dr following the equation of: phi=28.4 + 16*Dr**2 + 0.17*Dr
a = 16
b = 0.17
c = 28.4 - phi

# Calculating the discriminant
discriminant = b**2 - 4*a*c
if discriminant < 0:
    raise ValueError(f"Phi, for this value, do not have a real solution, phi = {phi}")

# Calculating dr (choosing the positive root)
dr = (-b + np.sqrt(discriminant)) / (2*a)
emin= 0.35
```

```
emax= 0.8

g_i.soillayer(3*length) #The depth of the soil layer

soil_1 = g_i.soilmat("Identification", "Sand", "SoilModel", "Hardening Soil", "gammaUnsat", gamma_unsat + 9.81,

"gammaSat", gamma_unsat + 9.81, "eInit", emax-dr*(emax-emin) , "EURRef", 36E3, "EOedRef" , 9700 , "E50Ref" , 12E3 , "nuUR", 0.3, "cRef", 0.5, "phi", phi,

"psi", 0, "DilatancyCutOff", True, "eMin", emin, "eMax", emax, "TensionCutOff", False,

"GroundwaterClassificationType", "USDA", "GroundwaterSoilClassUSDA", "Sand", "GwUseDefaults", True, "GwDefaultsMethod", "From grain size distribution",

"InterfaceStrengthDetermination", "Manual", "Rinter", r_inter, "DeltaInter", 0.1, "K0Determination", "Manual", "K0Primary", ko)


'''Those are some other attributions possibilities for the soil properties, different from the last one, this don't need to follow a sequence.'''

# g_i.Sand.TensionCutOff.set(False)

# g_i.Sand.DilatancyCutOff.set(True)

# g_i.Sand.eMin.set(0.35)

g_i.Soils[0].Material = soil_1 #Applying the soil_1 in the first soil created


#Defining points

points = []

for i in range(len(A_x)):

        points.append(g_i.Geometry.point(A_x[i], A_y[i]))

points.append(g_i.Geometry.point(x_caisson_points_right, length*z_pad)) #Point of the caisson to apply the force

caisson_contour = g_i.Geometry.point((x_caisson_points_left - 2*length/np.tan((45+phi/2)*np.pi/180), 0), (x_caisson_points_left - 2*length/np.tan((45+phi/2)*np.pi/180), -length*1.5), (x_caisson_points_right + 1.2*length/np.tan((45-phi/2)*np.pi/180), - length*1.5), (x_caisson_points_right + 1.2*length/np.tan((45-phi/2)*np.pi/180), 0))

'''The caisson contour will have the shape of a global shallow foundation rupture, with the soil uplifting of a 1.2*length/tan(pi/4-phi/2) distance of the right caisson skirt, and a soil downsliding of a 2*length/tan(pi/4+phi/2) distance of the left caisson skirt.'''


#Defining lines

lines = []

for i in range(len(A_x) -1 ):

    lines.append(g_i.Geometry.line(points[i], points[i + 1]))
```

#Defining the Plates

caisson = g_i.plate(lines[0], lines[1], lines[2])

steel = g_i.platemat("Identification", "Steel", "MaterialType", "Elastic", "w", 6.869, "EA1", 21e12, "EI", 17.5e9) #Volumetric weight of the steel (78.5-9.81) kN/m^3 * 0.1m(thickness) = 6.869 kN/m/m

#EA = E*h(thickness) b=1m (plane strain/axisymmetry) in this case using a high value of E = 210e12kN/m**2

g_i.setmaterial(caisson, steel) #EI = E*(h**3)/12

load_point_4 = g_i.pointload(points[4], "Fx",f_apply_x , "Fy", f_apply_y) #Application of the load in the points[4], the point on the zpad

#Defining Negative and Positive interface

g_i.neginterface(lines)

g_i.posinterface(lines[0], lines[2])

#Defining the cluster around the caisson

retang_refinement = g_i.Geometry.line(caisson_contour[0], caisson_contour[1], caisson_contour[2], caisson_contour[3])

#Defining the Phases

g_i.gotostages()

phase_initial = g_i.InitialPhase #The initial phase

phase_initial.Deform.SumMweight.set(1) #Applying the weight of the soil in the initial phase

phase_instalation = g_i.phase(phase_initial) #The instalation phase

phase_plastic_nil = g_i.phase(phase_instalation) #The plastic nil phase, to ensure that the stress field is in equilibrium before the load is applied

phase_1 = g_i.phase(phase_plastic_nil)   #The loading phase

phase_initial.UseCompressionForResultFiles.set(True) #Compression for the result files, to save space in the disk

phase_instalation.UseCompressionForResultFiles.set(True)

phase_plastic_nil.UseCompressionForResultFiles.set(True)

phase_1.UseCompressionForResultFiles.set(True)

phase_plastic_nil.Deform.ResetDisplacementsToZero.set(False) #Reset the displacements to zero in the plastic nil phase

phase_instalation.Deform.ResetDisplacementsToZero.set(False) #Reset the displacements to zero in the instalation phase

phase_1.Deform.ResetDisplacementsToZero.set(True) #Reset the displacements to zero in the loading phase

phase_1.Deform.ResetSmallStrain.set(True) #Reset the small strain in the loading phase

Defining the parameters of the calculation phase

phase_1.Deform.UseDefaultIterationParams.set(False)

phase_1.Deform.MaxLoadFractionPerStep.set(150/(200*length*diam)) #The max load fraction per step avoid application of a load that is too high, and the model goes to the wrong collapse

phase_1.Deform.MaxIterations.set(100) #The max iterations in the calculation phase

phase_1.Deform.ArcLengthControl.set('on') #Arc length control is recomended for a load-controled analysis

phase_1.Deform.MaxSteps.set(2000) #The max steps in the calculation phase

phase_1.Deform.OverRelaxation.set(1) #For friction angles, lower than 20 degrees, the overrelaxation should be around 1.5,for high friction angles, the overrelaxation sould be lower than 1

Defining the name of the phases and activating the Groundwater Flow, Plates, Interfaces and Line/Point loads

phase_plastic_nil.setproperties("Identification", "Plastic Nil Phase")

phase_instalation.setproperties("Identification", "Instalation of the pile")

phase_1.setproperties("Identification", "Instalation of the load")

g_i.Plates.activate(phase_instalation) #Activating the plates in the instalation phase

g_i.Interfaces.activate(phase_instalation) #Activating the interfaces in the instalation phase

g_i.GroundwaterFlowBCs.activate(phase_instalation) #Activating the groundwater flow in the instalation phase

g_i.PointLoads.activate(phase_1) #Activating the point loads in the loading phase

#Defining the Water Level

g_i.gotowater()

water_level = g_i.waterlevel((0,1), (x_max,1)) #Defining the water level in the model 1m above the mudline

g_i.UserWaterLevel_1.Points[1].Pinc.set(1)

g_i.UserWaterLevel_1.Points[0].Pinc.set(1)

g_i.setglobalwaterlevel(water_level, phase_initial) #Setting the global water level in the initial phase

#Defining the mesh

```
g_i.gotomesh()

g_i.BoreholePolygon_1_1.CoarsenessFactor.set(0.1) #Defining the coarseness factor of the cluster around the caisson

g_i.BoreholePolygon_1_2.CoarsenessFactor.set(0.25) #Defining the coarseness factor of the rest of the soil

g_i.Line_1_1.CoarsenessFactor.set(0.1) #Defining the coarseness factor of the caisson

for i in range(0, 9):
    g_i.points[i].CoarsenessFactor.set(0.1) #Defining the coarseness factor of the caisson points

g_i.Line_2_1.CoarsenessFactor.set(0.1) #Defining the coarseness factor of the caisson

g_i.Line_3_1.CoarsenessFactor.set(0.1) #Defining the coarseness factor of the caisson

g_i.Line_3_2.CoarsenessFactor.set(0.1) #Defining the coarseness factor of the caisson

g_i.Line_4_1.CoarsenessFactor.set(0.1) #Defining the coarseness factor of the lines around the cluster

g_i.Line_5_1.CoarsenessFactor.set(0.1) #Defining the coarseness factor of the lines around the cluster

g_i.Line_6_1.CoarsenessFactor.set(0.1) #Defining the coarseness factor of the lines around the cluster

g_i.BoundaryLine_1.CoarsenessFactor.set(0.25) #Defining the coarseness factor of the top boundary

g_i.BoundaryLine_2.CoarsenessFactor.set(0.1) #Defining the coarseness factor of the top boundary on the cluster

g_i.BoundaryLine_3.CoarsenessFactor.set(0.1) #Defining the coarseness factor of the top boundary on the cluster

g_i.BoundaryLine_4.CoarsenessFactor.set(0.25) #Defining the coarseness factor of the top boundary

g_i.BoundaryLine_5.CoarsenessFactor.set(1) #Defining the coarseness factor of the left boundary

g_i.BoundaryLine_6.CoarsenessFactor.set(1) #Defining the coarseness factor of the right boundary

g_i.BoundaryLine_7.CoarsenessFactor.set(1) #Defining the coarseness factor of the bottom boundary

g_i.mesh(re_el)    #for mesh() -> relative element factor(0.06*re) 0.06*0.5 for a very fine mesh, 0.06*0.67 for a fine mesh, 0.06*1 for a medium mesh, 0.06*1.33 for a coarse mesh, 0.06*2 for a very coarse mesh

#for meshd()-> element relative size(  le = 0.06 * re * sqrt((xmax - xmin)**2+(ymax - ymin)**2)  )

g_i.selectmeshpoints() #Opening the PLAXIS 2D Output to select the curve points

curve_point1 = g_o.addcurvepoint("node", g_i.Plate_2_1,(x_caisson_point_center, 0)) #Curve point in the center of the caisson

curve_point2 = g_o.addcurvepoint('node', g_i.Plate_3_1, (x_caisson_points_right, z_pad*length)) #Curve point in the point load

g_o.update() #Updating the PLAXIS 2D Output to apply the curve points in the calculations


#Calculating the model

g_i.gotostages()
```

```
g_i.calculate()

# Handling with the results
g_i.view(phase_1) #Opening the PLAXIS 2D Output in the Phase 1 to see the results
phase_1_o = get_equivalent(phase_1, g_o) #Equivalent phase in the PLAXIS 2D Output
curve_point1_o = g_o.CurvePoints.Nodes[0] #Curve points in the Output
curve_point2_o = g_o.CurvePoints.Nodes[1]
g_o.structureplot(caisson) #Plotting the caisson in the PLAXIS 2D Output
g_o.Plots[-1].ScaleFactor.set(20) #Setting the scale factor of the caisson plot
rotation = g_o.getsingleresult(g_o.Steps[-6], g_o.ResultTypes.Plate.Rot2D, (x_caisson_point_center, 0)) #Getting the rotation of the caisson in the step with the maximum load applied
ux_displacements_cap = g_o.getcurveresults(curve_point1_o, g_o.Steps[-6], g_o.ResultTypes.Plate.Ux) #Getting the horizontal displacements of the caisson in the step with the maximum load applied
uy_displacements_cap = g_o.getcurveresults(curve_point1_o, g_o.Steps[-6], g_o.ResultTypes.Plate.Uy) #Getting the vertical displacements of the caisson in the step with the maximum load applied
ux_displacements_pointload = g_o.getcurveresults(curve_point2_o, g_o.Steps[-6], g_o.ResultTypes.Plate.Ux) # " " horizontal " " "...
uy_displacements_pointload = g_o.getcurveresults(curve_point2_o, g_o.Steps[-6], g_o.ResultTypes.Plate.Uy) # " " vertical " " "...
sum_mstage_raw = g_o.Steps[-6].Reached.SumMstage.echo() #Getting the SumMstage in the Step with the maximun load applied as a string
sum_mstage = float(sum_mstage_raw[sum_mstage_raw.find(":")+1:]) #Converting the SumMstage to a float number
error_last_phase1 = g_i.Phases[-1].LogInfo.echo()[18:] #Getting the error of the last phase as printed in the PLAXIS 2D
error_last_phase = error_last_phase1[:error_last_phase1.find(".")+1] #Converting the error of the last phase to a single sentence
if alpha_pad == alpha_pad_i: #Used in some cases with multiples angles of the loading, printing the header only once
        print("ForceX","     ","ForceY","    ", "alphapads", "    ", "zpads", "    ","phi","     ",
   "        ","Dr","        ", "error","                          ", "Rotation","        " ,
   "Uxcap", "       ", "Uycap", "      ","Uxpointload", "  ", "Uypointload") #The header of the results
print(round(sum_mstage*f_apply_x,    2),"        ",round(sum_mstage*f_apply_y,    2),"                    ", alpha_pad,"            ",
   round(z_pad, 2),"    ", phi,"       ","    ", round(dr,3),"       ", error_last_phase, "       ",
```

```
    round(rotation,5), "      ", round(ux_displacements_cap,5), "      ", round(uy_displacements_cap,5), "     ", round(ux_displacements_pointload,5), "     ",
    round(uy_displacements_pointload,5)) #The results of the calculations
image_path = r"C:\repos\mt_renzo\PLAXIS_2D\plaxis_results\imagens" #The path to save the image of the rotation
save_image_path = os.path.join(image_path, file_name.replace(".p2dx", ".png")) #The name of the image to save, with the same name of the file
if save_image == 1:
        g_o.Plots[-1].export(save_image_path) #Saving the image of the rotation
sleep(3) #Waiting for 3 seconds to ensure that the computer do not crash with the saving
g_o.close() #Cloasing the PLAXIS 2D Output
sleep(3) #Waiting for 3 seconds to ensure that the computer will start the next calculation with the PLAXIS 2D Output closed

#Saving the file
if save_file == 1 and error_last_phase == "Soil body seems to collapse.": #The file will be saved only if the error of the last phase is "Soil body seems to collapse." to analyze the results
        g_i.save(save_path)
```

The script above represents the application of forces at the padeye, both in the horizontal and vertical directions. It also allows for analyses at various load angles by implementing loops that apply forces, save the results, and subsequently analyze them. Although this type of analysis was initiated, it could not be fully developed due to time management constraints. The calculations for the force applied at the top of the anchor were performed using the same script, with modifications only to the "Defining the points" section, as shown below:

From

```
#Defining points
points = []
for i in range(len(A_x)):
	points.append(g_i.Geometry.point(A_x[i], A_y[i]))
points.append(g_i.Geometry.point(x_caisson_points_right, length*z_pad))	#Point of the caisson to apply the force
```

to

```
#Defining points
points = []
for i in range(len(A_x)):
	points.append(g_i.Geometry.point(A_x[i], A_y[i]))
points.append(g_i.Geometry.point(x_caisson_point_center, 0)) #Point of the caisson to apply the force
```

B – THE RESULTS OF THE CALCULATIONS

The presented table is related with the vertical forces calculated, with the loads applied on the top cap of the caisson, for the values of φ = 31.028, 34.262 and 38.776 are equal to the D_r values of 0.4, 0.6 and 0.8 respectively:

Table 9 – Results from Axisymmetric model $K_0 = 1 - \sin(\varphi)$

Values of Vult using γ' = 10 Ktan(δ) = 0.24					
D(m)	L(m)	φ (°)	Fy (kN)	Fy/W (-)	k (-)
3	9	31.028	2065.09	3.41	0.9
3	15	31.028	4609.4	4.70	1.5
3	18	31.028	6210.32	5.31	1.8
5	15	31.028	8235	4.81	1.5
5	25	31.028	19285.7	6.97	2.5

D(m)	L(m)	φ (°)	Fy (kN)	Fy/W (-)	k (-)
5	30	31.028	26323.05	7.99	3
8	24	31.028	30729.41	6.95	2.4
8	40	31.028	74347.13	10.40	4
8	48	31.028	102238.25	12.01	4.8
Values of Vult using γ’ = 10 Ktan(δ) = 0.245					
D(m)	L(m)	φ (°)	Fy (kN)	Fy/W (-)	k (-)
3	9	34.262	2033.37	3.36	0.9
3	15	34.262	4614.45	4.70	1.5
3	18	34.262	6252.2	5.35	1.8
5	15	34.262	8159.13	4.77	1.5
5	25	34.262	19404.48	7.01	2.5
5	30	34.262	26675.49	8.09	3
8	24	34.262	30587.81	6.92	2.4
8	40	34.262	74669.1	10.45	4
8	48	34.262	102625.7	12.06	4.8
Values of Vult using γ’ = 10 Ktan(δ) = 0.248					
D(m)	L(m)	φ (°)	Fy (kN)	Fy/W (-)	k (-)
3	9	38.776	2040.1	3.37	0.9
3	15	38.776	4354.51	4.44	1.5
3	18	38.776	6425.18	5.50	1.8
5	15	38.776	8236.22	4.82	1.5
5	25	38.776	19650.83	7.10	2.5
5	30	38.776	27264.23	8.27	3
8	24	38.776	30538.13	6.91	2.4
8	40	38.776	75823.56	10.61	4
8	48	38.776	96446.47	11.33	4.8

Table 10 – Results from Axisymmetric model K_0 = 0.5

Values of Vult using γ’ = 10 Ktan(δ) = 0.248					
D(m)	L(m)	φ (°)	Fy (kN)	Fy/W (-)	k (-)
3	9	31.028	2086.06	3.45	0.9
3	15	31.028	4664.85	4.76	1.5

D(m)	L(m)	φ (°)	Fy (kN)	Fy/W (-)	k (-)
3	18	31.028	6294.32	5.39	1.8
5	15	31.028	8349.22	4.88	1.5
5	25	31.028	19570.12	7.07	2.5
5	30	31.028	26738.45	8.11	3
8	24	31.028	31285.5	7.08	2.4
8	40	31.028	75491.15	10.56	4
8	48	31.028	103951.73	12.21	4.8
Values of Vult using γ' = 10 Ktan(δ) = 0.281					
D(m)	L(m)	φ (°)	Fy (kN)	Fy/W (-)	k (-)
3	9	34.262	2212.69	3.65	0.9
3	15	34.262	4991.27	5.09	1.5
3	18	34.262	6765.24	5.79	1.8
5	15	34.262	8951.6	5.23	1.5
5	25	34.262	21032.53	7.60	2.5
5	30	34.262	28882.15	8.76	3
8	24	34.262	33714.6	7.63	2.4
8	40	34.262	81420.42	11.39	4
8	48	34.262	112690.74	13.24	4.8
Values of Vult using γ' = 10 Ktan(δ) = 0.331					
D(m)	L(m)	φ (°)	Fy (kN)	Fy/W (-)	k (-)
3	9	38.776	2388.34	3.94	0.9
3	15	38.776	5471.26	5.58	1.5
3	18	38.776	7487.17	6.41	1.8
5	15	38.776	9783.66	5.72	1.5
5	25	38.776	23241.74	8.40	2.5
5	30	38.776	32151.4	9.75	3
8	24	38.776	37059.06	8.38	2.4
8	40	38.776	90439.79	12.65	4
8	48	38.776	126569.21	14.87	4.8

Table 11 – Results from analytical solutions $K_0 = 1 - \sin(\varphi)$

Values of analytical solutions using γ' = 10 Ktan(δ) = 0.24								
D(m)	L(m)	φ (°)	Hirai (kN)	Cheng (kN)	Zhao (kN)	V_{Hirai}/W (-)	V_{Cheng}/W (-)	V_{Zhao}/W (-)
3	9	31.028	1905.79	2003.93	1997.33	3.15	3.31	3.30
3	15	31.028	4274.33	4756.94	4739.13	4.36	4.85	4.83
3	18	31.028	5767.25	6567.02	6541.56	4.93	5.62	5.60
5	15	31.028	7812.63	8293.77	8262.72	4.57	4.85	4.83
5	25	31.028	18190.48	20523.35	20439.62	6.57	7.42	7.38
5	30	31.028	24810.53	28673.13	28553.46	7.53	8.70	8.66
8	24	31.028	29606.22	31638.29	31509.94	6.70	7.16	7.13
8	40	31.028	70729.32	80508.58	80162.63	9.90	11.26	11.22
8	48	31.028	97158.10	113342.80	112848.44	11.42	13.32	13.26
Values of Vult using γ' = 10 Ktan(δ) = 0.245								
D(m)	L(m)	φ (°)	Hirai (kN)	Cheng (kN)	Zhao (kN)	V_{Hirai}/W (-)	V_{Cheng}/W (-)	V_{Zhao}/W (-)
3	9	34.262	1928.45	2033.80	2027.07	3.18	3.36	3.35
3	15	34.262	4332.38	4837.60	4819.41	4.42	4.93	4.91
3	18	34.262	5849.33	6682.34	6656.34	5.00	5.72	5.70
5	15	34.262	7918.58	8434.41	8402.70	4.63	4.93	4.91
5	25	34.262	18460.65	20902.66	20817.14	6.67	7.55	7.52
5	30	34.262	25191.99	29215.23	29093.01	7.64	8.86	8.83
8	24	34.262	30042.62	32219.75	32088.65	6.80	7.29	7.26
8	40	34.262	71839.27	82075.75	81722.42	10.05	11.48	11.43
8	48	34.262	98724.11	115582.25	115077.34	11.60	13.58	13.52
Values of Vult using γ' = 10 Ktan(δ) = 0.248								
D(m)	L(m)	φ (°)	Hirai (kN)	Cheng (kN)	Zhao (kN)	V_{Hirai}/W (-)	V_{Cheng}/W (-)	V_{Zhao}/W (-)
3	9	38.776	1937.64	2118.14	2039.16	3.20	3.50	3.37
3	15	38.776	4355.95	5065.34	4852.05	4.44	5.16	4.95
3	18	38.776	5882.66	7007.92	6703.00	5.03	6.00	5.74
5	15	38.776	7961.53	8831.47	8459.61	4.65	5.16	4.95
5	25	38.776	18570.30	21973.55	20970.62	6.71	7.94	7.58
5	30	38.776	25346.88	30745.77	29312.37	7.69	9.33	8.89

D(m)	L(m)	φ (°)	Hirai (kN)	Cheng (kN)	Zhao (kN)	V_{Hirai}/W(-)	V_{Cheng}/W (-)	V_{Zhao}/W (-)
8	24	38.776	30219.49	33861.38	32323.94	6.84	7.66	7.31
8	40	38.776	72289.70	86500.38	82356.57	10.11	12.10	11.52
8	48	38.776	99359.90	121904.95	115983.54	11.67	14.32	13.63

Table 12 – Results from analytical solutions $K_0 = 0.5$

Values of analytical solutions using γ' = 10 Ktan(δ) = 0.248								
D(m)	L(m)	φ (°)	Hirai (kN)	Cheng (kN)	Zhao (kN)	V_{Hirai}/W (-)	V_{Cheng}/W (-)	V_{Zhao}/W (-)
3	9	31.028	1939.60	1952.42	2041.73	3.20	3.22	3.37
3	15	31.028	4360.97	4617.86	4859.01	4.45	4.71	4.95
3	18	31.028	5889.76	6368.19	6712.95	5.04	5.45	5.74
5	15	31.028	7970.68	8051.29	8471.74	4.66	4.71	4.95
5	25	31.028	18593.67	19869.38	21003.36	6.72	7.18	7.59
5	30	31.028	25379.89	27738.46	29359.16	7.70	8.41	8.91
8	24	31.028	30257.17	30635.78	32374.12	6.85	6.93	7.32
8	40	31.028	72385.70	77806.55	82491.82	10.13	10.89	11.54
8	48	31.028	99495.42	109481.65	116176.80	11.69	12.86	13.65
Values of Vult using γ' = 10 Ktan(δ) = 0.281								
D(m)	L(m)	φ (°)	Hirai (kN)	Cheng (kN)	Zhao (kN)	V_{Hirai}/W (-)	V_{Cheng}/W (-)	V_{Zhao}/W (-)
3	9	34.262	2082.25	2239.63	2231.92	3.44	3.70	3.69
3	15	34.262	4728.99	5393.36	5372.55	4.82	5.50	5.48
3	18	34.262	6411.29	7476.88	7447.14	5.49	6.40	6.37
5	15	34.262	8637.03	9403.39	9367.11	5.05	5.50	5.48
5	25	34.262	20305.24	23516.02	23418.18	7.34	8.50	8.46
5	30	34.262	27802.41	32950.31	32810.47	8.43	10.00	9.95
8	24	34.262	33000.58	36225.93	36075.95	7.47	8.20	8.16
8	40	34.262	79414.87	92873.48	92469.22	11.11	12.99	12.94
8	48	34.262	109437.39	131011.97	130434.29	12.86	15.39	15.32

Values of Vult using γ' = 10 Ktan(δ) = 0.331								
D(m)	L(m)	φ (°)	Hirai (kN)	Cheng (kN)	Zhao (kN)	V_{Hirai}/W (-)	V_{Cheng}/W (-)	V_{Zhao}/W (-)
3	9	38.776	2295.49	2629.24	2523.57	3.79	4.34	4.17
3	15	38.776	5285.98	6445.39	6160.04	5.39	6.57	6.28
3	18	38.776	7203.38	8980.92	8572.97	6.16	7.68	7.34
5	15	38.776	9631.80	11237.61	10740.10	5.63	6.57	6.28
5	25	38.776	22893.10	28462.98	27121.18	8.27	10.28	9.80
5	30	38.776	31478.91	40020.62	38102.89	9.55	12.14	11.56
8	24	38.776	37093.06	43809.43	41752.51	8.39	9.91	9.45
8	40	38.776	90036.75	113313.00	107769.04	12.60	15.85	15.08
8	48	38.776	124518.92	160219.61	152297.41	14.63	18.82	17.89

The values of the analytical equations were plotted as a normalized uplift capacity (V_{ult}/W) and the soil stress level factor in order to englobe the caissons geometries difference, and compared with the numerical results in the charts below:

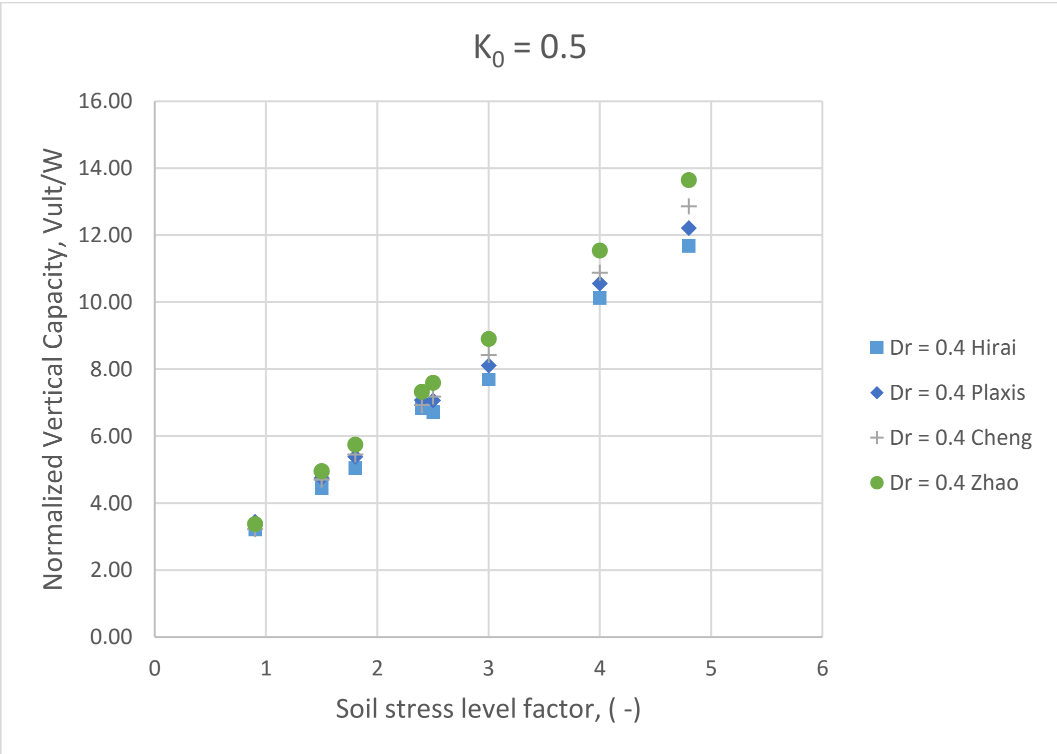

Figure B.1 – Comparsion between analytical equations and PLAXIS 2D results for Dr=0.4 in the axisymmetric model

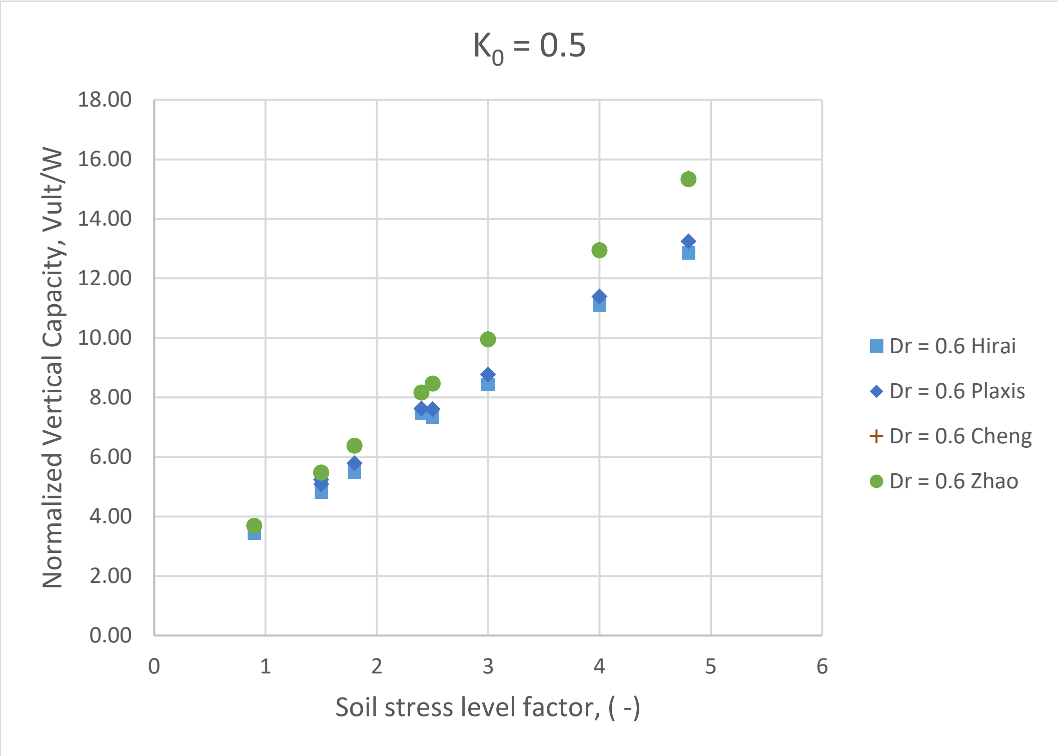

Figure B.2 – Comparsion between analytical equations and PLAXIS 2D results for Dr=0.6 in the axisymmetric model

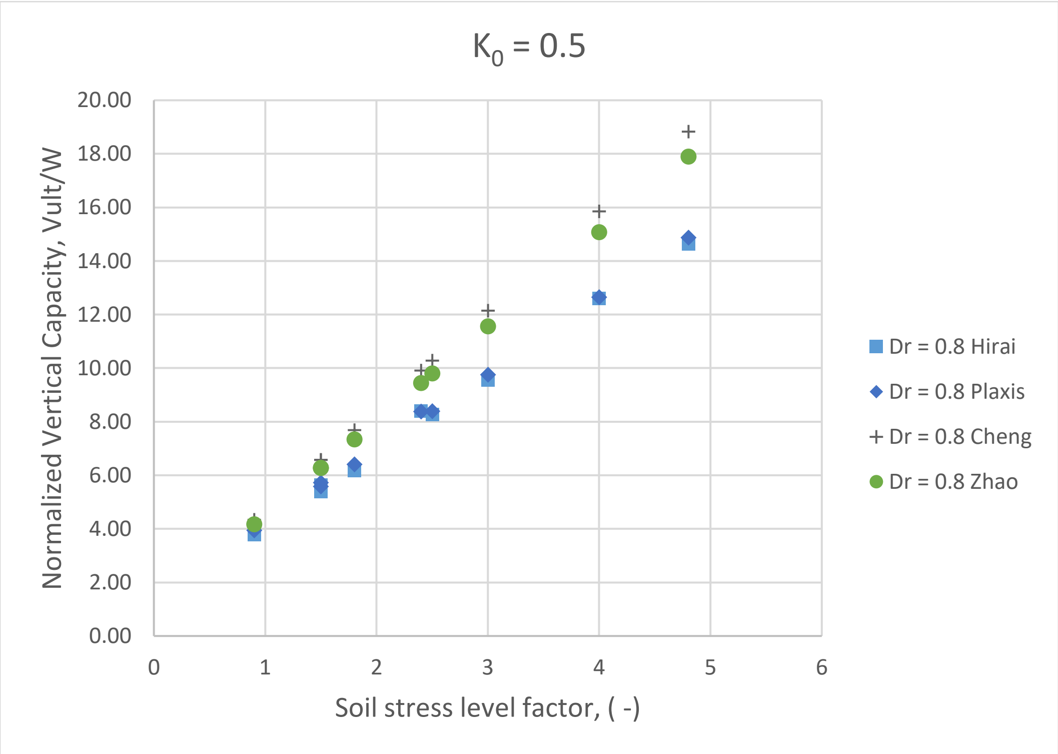

Figure B.3 – Comparsion between analytical equations and PLAXIS 2D results for Dr=0.8 in the axisymmetric model

Table 13 – Errors between PLAXIS 2D results and analytical equations for K_0=0.5 for the axisymmetric model

Values of error between PLAXIS 2D results and analytical solutions for Ktan(δ)=0.248					
D(m)	L(m)	φ (°)	Hirai error (-)	Cheng error (-)	Zhao error (-)
3	9	31.028	7.55	6.84	2.17
3	15	31.028	6.97	1.02	4.00
3	18	31.028	6.87	1.16	6.24
5	15	31.028	4.75	3.70	1.45
5	25	31.028	5.25	1.51	6.82
5	30	31.028	5.35	3.61	8.93
8	24	31.028	3.40	2.12	3.36
8	40	31.028	4.29	2.98	8.49
8	48	31.028	4.48	5.05	10.52
Values of error between PLAXIS 2D results and analytical solutions for Ktan(δ)=0.281					
D(m)	L(m)	φ (°)	Hirai error (-)	Cheng error (-)	Zhao error (-)
3	9	34.262	6.26	1.20	0.86
3	15	34.262	5.55	7.46	7.10
3	18	34.262	5.52	9.52	9.16
5	15	34.262	3.64	4.80	4.44
5	25	34.262	3.58	10.56	10.19
5	30	34.262	3.88	12.35	11.97
8	24	34.262	2.16	6.93	6.55
8	40	34.262	2.53	12.33	11.95
8	48	34.262	2.97	13.98	13.60
Values of error between PLAXIS 2D results and analytical solutions for Ktan(δ)=0.331					
D(m)	L(m)	φ (°)	Hirai error (-)	Cheng error (-)	Zhao error (-)
3	9	38.776	4.04	9.16	5.36
3	15	38.776	3.51	15.11	11.18
3	18	38.776	3.94	16.63	12.67
5	15	38.776	1.58	12.94	8.91
5	25	38.776	1.52	18.34	14.30

D(m)	L(m)	φ (°)	Hirai error (-)	Cheng error (-)	Zhao error (-)
5	30	38.776	2.14	19.66	15.62
8	24	38.776	0.09	15.41	11.24
8	40	38.776	0.45	20.19	16.08
8	48	38.776	1.65	21.00	16.89

Table 14 – K values of the installation phase

Calculations of the K value of the installation phase, $K_0 = 0.5$			
D(m)	L(m)	φ (°)	K_inst
3	9	31.028	0.54
3	15	31.028	0.554
3	18	31.028	0.545
5	15	31.028	0.572
5	25	31.028	0.524
5	30	31.028	0.529
8	24	31.028	0.536
8	40	31.028	0.53
8	48	31.028	0.522
3	9	34.262	0.594
3	15	34.262	0.548
3	18	34.262	0.537
5	15	34.262	0.564
5	25	34.262	0.522
5	30	34.262	0.527
8	24	34.262	0.533
8	40	34.262	0.529
8	48	34.262	0.521
3	9	38.776	0.578
3	15	38.776	0.543
3	18	38.776	0.533

D(m)	L(m)	φ (°)	K_inst
5	15	38.776	0.558
5	25	38.776	0.52
5	30	38.776	0.525
8	24	38.776	0.53
8	40	38.776	0.527
8	48	38.776	0.52

For the calculations in the plane strain model, with a force applied on the top cap of the caisson, the following tables of the calculations are presented:

Table 15 – Results of plane strain model of PLAXIS 2D using a K_0 = 0.5

Values of Vult using γ' = 10 Ktan(δ) = 0.248					
D(m)	L(m)	φ (°)	Fy (kN/m)	Fy/W (-)	k (-)
3	9	31.028	474.39	3.32	0.9
3	15	31.028	1039.22	4.61	1.5
3	18	31.028	1391.17	5.22	1.8
5	15	31.028	1133.33	4.74	1.5
5	25	31.028	2612.17	6.94	2.5
5	30	31.028	3552.24	7.98	3
8	24	31.028	2642.93	6.90	2.4
8	40	31.028	6337.54	10.51	4
8	48	31.028	8695.56	12.20	4.8
Values of Vult using γ' = 10 Ktan(δ) = 0.281					
D(m)	L(m)	φ (°)	Fy (kN/m)	Fy/W (-)	k (-)
3	9	34.262	496.9	3.48	0.9
3	15	34.262	1097.96	4.87	1.5
3	18	34.262	1465.81	5.50	1.8
5	15	34.262	1205.66	5.04	1.5
5	25	34.262	2783.64	7.40	2.5
5	30	34.262	3757.42	8.44	3
8	24	34.262	2836.04	7.40	2.4
8	40	34.262	6769.25	11.22	4
8	48	34.262	9131.71	12.81	4.8
Values of Vult using γ' = 10 Ktan(δ) = 0.331					
D(m)	L(m)	φ (°)	Fy (kN/m)	Fy/W (-)	k (-)
3	9	38.776	534.58	3.74	0.9
3	15	38.776	1184.52	5.26	1.5
3	18	38.776	1572.18	5.90	1.8
5	15	38.776	1315.36	5.50	1.5
5	25	38.776	3026.99	8.04	2.5

D(m)	L(m)	φ (°)	Fy (kN/m)	Fy/W (-)	k (-)
5	30	38.776	4048.13	9.09	3
8	24	38.776	3122.74	8.15	2.4
8	40	38.776	7359.77	12.20	4
8	48	38.776	9901.33	13.89	4.8

Table 16 – Results from analytical solutions adopted to plane strain using a K_0=0.5

Values of analytical solutions using γ' = 10 Ktan(δ) = 0.248								
D(m)	L(m)	φ (°)	Hirai (kN)	Cheng (kN)	Zhao (kN)	V_{Hirai}/W (-)	V_{Cheng}/W (-)	V_{Zhao}/W (-)
3	9	31.028	469.76	460.68	481.75	3.29	3.22	3.37
3	15	31.028	1056.27	1060.56	1115.94	4.69	4.71	4.95
3	18	31.028	1422.41	1452.18	1530.79	5.34	5.45	5.74
5	15	31.028	1151.05	1125.23	1183.99	4.82	4.71	4.95
5	25	31.028	2696.83	2702.24	2856.46	7.16	7.18	7.59
5	30	31.028	3673.30	3745.40	3964.23	8.25	8.41	8.91
8	24	31.028	2723.62	2656.82	2807.57	7.11	6.93	7.32
8	40	31.028	6560.47	6565.34	6960.69	10.88	10.89	11.54
8	48	31.028	9001.70	9171.51	9732.38	12.63	12.86	13.65
Values of Vult using γ' = 10 Ktan(δ) = 0.281								
D(m)	L(m)	φ (°)	Hirai (kN)	Cheng (kN)	Zhao (kN)	V_{Hirai}/W (-)	V_{Cheng}/W (-)	V_{Zhao}/W (-)
3	9	34.262	2082.25	2239.63	2231.92	3.54	3.70	3.69
3	15	34.262	4728.99	5393.36	5372.55	5.08	5.50	5.48
3	18	34.262	6411.29	7476.88	7447.14	5.80	6.40	6.37
5	15	34.262	8637.03	9403.39	9367.11	5.24	5.50	5.48
5	25	34.262	20305.24	23516.02	23418.18	7.82	8.50	8.46
5	30	34.262	27802.41	32950.31	32810.47	9.02	10.00	9.95
8	24	34.262	33000.58	36225.93	36075.95	7.78	8.20	8.16
8	40	34.262	79414.87	92873.48	92469.22	11.93	12.99	12.94
8	48	34.262	109437.39	131011.97	130434.29	13.85	15.39	15.32

Values of Vult using γ' = 10 Ktan(δ) = 0.331								
D(m)	L(m)	φ (°)	Hirai (kN)	Cheng (kN)	Zhao (kN)	V_{Hirai}/W (-)	V_{Cheng}/W (-)	V_{Zhao}/W (-)
3	9	38.776	2295.49	2629.24	2523.57	3.91	4.34	4.17
3	15	38.776	5285.98	6445.39	6160.04	5.66	6.57	6.28
3	18	38.776	7203.38	8980.92	8572.97	6.48	7.68	7.34
5	15	38.776	9631.80	11237.61	10740.10	5.86	6.57	6.28
5	25	38.776	22893.10	28462.98	27121.18	8.79	10.28	9.80
5	30	38.776	31478.91	40020.62	38102.89	10.16	12.14	11.56
8	24	38.776	37093.06	43809.43	41752.51	8.78	9.91	9.45
8	40	38.776	90036.75	113313.00	107769.04	13.49	15.85	15.08
8	48	38.776	124518.92	160219.61	152297.41	15.69	18.82	17.89

The results from plane strain model were plotted as the same way from the axisymmetric model, with the normalized vertical capacity as the V_{ult}/W, and the soil stress level factor:

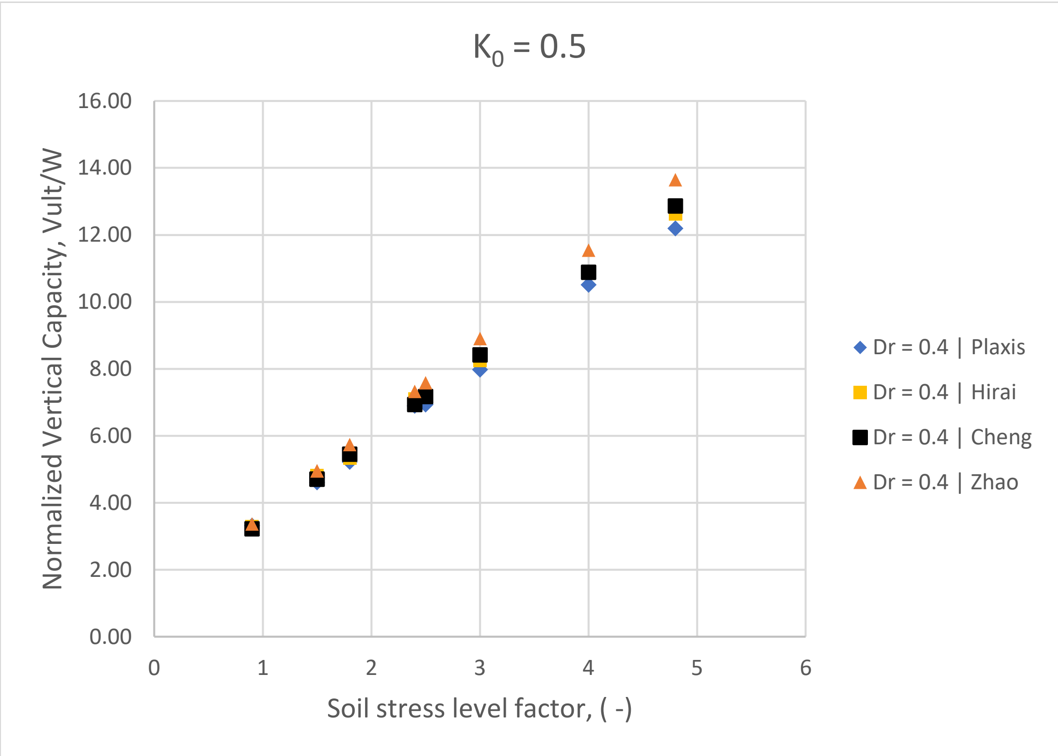

Figure B.4 – Comparsion between analytical equations and PLAXIS 2D results for Dr=0.4 in the plane strain model

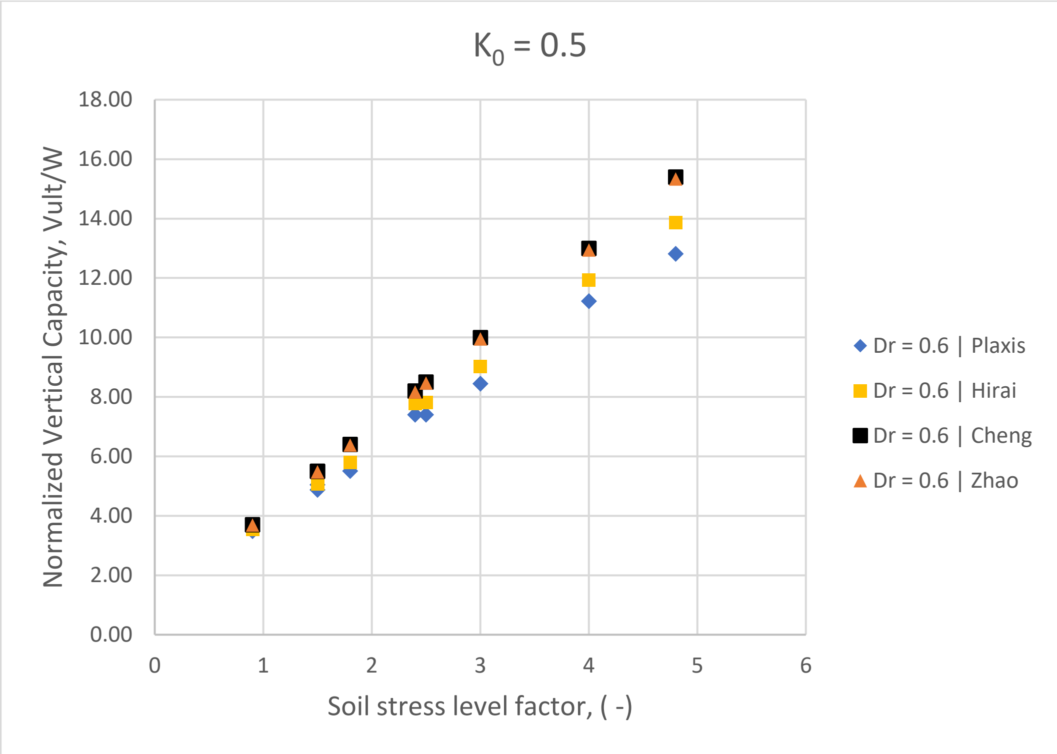

Figure B.5 – Comparsion between analytical equations and PLAXIS 2D results for Dr=0.6 in the plane strain model

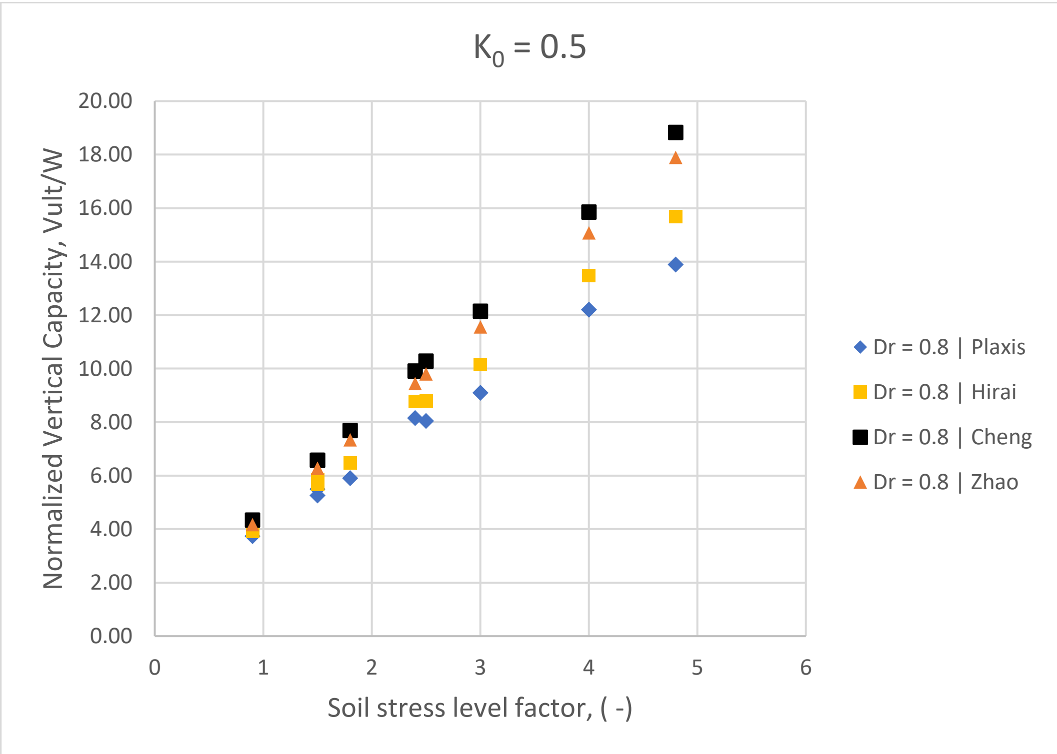

Figure B.6 – Comparsion between analytical equations and PLAXIS 2D results for Dr=0.8 in the plane strain model

Table 17 – Errors between PLAXIS 2D results and analytical equations for K_0=0.5 for the plane strain model

Values of error between PLAXIS 2D results and analytical solutions for Ktan(δ)=0.248					
D(m)	L(m)	φ (°)	Hirai error (-)	Cheng error (-)	Zhao error (-)
3	9	31.028	0.98	2.98	1.53
3	15	31.028	1.61	2.01	6.88
3	18	31.028	2.20	4.20	9.12
5	15	31.028	1.54	0.72	4.28
5	25	31.028	3.14	3.33	8.55
5	30	31.028	3.30	5.16	10.39
8	24	31.028	2.96	0.52	5.86
8	40	31.028	3.40	3.47	8.95
8	48	31.028	3.40	5.19	10.65
Values of error between PLAXIS 2D results and analytical solutions for Ktan(δ)=0.281					
D(m)	L(m)	φ (°)	Hirai error (-)	Cheng error (-)	Zhao error (-)
3	9	34.262	1.74	5.97	5.65
3	15	34.262	4.06	11.36	11.02
3	18	34.262	5.10	14.03	13.69
5	15	34.262	3.67	8.26	7.90
5	25	34.262	5.42	12.96	12.60
5	30	34.262	6.40	15.55	15.19
8	24	34.262	4.89	9.73	9.35
8	40	34.262	5.90	13.62	13.24
8	48	34.262	7.55	16.80	16.43
Values of error between PLAXIS 2D results and analytical solutions for Ktan(δ)=0.331					
D(m)	L(m)	φ (°)	Hirai error (-)	Cheng error (-)	Zhao error (-)
3	9	38.776	4.34	13.83	10.22
3	15	38.776	7.13	19.98	16.27
3	18	38.776	8.96	23.23	19.58
5	15	38.776	6.06	16.25	12.37
5	25	38.776	8.53	21.80	17.93

D(m)	L(m)	φ (°)	Hirai error (-)	Cheng error (-)	Zhao error (-)
5	30	38.776	10.51	25.09	21.32
8	24	38.776	7.17	17.81	13.76
8	40	38.776	9.52	23.03	19.07
8	48	38.776	11.47	26.23	22.39

Values of the uplift capacity for the load applied on different z_{pad}s of the anchor with different aspect ratios:

Table 18 – Values of the uplift capacity with the load applied on the padeye

Uplift capacity using a γ'= 10(γ$_{sub}$ = 19.81), K$_0$ = 0.5					
D(m)	L(m)	φ (°)	z_{pad} (-)	Fy (kN/m)	Rotation (°)
3	9	31.028	0.5	546.93	0.77886
3	9	31.028	0.6	548.59	0.81144
3	9	31.028	0.65	545.27	0.73109
3	9	31.028	0.7	545.46	0.7382
3	9	31.028	0.75	544.74	0.72245
3	9	34.262	0.5	570.7	0.81883
3	9	34.262	0.6	567.01	0.78125
3	9	34.262	0.65	567.58	0.76853
3	9	34.262	0.7	568.13	0.75628
3	9	34.262	0.75	568.07	0.74457
3	9	38.776	0.5	599.6	0.79313
3	9	38.776	0.6	599.57	0.83974
3	9	38.776	0.65	601.86	0.8569
3	9	38.776	0.7	601.13	0.80354
3	9	38.776	0.75	599.83	0.7851
3	18	31.028	0.5	1457	0.18008
3	18	31.028	0.6	1456.16	0.17982
3	18	31.028	0.65	1456.14	0.17982
3	18	31.028	0.7	1456.21	0.17985
3	18	31.028	0.75	1455.11	0.17965
3	18	34.262	0.5	1532.84	0.18524
3	18	34.262	0.6	1534.79	0.18564
3	18	34.262	0.65	1534.3	0.18585
3	18	34.262	0.7	1534.89	0.18592
3	18	34.262	0.75	1533.71	0.18759
3	18	38.776	0.5	1651.75	0.2087
3	18	38.776	0.6	1658.41	0.22293

D(m)	L(m)	φ (°)	z_{pad} (-)	Fy	Rotation (°)
3	18	38.776	0.65	1651.9	0.21544
3	18	38.776	0.7	1651.8	0.21347
3	18	38.776	0.75	1649.62	0.21236
Uplift capacity using a γ'= 10($γ_{sub}$ = 19.81), K_0 = 1 – sin(φ)					
D(m)	L(m)	φ (°)	z_{pad} (-)	Fy (kN/m)	Rotation (°)
3	9	31.028	0.5	545.25	0.77055
3	9	31.028	0.6	547.37	0.81723
3	9	31.028	0.65	549.83	0.91911
3	9	31.028	0.7	548.43	0.84936
3	9	31.028	0.75	538.68	0.59834
3	9	34.262	0.5	567.34	0.7944
3	9	34.262	0.6	566.9	0.79872
3	9	34.262	0.65	566.51	0.77487
3	9	34.262	0.7	566.33	0.77747
3	9	34.262	0.75	567.34	0.7944
3	9	38.776	0.5	580.48	0.84488
3	9	38.776	0.6	576.18	0.80075
3	9	38.776	0.65	591.01	0.97105
3	9	38.776	0.7	588.06	0.90394
3	9	38.776	0.75	585.82	0.86321
3	18	31.028	0.5	1442.53	0.18432
3	18	31.028	0.6	1441.84	0.18409
3	18	31.028	0.65	1441.88	0.18416
3	18	31.028	0.7	1441.67	0.18413
3	18	31.028	0.75	1440.99	0.18418
3	18	34.262	0.5	1457.52	0.20769
3	18	34.262	0.6	1458.48	0.20786
3	18	34.262	0.65	1458.29	0.20795
3	18	34.262	0.7	1458.49	0.2078
3	18	34.262	0.75	1458.74	0.20973
3	18	38.776	0.5	1465.86	0.24402

D(m)	L(m)	φ (°)	z_{pad} (-)	Fy(kN/m)	Rotation (°)
3	18	38.776	0.6	1471.34	0.24694
3	18	38.776	0.65	1467.28	0.24476
3	18	38.776	0.7	1468.72	0.24578
3	18	38.776	0.75	1480.47	0.25419

Table 19 – Values of the lateral capacity

Lateral capacity using a γ'= 10(γ_{sub} = 19.81), K_0 = 0.5							
D(m)	L(m)	φ (°)	z_{pad} (-)	Fx(kN/m)	Rotation (°)	Ux top cap(m)	Uy top cap(m)
3	9	31.028	0.5	1074.54	-1.676	0.344	0.014
3	9	31.028	0.6	1479.86	-0.924	0.406	-0.009
3	9	31.028	0.65	1536.37	0.100	0.328	-0.031
3	9	31.028	0.7	1433.14	0.656	0.195	-0.048
3	9	31.028	0.75	1335.78	0.888	0.123	-0.056
3	9	34.262	0.5	1160.27	-1.560	0.332	0.018
3	9	34.262	0.6	1602.22	-0.847	0.399	-0.004
3	9	34.262	0.65	1694.68	0.238	0.330	-0.036
3	9	34.262	0.7	1646.79	0.868	0.235	-0.052
3	9	34.262	0.75	1536.77	1.163	0.150	-0.065
3	9	38.776	0.5	1283.67	-1.418	0.320	0.022
3	9	38.776	0.6	1776	-0.712	0.379	-0.003
3	9	38.776	0.65	1865.5	0.193	0.318	-0.033
3	9	38.776	0.7	1751.6	0.680	0.201	-0.051
3	9	38.776	0.75	1704.23	1.182	0.151	-0.067
3	18	31.028	0.5	3171.38	-1.763	0.661	0.044
3	18	31.028	0.6	4988.41	-1.703	1.035	0.062
3	18	31.028	0.65	5292.84	0.006	0.741	-0.026
3	18	31.028	0.7	5021.3	0.871	0.430	-0.082
3	18	31.028	0.75	4389.84	0.935	0.218	-0.104
3	18	34.262	0.5	4125.44	-2.882	1.065	0.124
3	18	34.262	0.6	5661.83	-1.442	1.084	0.072
3	18	34.262	0.65	5947.78	0.226	0.780	-0.030

D(m)	L(m)	φ (°)	z_{pad} (-)	Fx(kN/m)	Rotation (°)	Ux top cap(m)	Uy top cap(m)
3	18	34.262	0.7	5602.02	1.022	0.465	-0.094
3	18	34.262	0.75	4954.92	1.053	0.244	-0.115
3	18	38.776	0.5	4685.48	-2.695	1.050	0.143
3	18	38.776	0.6	6242.89	-1.089	0.974	0.051
3	18	38.776	0.65	6570.09	0.226	0.746	-0.033
3	18	38.776	0.7	6261.46	1.036	0.470	-0.099
3	18	38.776	0.75	5935.12	1.420	0.296	-0.135
Lateral capacity using a γ'= 10(γ_{sub} = 19.81), K_0 = 1 – sin(φ)							
D(m)	L(m)	φ (°)	z_{pad} (-)	Fx(kN/m)	Rotation (°)	Ux top cap(m)	Uy top cap(m)
3	9	31.028	0.6	1463.42	-1.032	0.409	-0.003
3	9	31.028	0.65	1524.18	0.072	0.321	-0.031
3	9	31.028	0.7	1445.31	0.699	0.201	-0.051
3	9	31.028	0.75	1352.29	0.949	0.129	-0.058
3	9	34.262	0.6	1599.7	-0.849	0.399	-0.010
3	9	34.262	0.65	1634.03	0.132	0.304	-0.040
3	9	34.262	0.7	1607.68	0.791	0.221	-0.057
3	9	34.262	0.75	1470.22	0.921	0.136	-0.065
3	9	38.776	0.5	1263.08	-1.409	0.336	0.012
3	9	38.776	0.6	1698.72	-0.685	0.366	-0.018
3	9	38.776	0.65	1813.14	0.157	0.314	-0.051
3	9	38.776	0.7	1724.97	0.650	0.214	-0.067
3	9	38.776	0.75	1596.97	0.901	0.137	-0.079
3	18	31.028	0.5	3262.04	-1.927	0.718	0.051
3	18	31.028	0.6	4959.31	-1.672	1.019	0.056
3	18	31.028	0.65	5084.46	-0.072	0.669	-0.028
3	18	31.028	0.7	5022.47	0.892	0.438	-0.088
3	18	31.028	0.75	4722.27	1.267	0.260	-0.118
3	18	34.262	0.5	4024.18	-2.678	1.010	0.107
3	18	34.262	0.6	5507.09	-1.306	1.010	0.047
3	18	34.262	0.65	5853.38	0.159	0.759	-0.042

D(m)	L(m)	φ (°)	z_{pad} (-)	Fx(kN/m)	Rotation (°)	Ux top cap(m)	Uy top cap(m)
3	18	34.262	0.7	5615.32	1.053	0.482	-0.106
3	18	34.262	0.75	5157.99	1.282	0.280	-0.137
3	18	38.776	0.5	4764.17	-2.931	1.172	0.145
3	18	38.776	0.6	5988.06	-1.122	0.948	0.021
3	18	38.776	0.65	6568.39	0.231	0.788	-0.061
3	18	38.776	0.7	6435.52	1.261	0.545	-0.139
3	18	38.776	0.75	5511.35	1.137	0.284	-0.159

Table 20 – Values of the inclined capacity

Lateral capacity using a γ'= 10(γ_{sub} = 19.81), K_0 = 0.5								
D(m)	L(m)	φ (°)	z_{pad} (-)	Fx(kN/m)	Fy(kN/m)	Rotation (°)	Ux top cap(m)	Uy top cap(m)
3	9	31.028	0.5	798.9	461.25	-1.139	0.274	0.129
3	9	31.028	0.6	864.49	499.12	-0.113	0.183	0.091
3	9	31.028	0.65	877.07	506.38	0.362	0.144	0.071
3	9	31.028	0.7	879.45	507.75	0.797	0.103	0.051
3	9	31.028	0.75	858.16	495.46	1.126	0.055	0.033
3	9	31.028	0.8	811.69	468.63	1.433	-0.006	0.019
3	9	31.028	0.9	706.34	407.8	1.853	-0.098	0.004
3	9	34.262	0.5	868.52	501.44	-1.129	0.303	0.152
3	9	34.262	0.6	895.02	516.74	-0.107	0.162	0.075
3	9	34.262	0.65	912.97	527.11	0.279	0.139	0.064
3	9	34.262	0.7	916.52	529.16	0.698	0.104	0.051
3	9	34.262	0.75	901.06	520.23	1.019	0.056	0.031
3	9	34.262	0.8	857.34	494.99	1.292	0.002	0.019
3	9	34.262	0.9	768.69	443.81	2.040	-0.111	0.004
3	9	38.776	0.5	934.12	539.31	-1.040	0.295	0.154
3	9	38.776	0.6	982.81	567.43	-0.038	0.189	0.094
3	9	38.776	0.7	997.14	575.7	0.654	0.109	0.054
3	9	38.776	0.75	950.83	548.96	0.801	0.062	0.033
3	9	38.776	0.8	919.58	530.92	1.134	0.013	0.023

D(m)	L(m)	φ (°)	z_{pad} (-)	Fx(kN/m)	Fy(kN/m)	Rotation (°)	Ux top cap(m)	Uy top cap(m)
3	9	38.776	0.9	832.98	480.92	1.870	-0.097	0.006
3	18	31.028	0.5	2348.93	1356.16	-1.502	0.598	0.279
3	18	31.028	0.65	2664.53	1538.37	-0.084	0.330	0.194
3	18	31.028	0.7	2710.69	1565.02	0.324	0.261	0.176
3	18	31.028	0.75	2768.06	1598.14	0.799	0.188	0.162
3	18	31.028	0.8	2630.37	1518.65	1.069	0.059	0.094
3	18	31.028	0.9	2422.02	1398.35	2.045	-0.210	0.047
3	18	34.262	0.5	2490.26	1437.75	-1.417	0.584	0.282
3	18	34.262	0.6	2716.85	1568.57	-0.511	0.401	0.216
3	18	34.262	0.65	2845.5	1642.85	-0.083	0.355	0.215
3	18	34.262	0.7	2875.19	1659.99	0.289	0.272	0.182
3	18	34.262	0.75	2905.03	1677.22	0.775	0.186	0.159
3	18	34.262	0.8	2821.9	1629.23	1.095	0.070	0.105
3	18	34.262	0.9	2649.62	1529.76	2.294	-0.238	0.050
3	18	38.776	0.5	2687.46	1551.61	-1.349	0.584	0.303
3	18	38.776	0.6	2920.09	1685.92	-0.493	0.412	0.230
3	18	38.776	0.65	3016.77	1741.73	-0.092	0.344	0.204
3	18	38.776	0.7	3147.65	1817.3	0.350	0.301	0.203
3	18	38.776	0.75	3152.43	1820.06	0.758	0.201	0.164
3	18	38.776	0.8	3040.06	1755.18	1.069	0.081	0.110
3	18	38.776	0.9	2815.88	1625.75	1.965	-0.186	0.048
Lateral capacity using a γ'= 10(γ_{sub} = 19.81), K_0 = 1 – sin(φ)								
D(m)	L(m)	φ (°)	z_{pad} (-)	Fx(kN/m)	Fy(kN/m)	Rotation (°)	Ux top cap(m)	Uy top cap(m)
3	9	31.028	0.5	795.42	459.24	-1.116	0.268	0.124
3	9	31.028	0.6	859.31	496.12	-0.092	0.177	0.084
3	9	31.028	0.65	877.68	506.73	0.386	0.151	0.073
3	9	31.028	0.7	887.68	512.5	0.870	0.112	0.057
3	9	31.028	0.75	855.52	493.94	1.203	0.052	0.031
3	9	31.028	0.8	799.57	461.63	1.314	-0.002	0.016

D(m)	L(m)	φ (°)	z_{pad} (-)	Fx(kN/m)	Fy(kN/m)	Rotation (°)	Ux top cap(m)	Uy top cap(m)
3	9	31.028	0.9	702.03	405.32	1.783	-0.094	0.003
3	9	34.262	0.5	853.67	492.87	-1.152	0.299	0.144
3	9	34.262	0.6	897.44	518.14	-0.068	0.174	0.077
3	9	34.262	0.65	911.43	526.22	0.296	0.138	0.059
3	9	34.262	0.7	932.69	538.49	0.726	0.121	0.056
3	9	34.262	0.75	924.2	533.59	1.322	0.065	0.040
3	9	34.262	0.8	852.68	492.3	1.240	0.009	0.018
3	9	34.262	0.9	766.6	442.6	2.005	-0.103	0.002
3	9	38.776	0.5	927.79	535.66	-1.090	0.311	0.151
3	9	38.776	0.6	978.89	565.16	-0.088	0.200	0.089
3	9	38.776	0.65	993.53	573.61	0.283	0.166	0.070
3	9	38.776	0.7	1001.9	578.45	0.692	0.132	0.056
3	9	38.776	0.75	992.8	573.19	1.119	0.084	0.038
3	9	38.776	0.8	941.28	543.45	1.286	0.025	0.018
3	9	38.776	0.9	855.67	494.02	2.344	-0.122	-0.003
3	18	31.028	0.5	2306.53	1331.67	-1.375	0.547	0.246
3	18	31.028	0.6	2610.85	1507.37	-0.540	0.431	0.236
3	18	31.028	0.65	2656.84	1533.93	-0.090	0.330	0.192
3	18	31.028	0.75	2715.41	1567.74	0.726	0.175	0.142
3	18	31.028	0.8	2629.21	1517.98	1.042	0.066	0.094
3	18	31.028	0.9	2477.36	1430.31	2.333	-0.246	0.049
3	18	34.262	0.5	2517.23	1453.32	-1.564	0.656	0.323
3	18	34.262	0.6	2766.31	1597.13	-0.542	0.454	0.249
3	18	34.262	0.65	2807.58	1620.96	-0.124	0.358	0.206
3	18	34.262	0.7	2904.66	1677	0.345	0.304	0.201
3	18	34.262	0.75	2923.12	1687.66	0.764	0.204	0.159
3	18	34.262	0.8	2835.64	1637.16	1.098	0.087	0.107
3	18	34.262	0.9	2624.28	1515.13	2.211	-0.219	0.047
3	18	38.776	0.5	2670.91	1542.05	-1.469	0.652	0.329
3	18	38.776	0.6	2968.48	1713.85	-0.540	0.491	0.267
3	18	38.776	0.65	3050.86	1761.42	-0.115	0.413	0.234

D(m)	L(m)	φ (°)	z_{pad} (-)	Fx(kN/m)	Fy(kN/m)	Rotation (°)	Ux top cap(m)	Uy top cap(m)
3	18	38.776	0.7	3193.62	1843.84	0.422	0.359	0.232
3	18	38.776	0.75	3193.62	1843.84	0.844	0.249	0.185
3	18	38.776	0.8	2984.49	1723.09	0.962	0.121	0.100
3	18	38.776	0.9	2800.81	1617.05	2.126	-0.188	0.046